

THE MECHANICS OF CENTRAL PEAK FORMATION  
IN SHOCK WAVE CRATERING EVENTS

by

Gilbert W. Ullrich

B. S. The Citadel (1967)

M. S. The Air Force Institute of Technology (1969)

SUBMITTED IN PARTIAL FULFILLMENT  
OF THE REQUIREMENTS FOR THE  
DEGREE OF DOCTOR OF  
PHILOSOPHY

at the

Massachusetts Institute of Technology

August, 1974

Signature of Author. \_\_\_\_\_

Dept. of Earth and Planetary Sciences  
/ / /

Certified by \_\_\_\_\_

Thesis Supervisor

Accepted by \_\_\_\_\_

Chairman, Departmental Committee on  
Graduate Students Lindgren

**WITHDRAWN**  
**(NOT FROM 1974)**

THE MECHANICS OF  
CENTRAL PEAK FORMATION  
IN SHOCK WAVE CRATERING EVENTS

by

Gilbert W. Ullrich

Abstract

Central peaks are common features observed in craters on the Earth, the Moon, Mars, and Mercury. Since these peaks do not occur in all craters, they should be useful in providing strong constraints on both planetary evolution and numerical cratering simulations. Unfortunately, because the mechanics of central peak formation has been poorly understood, little use of those constraints has yet been made.

Therefore, a program of numerical simulations of the ground response to a high-explosive detonation was accomplished to examine the influence of model conditions on calculated central-peak formation. During this program, data from a numerical simulation of a high-explosive detonation were used as a surface-boundary condition, and the ground response was simulated by a computer code that modeled two-dimensional, axisymmetric problems of continuum-mechanics with elastic-plastic material models. First, a calculation that modeled the 20 ton high-explosive detonation designated Mixed Company II showed that, when ballistically extrapolated, the computed motions at a simulated time of 16.4 msec were consistent with the observed crater and formation of a central mound. The results of a series of calculations in which compaction, layering, and material-yield models were varied indicated 1) the calculated upward motions below the crater were eliminated by increased material-compactibility, 2) the model of test-site layering in the Mixed Company II numerical simulation only slightly influenced the upward velocities below the crater, 3) plastic volumetric-increases of material during Mohr-Coulomb yield contributed significantly to the calculation of upward motions, 4) upward velocities for points on the axis of symmetry were first calculated where strength effects were important, and 5) the inclusion of a lower, "fluid" layer modified the calculated response in an overlying, solid layer in a manner that may have eventually resulted in upward motions.

A mechanical model of central mound formation is developed with the results of the numerical calculations as a guide. Material rebound in the region where strength effects are important is emphasized in the model. Central mounds would be inhibited by material compaction unless a lower layer responded as a fluid. The mechanical model includes enhancement of the central mound primarily by material bulking but also by

reflections of stress waves and the effect of the main shear-wave. Gravitational adjustments that contribute to inward displacements are considered possible. This model is found to be consistent with both the observed occurrence and structural relations of central peaks at sites of nuclear and high-explosive detonations and hypervelocity impact events. The conclusions are that the mechanical model is generally applicable to central peak formation, the occurrence of a central peak in a crater is primarily dependent on material properties of the medium, and the calculational code used for the numerical simulations can serve as a tool to investigate whose material properties.

Advisor: M. Gene Simmons

Title: Professor of Geophysics

Acknowledgments

I wish to thank M. G. Simmons for the help he contributed to this work. His time, encouragement, and suggestions were extremely valuable and appreciated.

The aid of R. J. Port, of the Air Force Weapons Laboratory, was invaluable. He first suggested the Mixed Company II numerical simulation, and then provided the physical insight required to develop the successful model. Without his contributions, the knowledge gained during this study would have been more difficult to obtain.

I also appreciate the guidance and support provided by D. R. Roddy, T. R. McGetchin, C. Goetze, and J. B. Southard. Their time and ideas were especially important.

I thank J. G. Trulio for his permission to use the AFTON-2A code.

I am also grateful to R. Waters, of the Defense Nuclear Agency, and B. L. Carnes, of the U. S. Army Waterways Experiment Station, for providing the Mixed Company II crater profiles.

Significant support was obtained from many other personnel of the Air Force Weapons Laboratory Civil Engineering Branch and the Air Force Cambridge Research Laboratory Computation Support Division. This support included both provision of, and training in, the computer codes used during this study, and aid in the solution of the many programming problems encountered. Also many administrative problems were quickly alleviated.

I would like to thank Ms. Ingham for typing the manuscript.

Finally, special thanks must be expressed to my wife, Suki. Her encouragement and adaptation to a strange world meant more than I can say. This thesis must be dedicated to her.

Financial support during this study was obtained from the U. S. Air Force through the Air Force Institute of Technology Civilian Institutes Program, and from the National Aeronautics and Space Administration under contract NGL-22-009-187. The computations were accomplished at the Air Force Cambridge Research Laboratory computer facility with the sponsorship of the Air Force Weapons Laboratory.

Gilbert Wayne Ullrich

Table of Contents

	<u>Page</u>
Abstract	2
Acknowledgments	4
Table of Contents	6
List of Figures	8
Chapter I. Introduction	11
Chapter II. Previous Work of Others	18
Occurrence and Structure of Central Peaks	18
Previous Computational Programs	30
Postulated Mechanisms	37
Chapter III. Numerical Simulation of Shock-Wave-Cratering	44
Mixed Company II Experiment	44
Computational Model of Mixed Company II	48
Mixed Company II Numerical Simulation (MC 2.12)	61
Numerical Parametric Study	79
Chapter IV. Discussion and Conclusions	114
Discussion	114
Conclusions	122
Future Work	124
Appendix I. Computation Parameters	127

	<u>Page</u>
Appendix II. The AFTON-2A Code	132
Appendix III. Auxiliary Computation Routines	158
Bibliography	164
Biographical Note	170

List of Figures

<u>Figure</u>		<u>Page</u>
1	The lunar craters Alphonsus, Alpetragius, and Arzachel with peaks in the center of the craters.	12
2	Generalized stratigraphic sections from the western side of the Flynn Creek structure.	20
3	The size distribution of craters with central peaks on the Earth, Mars, and the Moon.	25
4	Cross section of the crater produced by the 500 ton TNT event Snowball.	25
5	Velocity vectors at a simulated time of 220 msec for the Distant Plain 6 calculation.	32
6	Vertical velocity comparison between Middle Gust III experimental measurement and three material models.	36
7	Composite crater profile constructed from the detonation of two 40-grain dynamite charges.	39
8	Theoretical lines of slip under a valley with sides dipping at $30^{\circ}$ to the horizontal.	39
9	Apparent and true crater profiles of the 20 ton TNT event Mixed Company II.	47
10	The model pressure - specific volume relation in the low pressure regime for Layer 2.	54
11	The model pressure - specific volume relation in the high pressure regime for Layer 2.	55
12	Schematic yield surface for materials.	58
13	Velocity vector plot for MC 2.12 at 8.4 msec after detonation.	62
14	Principal stress axes plot for MC 2.12 at 8.4 msec after detonation.	63
15	Calculation grid plot for MC 2.12 at 616.4 msec after detonation compared to observed apparent and true crater profiles along the southern radial of the Mixed Company II crater.	64

<u>Figure</u>	<u>Page</u>
16 Velocity vector plot for MC 2.12 at 3.0 msec after detonation.	67
17 Acceleration vector plot for MC 2.12 at 3.0 msec after detonation.	68
18 Motion time history for the target point originally located on the vertical axis at 10 ft depth in the MC 2.12 calculation.	70
19 Stress time history for the target point of Figure 18.	71
20 Motion time history of the target point originally located at 4 ft range and 8 ft depth in the MC 2.12 calculation.	72
21 Stress time history for the target point of Figure 20.	73
22 Motion time history of the target point originally located at 18 ft range and 4 ft depth in the MC 2.12 calculation.	75
23 Stress time history for the target point of Figure 22.	76
24 Maximum pressure contours as a function of original position for the MC 2.12 calculation.	77
25 Motion time history of the target point originally located at 6 ft range and 1 ft depth in the MC 2.12 calculation.	78
26 Velocity vector plot for MC 2.13 at 9.5 msec after detonation.	81
27 Velocity vector plot for MCP-03 at 8.2 msec after detonation.	82
28 Velocity vector plot for MCP-09 at 9.5 msec after detonation.	85
29 Velocity vector plot for MCP-09 at 2.8 msec after detonation.	86
30 Velocity vector plot for MCP-01 at 8.4 msec after detonation.	88
31 Velocity vector plot for MCP-02 at 9.5 msec after detonation.	89

<u>Figure</u>	<u>Page</u>
32 Velocity vector plot for MC 2.15 at 8.4 msec after detonation.	92
33 Velocity vector plot for MCP-06 at 3.2 msec after detonation.	94
34 Velocity vector plot for MCP-02 at 3.2 msec after detonation.	95
35 Velocity vector plot for MCP-05 at 19.9 msec after detonation.	98
36 Velocity vector plot for MCP-21 at 5.6 msec after detonation.	101
37 Velocity vector plot for MCP-21 at 6.9 msec after detonation.	102
38 Velocity vector plot for MCP-21 at 10.5 msec after detonation.	103
39 Motion time history for the target point originally located on the vertical axis at 12 ft depth in the MCP-21 calculation.	104
40 Stress time history for the target point of Figure 39.	105
41 Stress time history for the target point originally located on the vertical axis at 20 ft depth in the MCP-21 calculation.	106
42 The lunar crater Lansberg, located near 0°N, 26.5°W, with a pronounced central peak.	109
43 The lunar crater Reinhold, located near 3°N, 23°W, with no pronounced central peak.	110
44 Velocity vector plot for MCP-12 at 16.6 msec after detonation.	111

THE MECHANICS OF CENTRAL PEAK FORMATION  
IN SHOCK WAVE CRATERING EVENTS

Chapter I. Introduction

Central peaks, or mounds (Figure 1), are a common feature of craters. Such peaks have been observed in craters measured in feet (Roddy, 1968; 1973) and in craters measured in tens of miles (Baldwin, 1963). They occur in craters produced by chemical explosives (Roddy, 1973) and in ancient impact structures on the earth (Howard et al., 1972; Roddy, 1968; Dence, 1968; Beals, 1965). They have been seen in craters on the Moon (Baldwin, 1963), on Mars (Hartmann, 1973), and on Mercury (Murray et al., 1974). However, while several authors have advanced hypotheses as to the cause of central peaks (Baldwin, 1963; Short, 1965; Dence, 1968; Milton and Roddy, 1972), a satisfactory explanation of the mechanics of central mound formation has not been demonstrated.

Central mounds serve as a very useful constraint on cratering calculations because they are directly observable. The Defense Nuclear Agency, a branch of the U. S. Department of Defense, has sponsored many attempts to simulate numerically the cratering and ground-shock effects of experiments where high-explosive charges were detonated at the surface of the earth

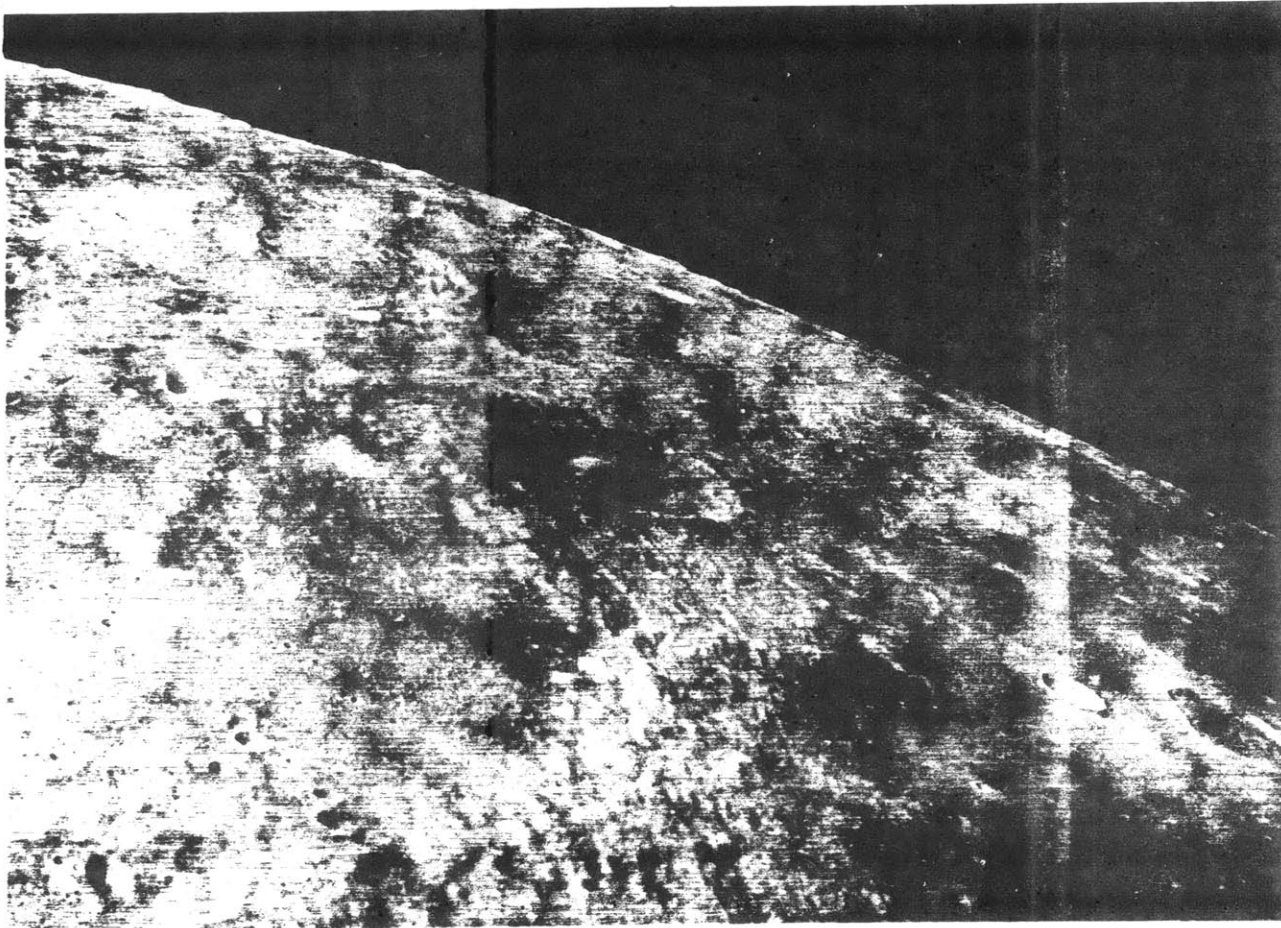


Figure 1. The lunar craters Alphonsus (bottom), Alpetragius (center), and Arzachel (top) with peaks in the center of the craters (NASA photograph AS-12-51-7580, Apollo 12).

(Christensen, 1969; Maxwell and Moises, 1971b; Port and Gajewski, 1973; Wright et al., 1973; Ialongo, 1973). Primary constraints on these calculations have been comparisons with crater radii and depths, and comparisons with ground-motion data obtained from active instrumentation usually emplaced more than one crater radius from ground zero. Although central mounds occurred in many of the craters (Roddy, 1968; 1973), little attention has been given to whether the motions predicted by such calculations are consistent with central peak formation. Christensen (1970) considered such a constraint, and he found the requirement for upward motions below the detonation point to be a very useful guide to the physics required in the calculation because, while all computations predicted a crater, a central mound was predicted only under limited conditions. Therefore, the presence or absence of a central mound in an experimentally produced crater provides an immediate direct test of the adequacy of numerical simulations, and an understanding of the causes of the central mound will be important to the understanding of cratering and ground-shock mechanics.

Also, the central peaks observed in hypervelocity impact craters on planetary surfaces provide information on the conditions of the impact event. The high velocity impact of a body on a planetary surface is a dynamic test of the two bodies over a very short time period. This information is recorded in the occurrence of a central mound; because, while the size of the crater is primarily controlled by the mass and velocity of the impacting particle (Baldwin, 1963), the formation of a central

mound is primarily controlled either by properties of the planet (Baldwin, 1963; Short, 1965; Dence, 1968), by properties of the impacting body (Milton and Roddy, 1972), or by properties of both (Roddy, 1968b). An understanding of the causes of central mound formation may allow us to obtain information concerning the conditions at the time a crater was formed. The evolution of those conditions may then be studied by observations of craters of different ages, and variations of those conditions with location may be tested with central-peak data in different locations.

The central peaks of craters represent important sampling sites for any extraterrestrial landing or remote sensing mission. Roddy (1968) showed that the material in the central mound is the deepest material exposed during the cratering event. A traverse across the mound will sample the deepest stratigraphic section obtainable at the surface of a crater. An understanding of central peak formation will aid the determination of the pre-impact location of the material.

Therefore, a program of numerical simulations was accomplished to examine the causes of central peak formation in a shock-wave-cratering event. During this program, the models were limited to the simplest possible expressions to demonstrate which factors were most important in the formation of a central mound. These models were an idealization of much more complex material behavior. I used a computer code, AFTON-2A (see Appendix II), that was already actively used for ground-shock calculations (see for example Port and Gajewski, 1973) and did no code

development other than modifications of material behavior models. One model of a high-explosive detonation was used for all of the numerical simulations, and only models of material properties were varied. The results of the calculations were generalized to different types of cratering events by developing a general model for the causes of central mound formation that was compared to reported observations of central mounds.

To clarify the discussion contained in this paper, the terms "shock-wave-cratering event" and "central mound" should be defined. A "shock-wave-cratering event" is an event that transfers a large amount of energy to a small volume of a half-space by sending a shock wave into the halfspace and forms a crater at the surface. This term applies to both a hypervelocity impact and a surface chemical or nuclear explosive detonation. Further, as Shoemaker (1961) suggests, this term is more basic than explosion cratering event because, even if the characteristics of craters are controlled by the expansion of gases near the source of the event (Baldwin, 1963), the passage of the shock wave through the material is the mechanism which establishes the conditions for such expansion. A "central mound" is a local topographical high at the center of a crater that is composed of material that was displaced upward during the cratering event. This term is applicable to a definite structural feature, and is not meant to include the possibility that material ejected from the crater may subsequently fall into the crater and form a hill at the center. Also, in this paper, the terms "central peak" and "central mound" will be synonymous.

Three assumptions were basic to the physical models used. First, all calculations were performed assuming axial symmetry, i.e., all properties can be described in terms of the radial and axial position coordinates of a cylindrical co-ordinate system. Second, all material models were assumed to be isotropic. Finally, no energy transfer by radiation or conduction was considered.

In addition to the basic assumptions, several additional assumptions were involved in this study. Some of these assumptions were inherent in the AFTON-2A code, and will be described in an appendix. Other assumptions were involved in the description of the numerical experiments accomplished during this study and will be described during the presentation of those problems.

The generalization of the results of numerical simulations should be done cautiously because those results strictly apply only to definite models with specific input parameters. The following procedure will be used to generalize specific numerical results concerning the mechanics of central peak formation. First the available information pertinent to central peaks will be reviewed to provide the broadest possible base of data. Then, a numerical model of the high-explosive experiment Mixed Company II will be described to demonstrate the applicability of the numerical results to that one experiment. The results from additional numerical simulations in which material models were varied will be described to determine what properties are important to central peak formation. These properties will be included in a general model of central peak mechanics which

will be tested by comparisons with the available information described initially. Through this comparison the relevance of the general model will be determined.

## Chapter II. Previous Work of Others

Three types of information concerning central mounds in shock-produced craters are available. First, observations, presented by others, of the occurrence of central peaks and of the structure of central uplifts in both ancient impact features on earth and experimental high-explosive detonations provide constraints on any explanation of central peak formation. Second, numerical simulations of shock-wave-cratering events provide guides to the physical processes involved in central mound formation. Finally, several others have previously proposed hypotheses concerning the causes of central peak formation. In this chapter, information of each type is reviewed to provide a basis for later conclusions concerning the mechanics of central mound formation.

### Occurrence and Structure of Central Peaks

Observations of the structure of central uplifts and their occurrence in craters indicate that similar relations apply to both hypervelocity impact events and explosive detonations. The material in the central uplifts of both ancient impact structures on earth and high-explosive craters is displaced upward from its original position (Roddy, 1968). Horizontal displacements of the material that form central mounds are probably inward in the deeper regions and outward in the shallower regions (Howard et al., 1972; Milton et al., 1972). Shatter cones are frequently found in the central uplifts (Dietz, 1968; Roddy, 1973), indicating that maximum stresses were on the order of, but above, the

Hugoniot elastic limit of the material. Central mounds do not occur in craters formed in very porous material.

Central Peaks in Hypervelocity Impact Structures. Central uplifts have been observed in many structures that have effects which are commonly associated with sites of hypervelocity impact events on earth (Dietz, 1968). Roddy (1968) examined one of those structures, that was 2.3 miles in diameter, at Flynn Creek, Tennessee (Figure 2). He found that, in the center, Stones River and Knox strata occur as folded, faulted, and brecciated material which form a hill with a top about 370 ft above the original crater floor. This hill had the general structure of a domed megabreccia block with 100 ft of the Knox formation, now exposed as steeply dipping strata, raised 1100 ft above its original position. Where the base of the mound intersected the bedded breccia on the crater floor, the hill was almost 3000 ft in diameter with sides sloping an average of  $15^{\circ}$ . Similar upward displacements of the material in central mounds were observed at the Wells Creek Structure, Tennessee (Stearns et al., 1968); Sierra Madera, Texas (Howard et al., 1972); and Gosses Bluff, Australia (Milton et al., 1972).

Some evidence of inward displacements at depths also existed in many of the structures. Howard et al. (1972) suggested that individual beds in the Sierra Madera uplift were faulted and folded to an extent that the total strike length of each bed was greater than the perimeter on which it lies. This shortening may have been as great as 25% in some stratigraphic sections, although this estimate was based on the possibly invalid (Milton

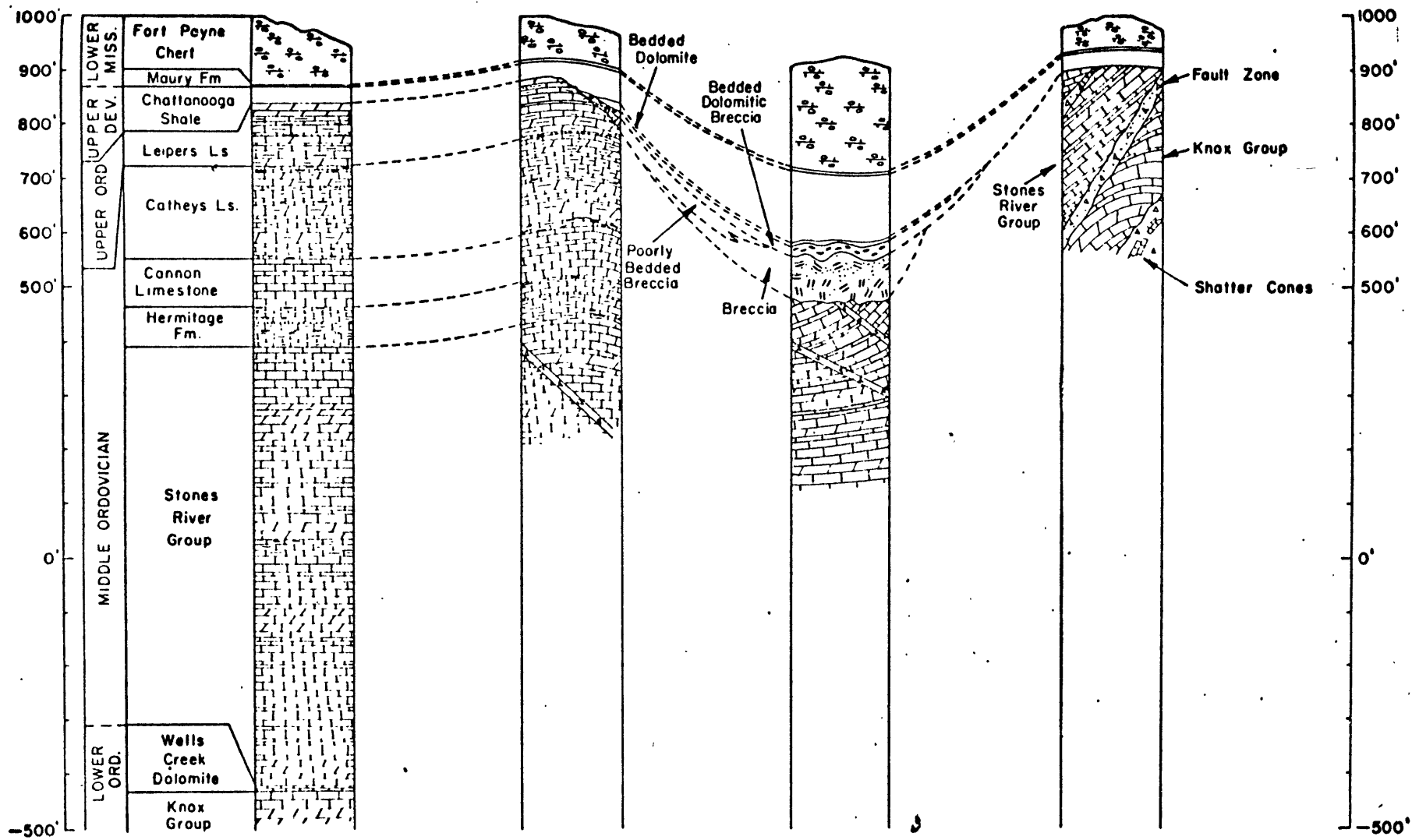


Figure 2. Generalized stratigraphic sections from the western side of the Flynn Creek structure (after Roddy, 1968).

and Roddy, 1972) assumption that the displacement of each segment could be resolved into translation plus rotation about no more than one axis. Also, stratigraphic beds appeared to have been thickened such that near-vertical beds, which were no more than 1200 ft thick, filled a minimum width of 5000 ft.

The orientation of shatter cones (shatter cones will be discussed later) has also been used as a measure of inward displacement (Milton et al., 1972). Measurements of such orientations at Gosses Bluff, when a common shock focus was assumed, indicated that inward displacements were from 20 to 52% of the original radial distance from the center, with the deeper strata displaced inward more than the shallower strata. However, these estimates could be significantly reduced if the shock was produced by a vertical line source. A complete elimination of inward displacements would require that the line source was 6300 ft long. If the relation that upper beds moved inward relative to lower, as suggested by Howard et al. (1972) based on fold patterns at Sierra Madera, is also valid at Gosses Bluff; then the assumption of a common source results in an incorrect relation of displacements between strata, and quantitative estimates that are based on that assumption are not valid.

While evidence of inward displacements in the deeper regions is not complete, outward displacements in much shallower regions are observed. For example, at Gosses Bluff the upper ends of layers lie as overturned plates or detached blocks on the truncated edge of stratigraphically higher units (Milton et al., 1972). In addition, 330 ft long blocks of sandstone lie 1000 ft

from their stratigraphic outcrop, indicating an outward ballistic flight.

The peak shock pressures experienced by the material in central mounds can be estimated on the basis of the occurrence of shock effects. One macroscopic shock effect, already mentioned, is the shatter cone. Dietz (1968) describes shatter cones as cup-and-cone structures with striated surfaces that radiate from small half-cones on the face of a master cone. They are most common in carbonate rocks, but are also known in shale, sandstone, quartzite, and other lithologies. They frequently occur in central uplifts, as shown in Table I, indicating that conditions favorable to shatter-cone formation are experienced in that material. A theoretical study of shatterconing (as reported by Dietz, 1968) shows that shatter cones are shock fractures formed along a travelling boundary between the plastic and elastic response of a material defined by the dynamic elastic limit, with the plastic domain moving relative to an elastic domain. The analysis is consistent with the observations that shatter cones appear to be formed prior to significant material displacement, and high pressure phases (coesite, stishovite, maskelynite) have not been found associated with shatter cones. Thus, shatter cones, and by association central mounds, appear to be formed in material where the shock pressures were close to, but above, the Hugoniot elastic limit.

An extensive study of circular structures that have effects consistent with hypervelocity impact sites has led Dence et al. (1968) to conclude that there is a critical crater size required

Table I  
 STRUCTURES WITH SHATTER CONES  
 IN CENTRAL UPLIFT  
 (Dietz, 1968)

<u>Structure</u>	<u>Location</u>	<u>Rock Type of Shatter Cones</u>
1. Steinheim Basin	Germany	Limestones
2. Wells Creek Basin	Tennessee	Dolomite
3. Crooked Creek	Missouri	Limestone
4. Serpent Mound	Ohio	Limestone
5. Flynn Creek	Tennessee	Limestone
6. Sierra Madera	Texas	Limestone
7. Verdefort Ring	South Africa	Granite
8. Clearwater Lake West	Quebec, Canada	Granitic Gneiss
9. Sudbury	Ontario, Canada	Quartzite, Shale, Granite
10. Manicouagan-Mushalagan	Quebec, Canada	Crystalline Gneisses
11. Gosses Bluff	Australia	Limestone, Sandstone, etc.

to form central uplifts in granitic gneisses. Information from structural mapping, gravity surveys, and drilling, combined with evidence of previous shock-wave experience in materials, has indicated that there are at least 12 shock-produced craters on the Canadian Shield. The smaller of these craters, with diameters of 2.5 miles or less (Brent, Holleford, New Quebec craters), have a bowl-shaped structure with no central uplift. The craters with diameters greater than 5.5 miles (Deep Bay, Clearwater Lakes, Carswell Lake), however, show a complex structure which includes a central uplift, an annulus of brecciated rock, and a peripheral depression which surrounds the crater.

Observations of the occurrence of central mounds on the Earth, Mars, and the Moon have been interpreted to show that gravity has an influence on the occurrence of central peaks (Hartmann 1972, 1973). Hartmann (1972) suggested that data on the size distribution of craters with central peaks as a function of crater diameter, Figure 3, indicated that central peaks tended to form in craters of smaller diameter as gravity increased; although the statistical base for the Earth data was only 33 cryptovolcanic structures. He suggested the relationship was

$$D_c \propto g^{-1.25 \pm 0.2}$$

where  $g$  was the gravitational acceleration and  $D_c$  represented either the minimum diameter for craters with central peaks or the diameter of craters with the maximum frequency of central peak occurrence. The data also showed, however, that the inferred minimum diameter of craters with central peaks was significantly

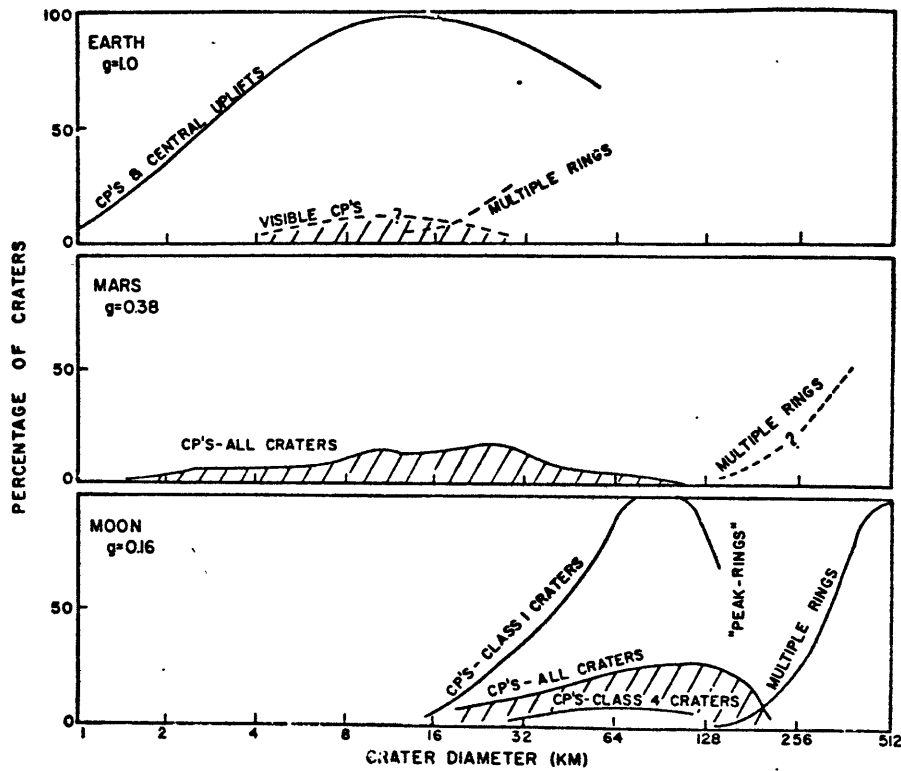


Figure 3. The size distribution of craters with central peaks on the Earth, Mars, and the Moon. Solid line on Earth data includes structural uplifts in astroblemes and is based on a total of 33 structures (after Hartmann, 1972).

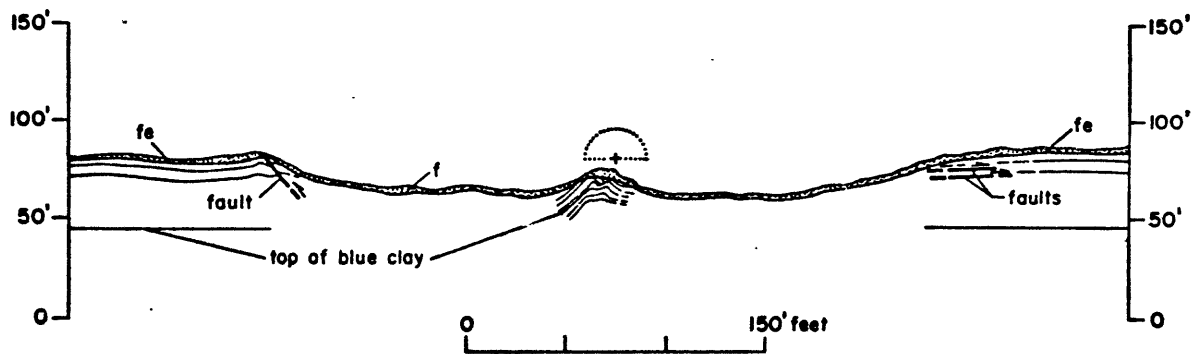


Figure 4. Cross section of the crater produced by the 500 ton TNT event Snowball (after Roddy, 1968).

different from the diameter at maximum frequency. This difference indicated that gravitational stress, while a contributory factor, was not the only cause of central mound formation.

Central Mounds in High Explosive Detonation Experiments.

Similar structural relations have been observed at central mounds in craters caused by large chemical-explosive detonations. One series of tests was located at the Watching Hill Test Range near Suffield, Alberta and was sponsored by the Defense Research Establishment of Canada. Programs during this series included Snowball, Distant Plain, Prairie Flat, and Dial Pack. The geology at the test range was characterized by a ground water table usually near 25 ft depth (Zelasko and Baladi, 1971). The presence and depth of this water table resulted in essentially a two-layer structure. The material above 25 ft depth was a low-density soil that displayed a Mohr-Coulomb yield surface with a slope near 1. The material below 25 ft depth was a denser, saturated soil that, for confining pressures less than 40 bars, had little strength dependence on confining pressure. Also, the Poisson's ratio of the material increased from 0.30 near the surface to 0.47 at 30 ft depth.

Central peaks with characteristics similar to the central uplifts observed in ancient impact structures were formed in many of the craters that resulted from the explosive tests. Roddy (1968) described the crater, Figure 4, from the 500-ton TNT event, Snowball, as shallow and flat-floored with a diameter of more than 300 ft and a maximum depth of 22 ft. The central mound, which was nearly 19 ft high, consisted of folded and

faulted clay beds in a tightly folded dome. The beds showed plastic thickening and thinning with a stratigraphic horizon lifted nearly 24 ft. During the test series at Suffield, a 20 ton spherical charge and a 100 ton hemispherical charge formed craters with no central peaks, while a 100 ton spherical charge and 500 ton hemispherical and spherical charges formed craters with central mounds (Milton and Roddy, 1972).

A series of high-explosive detonations, named Middle Gust, was performed near Pueblo, Colorado during 1971 and 1972 (Myers, 1973). This series included a total of five experiments at two sites (see Table II). One site had a 10 ft overburden of sandy clay over fractured clay shale that interfaced with competent shale 23 ft below the ground surface (Windham et al., 1973). This site was called the "wet" site because a perched water table on the top of the competent shale extended to about 4 ft below the ground surface. Two sets of nearly vertical joints existed in the competent shale. The sets were nearly perpendicular and had intervals between joints of 6 to 8 ft and 10 to 14 ft. The second, or "dry" site was 23 ft of fractured clay shale over a more competent shale with no near-surface water table. Three sets of nearly vertical joints existed in the weathered shale at the second site. The maximum strength of even the competent shale at both sites was less than 100 bars and independent of confining pressure. All the craters extended into the weathered shale, and the Middle Gust III crater reached the competent shale (Myers, 1973). All of the craters except Middle Gust III had interior mounds that were 2 to 5 ft high although the top of one of the

Table II

## Defense Nuclear Agency High Explosive Experiments

(Roddy, 1973)

<u>Experiment</u>	<u>Charge (tons TNT)</u>	<u>Charge Position</u>	<u>Test Side</u>	<u>Central Mound</u>
Middle Gust I	20	half-buried	"wet" shale	2 ft
Middle Gust II	100	elevated	"wet" shale	5 ft
Middle Gust III	100	surface tangent	"wet" shale	trough
Middle Gust IV	100	surface tangent	"dry" shale	2 ft
Middle Gust V	20	half-buried	"dry" shale	3 ft
Mixed Company I	20	half-buried	sandstone	3 ft
Mixed Company II	20	surface tangent	sandstone	7 ft
Mixed Company III	500	surface tangent	sandstone	5 ft

mounds was offset from ground zero. The mounds tended to fracture along old joint directions (Roddy, 1973). The Middle Gust III crater had a 5-ft-deep central trough in the competent shale. Roddy (1973) reported shatter cones in the Middle Gust IV and V central mounds.

An additional series of three high-explosive detonations, called the Mixed Company series, was performed near Grand Junction, Colorado during 1972 (Choromokos and Kelso, 1973). The sites for these experiments were surface layers of alluvial sandy soil over sandstone with no significant water content. The alluvial soil layer was 5 ft thick for events I and III and 1.8 ft thick (Day, 1973) for event II. The sandstone was generally weathered to a depth of 12 ft below the surface.

The craters that resulted from these experiments all had central uplifts (Roddy, 1973). The first event produced a crater with an apparent depth of 15 ft and a central peak 3 ft high. The sandstone beds in this uplift were generally intact on the flanks but were brecciated in the core. The second event produced a crater with an apparent depth of 7 ft. A very large central mound covered the crater floor and extended nearly 3 ft above the original ground level. The third event produced a crater with an apparent depth of 18 ft and a poorly formed irregular dome of massive sandstone 5 ft high. The crater floor surrounding the uplift consisted of large slabs of sandstone that sloped upward towards ground zero and exhibited both fracturing and faulting approximately parallel to the local joint pattern. A circular ring fault formed on the crater floor at the base of

the crater walls, locally separating the floor from the walls. Carnes (1973a) reported that permanent displacements in the sandstone beyond the crater walls were primarily upward and outward.

Craters Without Central Peaks. Central mounds are not observed in all shock-produced craters. In particular, there is a notable lack of central peaks produced by nuclear detonations at the Nevada Test Site (Roddy, 1968) and at Eniwetok and Bikini Atolls in the Pacific (Circeo and Nordyke, 1964). Such nuclear experiments included detonations with yields from a kiloton to over 10 megatons and shotpoint locations that were deeply buried, near surface, and above surface. The test sites were dry alluvium at the Nevada Test Site and unconsolidated sands and gravels over coral reefs in the Pacific. The common geologic characteristic of these sites is the porous structure of the cratered materials. The medium beneath the Barringer Crater in Arizona, a meteorite impact crater with no central mound, is porous sandstone (Shoemaker, 1963). Also, craters without central mounds were produced in impact craters formed in dry, noncohesive quartz sand during laboratory tests (Gault et al., 1968).

#### Previous Computational Programs

Several attempts have been made by others to numerically simulate shock-wave-cratering events. These attempts have shown that the ground-motion history during a simulation was sensitive to the amount of material compaction that was modeled for a complete cycle of stress loading and unloading. A second

important feature of the simulations was that the motion caused by the simulated shear wave was toward the axis of symmetry.

Distant Plain 6 Simulation. The coupled Eulerian - Lagrangian computer code, called ELK, was used for three attempts to numerically simulate the crater and central mound produced by the 100 ton, surface-tangent high-explosive experiment, Distant Plain 6 (Christensen et al., 1968; Christensen, 1970). The material models for all three of the calculations were based on reported test-site data; however, only one of the simulations, ELK 31, included a precompaction model beneath, and as a result of, the 100 ton explosive charge. The ELK 31 calculation was continued until a simulated time of 220 msec, Figure 5, and showed the development of upward velocities near the axis of symmetry after 160 msec. At 220 msec the flow pattern showed that material near the crater boundary at the 20 ft range was moving down and toward the vertical axis. This motion resulted in a vortex pattern centered at a range of 12 ft. Extension of this flow pattern, accomplished by extrapolating deceleration, resulted in calculated crater dimensions at a simulated time of one second that were consistent with the observed crater. The other two calculations were stopped by a simulated time of 125 msec because the computed depths of the craters were too great. Christensen (1970) concluded that causes for the upthrust included the airblast-induced shear wave interacting at the axis of symmetry, the effect of gravity, and the compaction cone that resulted from quick settlement under the 100 ton explosive load, but he did not determine the contribution of each cause.

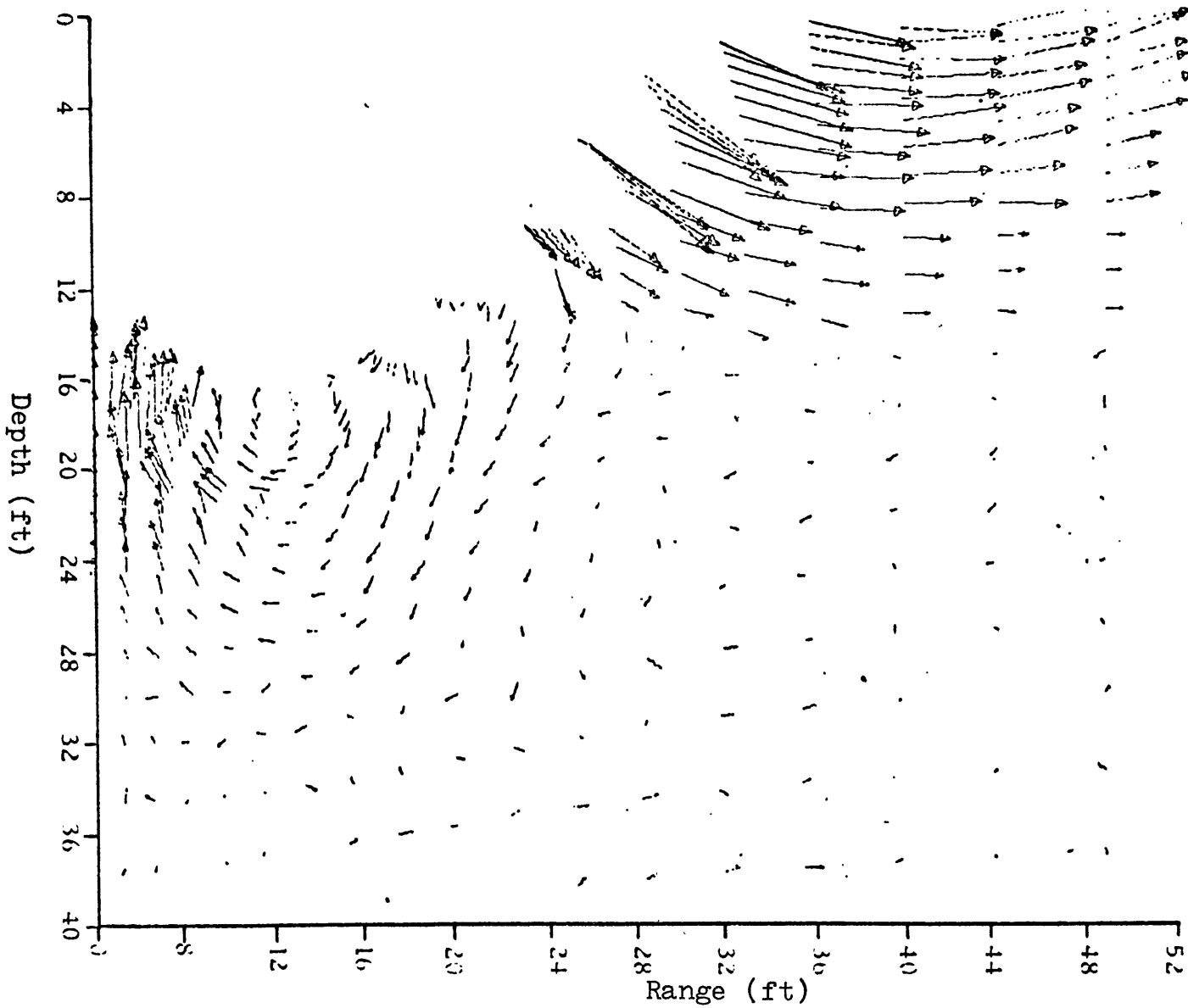


Figure 5. Velocity vectors at a simulated time of 220 msec for the Distant Plain 6 calculation (after Christensen et al., 1968).

Mine Under Simulation. A numerical simulation was also accomplished to model the test event Mine Under (Maxwell and Moises, 1971a). The event was the detonation of a 100 ton spherical charge of TNT over granite. The charge was centered at a height of two charge radii to produce only airblast loading on the ground. The test site was composed of weathered granite with a compressional wave speed of 10,000 ft/sec and a shear wave speed of 6100 ft/sec. Sample porosities varied a factor of two from a mean value of five percent. This porosity resulted in a residual compression, after a cycle of compressive loading and unloading, of 20% of the peak compression for peak pressures below 43 kbar. A complex yield model which included brittle fracture and sliding on cracks was also included in the calculation, with a von Mises limit of 30 kbar reached by a pressure of 24 kbar. The results of this calculation showed that the calculated shear wave, supported by the strong rock model, caused a clockwise rotation in the material flow pattern. However, data from instrumentation in the actual event did not indicate such a substantial shear wave. Maxwell and Moises concluded that the in-situ rock strength was much lower than the strength included in the model.

Sierra Madera Simulation. A numerical simulation of the event which may have formed the Sierra Madera formation was also accomplished by Maxwell and Moises (1971b). For this simulation a sphere with a radius of 328 ft and a velocity of 19 miles/sec was assumed to impact vertically on a halfspace. Both the sphere and the halfspace were assumed to be composed of

the same material, which had an assumed density of 2.7 gm/cc. The parameters of the material equation-of-state were based only on Hugoniot data for basalt. The yield model was a 0.2 kbar von Mises limit until a calculational zone experienced zero pressure, after which that zone was assumed to have no shear strength. The calculation resulted in upward velocities below the impact point by a simulated time of 5.5 sec with a toroidal flow pattern developed by 9.5 sec that continued until the calculation was terminated at 30 sec. Maxwell and Moises concluded that the dominant driving force of the central uplift was the release of the overburden by excavation. The entire flow pattern after 5.5 sec, however, could be explained by the flow of a liquid under the influence of gravity.

Nuclear Explosion Simulation. A series of calculations, called REVROC, was completed at the Air Force Weapons Laboratory (AFWL, 1973) to study the effects of layered bedrock on calculated near-surface ground motions caused by a simulated nuclear explosion. A two-dimensional, axisymmetric computer code was used for the simulation. Material models included irreversible compaction after a cycle of loading and unloading. The results showed that, by 0.5 sec, the calculated flow field included upward motion near the vertical axis of symmetry. These motions seemed to be caused by the primary shear wave and occurred even in the bottom layer of material. Also, the motions were a function of the amount of irreversible compaction included in the model, with less compaction favoring more upward motion.

Middle Gust III Simulation. Port and Gajewski (1973)

performed a numerical parametric study to examine the causes of major discrepancies between the ground motions calculated using pretest models of the Middle Gust III event and ground motions measured during the experiment. The main discrepancy was the failure of the numerical calculations to simulate accurately the arrival and magnitude of the large direct-induced ground shock which dominated the experimental motion. Three alternate material models were evaluated in their calculations. The first, or laboratory, model was based on detailed laboratory uniaxial-strain tests on samples of materials obtained from site drill cores. The second, or CIST, model was based on cylindrical in-situ test results of the Middle Gust site. The CIST test was used to determine dynamic moduli of in-situ materials by measuring the ground motions caused by a cylindrically symmetric shock input (Davis, 1973). The third model was based on seismic velocity data of the site and was referred to as the Seismic model. The first two models included irreversible compaction after a load-unload pressure cycle, while the seismic model was incompactible. The velocities of large-amplitude stress waves implied by the models were lowest for the laboratory model and highest for the seismic model. The same equation-of-state was used for high pressures in all three models.

The results of the parametric study showed that the laboratory model was inadequate. That model resulted in wave speeds that were one-third to one-fourth of the values required to match the arrival time of strong ground-motion signals. Further, that model failed to produce the magnitude of the peak upward veloci-

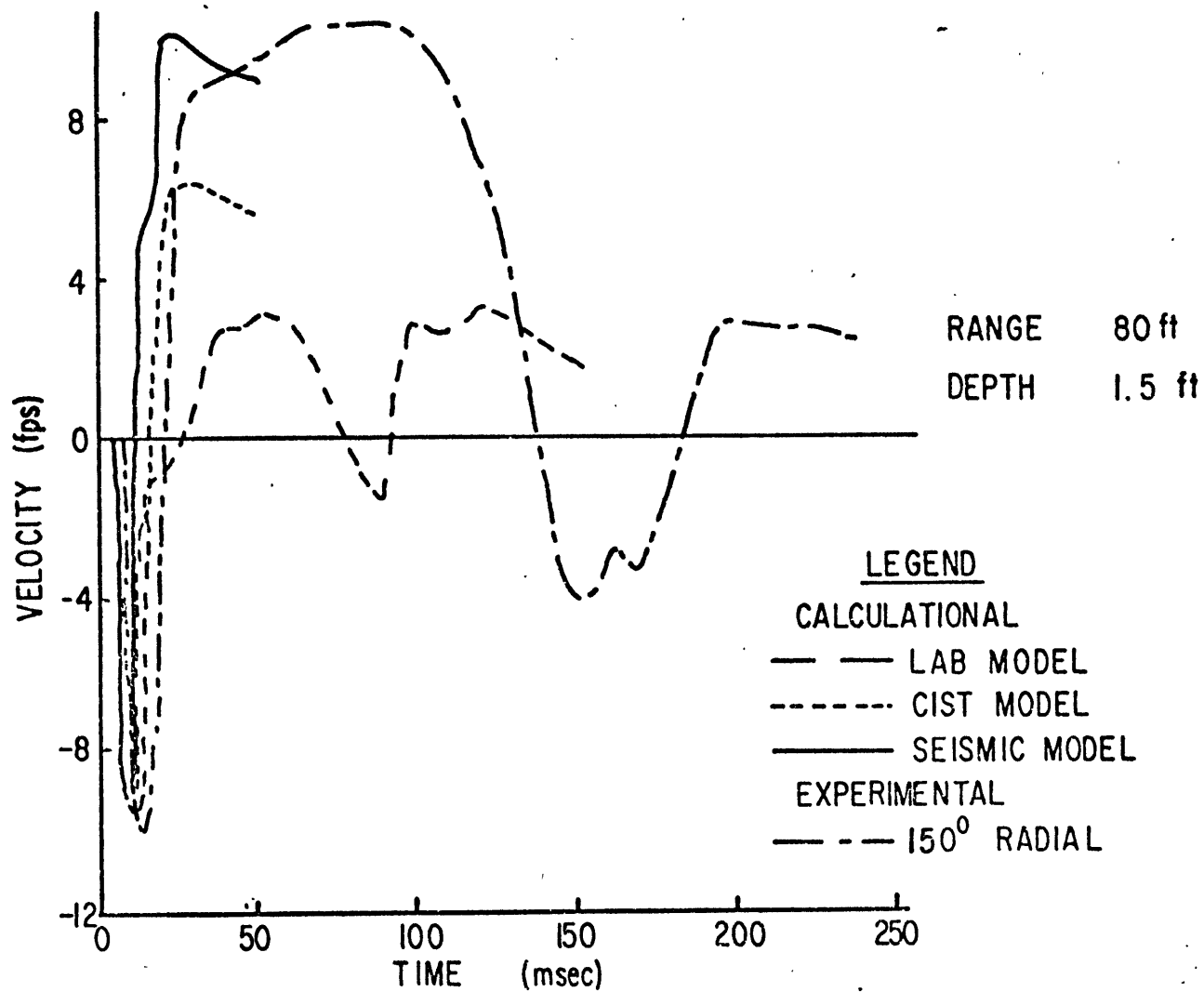


Figure 6. Vertical velocity comparison between Middle Gust III experimental measurement and three material models. Termination of model lines indicate end of calculation. Positive velocities indicate upward motion (after Port and Gajewski, 1973).

ties near the surface caused by the direct-induced wave, Figure 6. The shock arrival times that were measured above 23 ft depth were most consistent with the CIST model calculation. The data from instruments placed below 23 ft indicated wave speeds greater than even the seismic model. The peak upward velocities near the surface were matched only with the seismic model. The crater profiles predicted for all three models were nearly the same, with a maximum depth below ground zero near 17 ft, while the observed depth was 21 ft.

#### Postulated Mechanisms

Several mechanisms have been proposed to explain the formation of central peaks. These mechanisms may be broadly divided into 1) effects related to stress waves and 2) rapid gravitationally-controlled adjustments of the walls of an initial crater. The first of these broad divisions includes rebound, stress-wave reflections, shear-wave effects, and special boundary conditions caused by the impact of low-density bodies. The second division includes deep gravitational sliding and Rayleigh jet formation.

Stress Wave Related Mechanisms. The rebound of material below the crater following the compression by the shock wave was suggested by Boon and Albritton (1938) as the primary mechanism for forming central mounds. This rebound results from the acceleration of material toward the stress wave source as a result of the decreasing stress gradient that extends to the free surface. Baldwin (1963) used a set of two very-small-scale explosive experiments to examine this mechanism. In the first,

a 40 grain dynamite charge was detonated 1 inch below the surface of a specially built-up volume of soil. A box 3 ft square and 1 ft deep was filled with soil. The bottom 6 inches consisted of ordinary soil. Above this soil were six horizontal layers of colored soil, each 1 inch thick, with each layer lightly tamped into place. The second test was a repeat of the first with the soil colored into vertical layers. From these two tests a composite crater, Figure 7, was determined. Baldwin concluded that a flat area in the center of the crater was an incipient central cone formed by rebound. This conclusion was reached because some of the horizontal white layer was found above the red layer and partially under the gray layer. This white material was of lower-than-normal density, while the yellow and white layers below it were denser than normal. Dence (1968) also mentioned that unloading of materials after the shock wave might influence central mound formation, but did not emphasize this mechanism because of the small increase in specific volumes for materials subjected to shock pressures of less than 100 kbar.

Short (1965) proposed the reflection of stress waves from material discontinuities as an explanation for the occurrence of central peaks. This mechanism was based on the partial reflection of the initial shock wave from surfaces where the acoustic impedance changes discontinuously. These reflected waves, upon returning to the crater, would reflect again from the free surface as tensile waves, producing an upward heave that would be maximum near the center. Short also suggested that, if such an effect did result in central peaks, then the

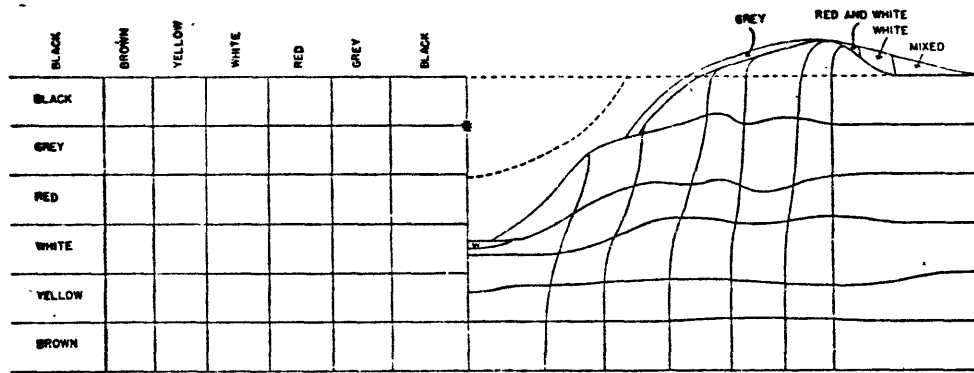


Figure 7. Composite crater profile constructed from the detonation of two 40-grain dynamite charges with the shot point at the base of the black layer. The curved dotted line gives the limit of the volume from which the soil was actually blasted from the crater. The lens at the bottom of the crater is white material of lower than original density (after Baldwin, 1963, pg 120).

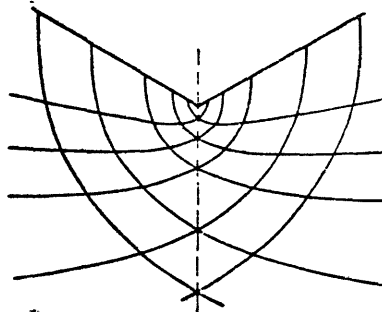


Figure 8. Theoretical lines of slip under a valley with sides dipping at  $30^\circ$  to the horizontal (after Dence, 1968).

presence of such peaks on the moon implied at least a zone of higher acoustical impedance below the lunar surface.

As an example, Short made a limited calculation of the effect of this mechanism during the impact that formed the East Clearwater Lake crater in Canada. He estimated that the shock pressure from such an event would attenuate to a kilobar at a depth of 19 miles, and, if totally reflected, would still be several hundred bars upon return to the crater base. Beals (1965) discounted this mechanism because much less than total reflection would occur. Beals based his conclusion on the tables of Muskat and Meres (1940), from which he inferred that for an elastic wave reflecting from the crust-mantle discontinuity only about 0.25% of the energy would be reflected.

The inward motion of material behind the primary shear wave has also been suggested as a cause of central peaks (Port, Air Force Weapons Laboratory, personal conference, 1973). The motion behind that wave would force material into a smaller volume about the vertical axis through the center of the crater, because the shear wave would be symmetric about that axis. This squeezing effect would tend to cause upward velocities in a manner similar to squeezing toothpaste from a tube. This effect was evident in calculations, similar to the REVR0C study, that showed upward motions began where the calculated shear wave intersected the axis of symmetry. Also, as was noted earlier, Christensen (1970) observed this mechanism in the ELK 31 calculation.

Milton and Roddy (1972) suggested that the occurrence of a central peak in an impact crater may indicate a low-density

impacting body such as a comet. They stated that a necessary condition for central peak formation may be the initial deposition of energy near the surface, and not at some depth. This condition may be required because central peak formation depends on a complex interaction of the shock wave with the free surface. If a major portion of the initial energy is deposited too deeply into the target material, the region that would have formed the central peak would become involved in the crater. A central peak would form in a cometary impact crater because the comet, consisting mainly of  $H_2O$  and  $CO_2$  ices, would volatilize near the surface upon impact, while a meteorite would penetrate to some depth. They concluded that information on the percentage of impact craters with central peaks may indicate the ratio of large-scale cometary impacts to meteor impacts on the surface of a planet.

Gravitational Mechanisms. Several authors (Shoemaker, 1963; Dence, 1968; Gault et al., 1968) have suggested that a cause of central peak formation is a deep sliding, or base failure, resulting from the gravitational stresses produced by the difference in height between the rim and the center of a crater. Dence (1968) referred to a solution, Figure 8, which showed that, under a valley with walls sloping at  $30^\circ$ , the earth movement would occur along slip lines that form two families of parabolas with the bottom of the valley as the focus and the apices within the moving material. In the cratering case, Dence assumed the slip lines would be replaced by coaxial surfaces that retained the upward turning beneath the center of the crater.

Motion along these slip surfaces would be resisted by the shear strength of the medium. There would, therefore, be a minimum crater size for any medium below which no such motion could occur. He described the formation of a crater with a central mound as proceeding from a primary crater by the walls sliding down and in along deep slip surfaces forcing the material under the crater to bulge.

Dent (1974) has also considered the failure mode of the walls of a crater. These modes of failure are "slope failure", in which the failure surface emerges in the crater wall, and "base failure", in which the failure surface extends deeply below the bottom of the crater. He accomplished an elastic plane-strain analysis of the stresses caused by the excavation of a semicircular cavity at the surface of a two-dimensional halfspace in a gravitational field. He concluded that, with a Mohr-Coulomb failure criterion, the slope-failure mode would be preferred for any size of excavation.

Pike (1971) suggested that central peaks may be caused by the centripetal movement of collapsed rim material similar to the Rayleigh jet produced in the transient craters in a liquid medium. Harlow and Shannon (1967) have numerically simulated the splash of liquid drops into deep pools, showing the development of these splash jets in incompressible fluids. Their results showed that the development of the central jet was caused by the gravitational collapse of the sides of the crater into the crater void provided that the scale condition  $(gR)^{\frac{1}{2}}/U_0$  was less than 0.4 where  $g$  is the gravitational acceleration,  $R$  is the radius

of the impacting drop and  $U_0$  is the impact velocity. However, these results were changed significantly when compressibility and shock processes were involved, with the process reverting to the rebound mechanism already described (Amsden, 1966).

### Chapter III. Numerical Simulation of Shock-Wave-Cratering

The high-explosive cratering experiments provided excellent opportunities to examine the causes of central mound formation through numerical simulation because 1) the preshot material properties of the medium were extensively tested, 2) the test conditions were known, and 3) the post-event structure of the craters and central mounds were carefully documented, providing strong constraints on the numerical results. The Mixed Company II event served as a particularly useful experiment because of the large size of the central mound compared to the size of the crater. This large size indicated that the central mound processes were particularly effective in this test event and reduced resolution problems associated with numerical calculations. Therefore, a series of numerical experiments was undertaken to simulate the Mixed Company II event and determine the contribution of individual mechanisms to the formation of the central mound. The results showed that the calculation of upward motions below a simulated crater was dependent on the material compaction model in the region where strength effects were significant. The results of one numerical simulation indicated that the presence of a lower "fluid" material may also cause the formation of a central mound.

#### Mixed Company II Experiment

As previously stated, the Mixed Company II experiment was the detonation of 20 tons of TNT, arranged in a spherical

charge of 4 ft radius, placed above, and tangent to, the ground surface. The Mixed Company test site consisted of a thin deposit of sandy clayey silt over a 70 ft thick section of Kayenta formation (Ehrgott, 1973). The silt, which was 1.8 ft thick at the Mixed Company II test site (Day, 1973), appeared to become slightly cemented at depth. The Kayenta is a fluvial deposit which consists of lenticular to irregularly bedded layers of fine-to-medium-grained sandstone, siltstone, and conglomerate with occasional layers or lenses of shale. The calculational models of these materials were based on properties, determined from laboratory and CIST data from the site (Gajewski, 1973), which are given in Table III. This information divided the test site, to a depth of 60 ft, into a 1.8 ft layer of alluvium over a halfspace that had three layers. The properties indicated that the material below the soil had a much higher maximum yield strength than the shales in the Middle Gust experiments.

Observed crater morphology and structural information provided the primary constraints on the numerical simulation of the Mixed Company II experiment. Detailed profiles, Figure 9, of the crater that was formed (Carnes, 1973b) showed that the apparent crater extended a maximum of 4 ft below the original ground level at a radius from ground zero of 12 ft. The crater was only approximately symmetric, with radii at the original ground level of 20 ft to the north and 22 ft to the south. The central mound, represented by true crater dimensions, extended a distance of 8 ft from the vertical axis through ground zero

Table III

## MIXED COMPANY II SITE MODEL

(from Gajewski, 1973)

<u>Property</u>	<u>Layer</u>			
	1	2	3	4
Depth to top (ft)	0.0	1.8	11.2*	19.6+
Density (gm/cc)	1.875	2.35	2.47	2.35
Compressional wave speed (ft/sec)	500	8000	9000	8000
Rarefaction Velocity (ft/sec)	1500	16000	18000	16000
Volume fraction of air filled voids	.2366	.0510	.0229	.0510
Poisson's ratio	0.25	0.20	0.25	0.20
Cohesion (bars)	0.7	68	51	68
Angle of internal friction (°)	25	35	37	45
Von Mises limit (kbar)	0.5	7.5	2.1	11.6

\* changed to 11.4 ft in calculations

+ changed to 19.2 ft in calculations

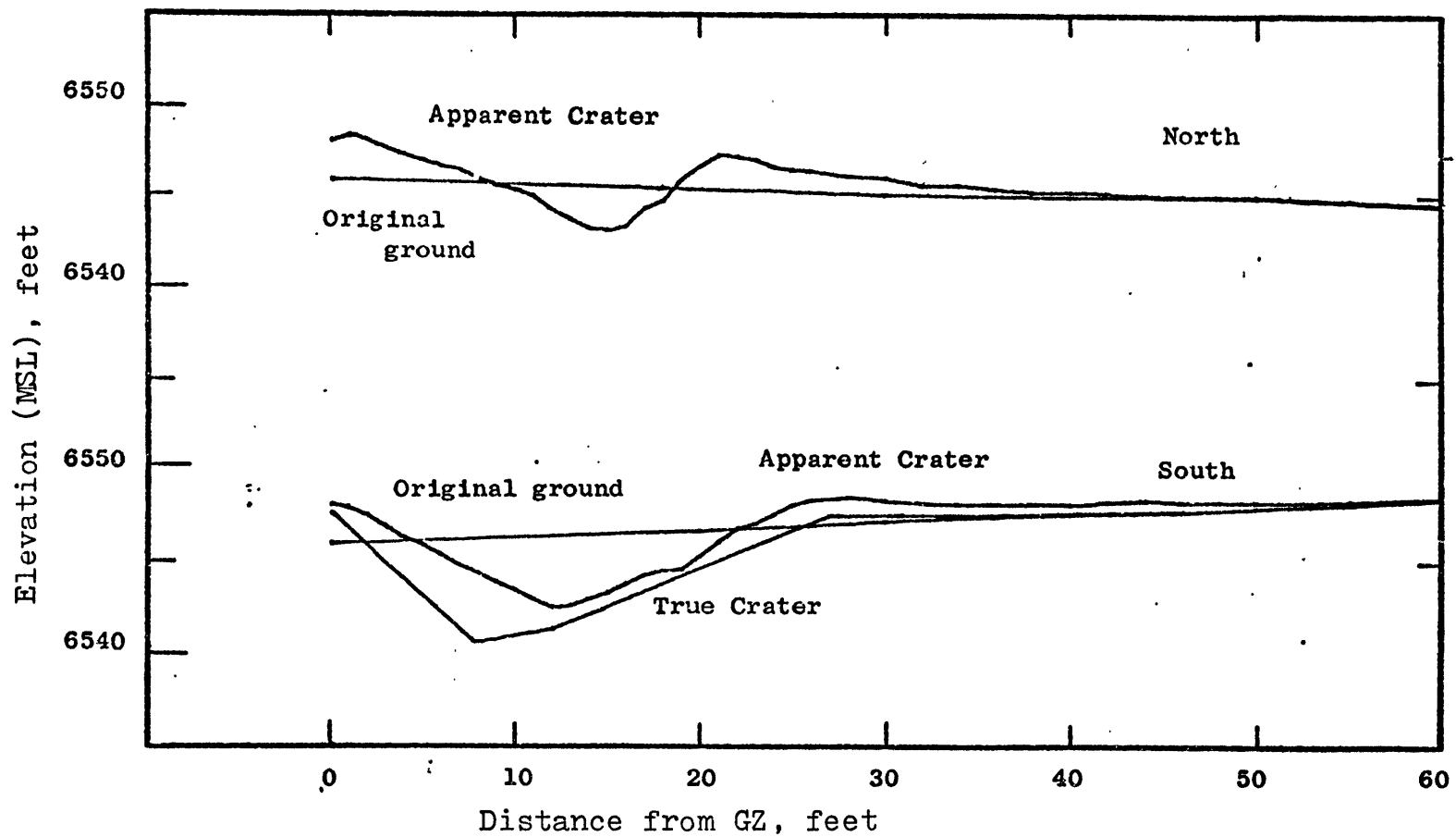


Figure 9. Apparent and true crater profiles of the 20 ton TNT event, Mixed Company II (after Carnes, 1973b).

and was 7 ft high. The mound was composed of uplifted and brecciated sandstone (Roddy, 1973). A poorly-developed overturned flap and thin blanket of ejecta surrounded the crater, and no fused material was found. Deformation in the crater wall and rim consisted mainly of shattering and local brecciation. A piece of color-coded grout, originally placed at 10 ft depth, was found 1 ft below the top of the central peak (personal conference with Major Lamping of the Air Force Weapons Laboratory in March, 1973). Ground shock instrumentation (Day, 1973) included vertical and horizontal acceleration gages at ranges of 54 and 70 ft and depths of 1.5 and 5 ft. Vertical and horizontal velocity gages were located at similar depths and ranges greater than 93 ft. The gage at 70 ft range and 5 ft depth indicated a shock arrival at 10 msec. All the data indicated that a large signal was transmitted in the material below the depth of 1.8 ft.

#### Calculational Model of Mixed Company II

The numerical simulation of the Mixed Company II experiment included the use of three mathematical models of the physical processes that were assumed to be important. The first was a model of the surface-pressure boundary condition to simulate the high-explosive detonation. The second was a computer code that modeled the initial response of the ground to the surface boundary condition. This code included approximations to physical relations and the properties of the materials at the test site. The final model was a simplified ballistic extension of the conditions that were calculated using the first two models.

Explosive Detonation Model. The explosive detonation was modeled with data from a solution of the airblast pressure as a function of range and time for a 100 ton explosive charge on a rigid halfspace (data supplied by the Air Force Weapons Laboratory, see Port and Gajewski, 1973). This information was applied using a cube-root scaling procedure to provide a surface-pressure boundary condition for a 20 ton, surface-tangent event. The procedure was to scale the ranges and time of the calculation by the ratio  $(100/20)^{1/3}$ , apply the boundary condition, and then rescale range and time by the inverse ratio.

Ground Response Model. The initial response of the ground was modeled with the AFTON-2A computer code (Niles et al., 1971). This code models two-dimensional, axisymmetric continuum mechanics problems using elastic-plastic material models that simplify to hydrodynamic expressions at high internal energies. The theory of this code (see Appendix II) is based on a specific method of constructing finite-difference approximations to the laws of continuum mechanics in integral, but not necessarily Lagrangian, form that includes artificial viscosity (von Neumann and Richtmeyer, 1950) to treat strong shock waves. This method uses relations to describe mass conservation, momentum conservation, and the first law of thermodynamics that combine to describe also energy conservation exactly. AFTON-2A is used frequently in ground-shock calculations (see for example Port and Gajewski, 1973) and the numerical errors associated with the code have been investigated extensively (Cooper, 1971; Trulio et al., 1967). All the calculations accomplished during this

study, unless specifically stated, used a Lagrangian coordinate system.

The code provides information in three forms. One form, termed a data edit, is a printed listing of selected parameters at each calculation point. The second form, called a restart dump, is a listing on magnetic tape of all the information necessary to continue the calculation from the time of that dump. While the primary purpose of this form is to provide a restart capability, these dumps also provide the information required to construct displays, termed flow field plots, of the conditions that exist in the calculation space at the simulated time of each dump. The third form is complete time history information of 100 selected "target" points. These "target" points may be considered to be "perfect" instruments which measure the forces and responses of a mass particle without influencing the behavior of that particle. They are points that may be located at any position in the calculational space, not just at calculational meshpoints, and move in a Lagrangian manner.

A description of the calculation grids is required to understand the later ballistic model and information representations. The quantities in this code are computed on two separate, but related, grids. Motion quantities (such as acceleration, velocity, and position) are computed at the designated calculation, or grid, points. Thermodynamic variables (such as stresses, strains, and internal energy) are computed at the interior of the volume defined by the four surrounding grid

points. Thermodynamic quantities are, therefore, computed and represented on a thermodynamic mesh. The combination of the two grids divides the volume surrounding the calculation point into four quarter-volumes with associated quarter masses. These quarter-volumes are also used in a ballistic extension to the code results.

The boundaries of the grid were the surface boundary, the axis of symmetry, and two transmitting-boundaries (Niles et al., 1971). The transmitting boundaries were imposed at 60 ft depth and 551 ft range and had no significant influence on the calculated motions.

One of the basic relations used to describe the material properties is the equation-of-state, which relates pressure,  $P$ , to material density,  $\rho$ , and specific internal energy. The general equation-of-state for the material models of the Mixed Company site was

$$P = f(\mu, \mu^*) \quad (3.1)$$

where the excess compression,  $\mu$ , was defined as

$$\mu = \frac{\rho - \rho_i}{\rho_i} \quad (3.2)$$

with  $\rho_i$  the initial material density and  $\mu^*$  the maximum excess-compression ever calculated at a thermodynamic mesh point. This functional relationship was divided into a low-pressure regime, for  $\mu$  less than or equal the volume fraction of air-filled voids, and a high-pressure regime. Effects of internal energy on relation (3.1) were included by adding the term  $Ae$  ( $e$  is the specific internal energy and  $A$  is a constant assumed to be  $3 \times 10^{-12}$  gms/erg) to both  $\mu$  and  $\mu^*$ . For all calculations, the

effect on pressure of this addition was small. This equation-of-state is a generalization of the Seismic model (Port and Gajewski, 1973) to allow for a permanent compaction, as in the CIST model.

The low-pressure equation-of-state was further divided into a loading relation, for  $\mu$  equal  $\mu^*$ , and an unloading relation, for  $\mu$  less than  $\mu^*$ . The loading relation was

$$P = K_L \mu \quad (3.3)$$

where

$$K_L = \rho_i c_p^2 \frac{(1+\nu)}{3(1-\nu)} \quad (3.4)$$

defined  $K_L$  for each layer from the initial density, the compressional wave speed,  $c_p$ , and the Poisson's ratio,  $\nu$ , of the material. The unloading relation allowed for a linearly changing derivative of the equation-of-state through the relation

$$\frac{dP}{d\mu} = [K_u \mu_x (\beta - 1) + K_u \mu + K_v (\mu_x - \mu)] / \beta \mu_x \quad (3.5)$$

for  $(1 - \beta) \mu_x \leq \mu \leq \mu_x$

where

$$\mu_x = \min \left\{ \begin{array}{l} \mu^* \\ \mu_3 \end{array} \right\} ; \quad \beta = \frac{2 K_L}{K_u + K_v}$$

and  $\mu_3$  represented the volume fraction of air-filled voids. The parameter  $K_u$  was defined by the relation (3.4) where  $c_p$  was replaced by the sonic velocity at the initial release of pressure,  $c_u$ ; and  $K_v$  was defined by the same relation with the sonic velocity as the pressure approaches zero,  $c_v$ . The unloading hydrostat was then

$$P = \frac{K_u [(\beta - 1) \mu_x + \mu]^2 - K_v (\mu_x - \mu)^2 + K_v (\beta \mu_x)^2}{2 \beta \mu_x} \quad (3.6)$$

after integration of (3.5). For  $\mu$  less than  $(1-\beta)\mu_x$  the pressure-density relation was assumed to be

$$P = -K_v [(1-\beta)\mu_x - \mu] \quad (3.7)$$

with the material in tension.

The low-pressure regime allowed for a reduction in the specific volume of the materials after a complete cycle of loading and unloading (Figure 10). The amount of this reduction was defined by the ratio  $\beta$  and the maximum compression experienced within the low-pressure regime. The parameter defined as

$$C = (1-\beta) \quad (3.8)$$

was the compactibility of a material. By transformations to specific volumes, the relation

$$\frac{v_i - v_0}{v_i - v_x} = \frac{v_0}{v_x} C \approx C \quad (3.9)$$

where  $v$  represents specific volume and  $v_0$  is the zero-pressure specific volume after a load-unload cycle, allows the compactibility of a material model to be estimated from graphs of pressure vs. specific volume. Initial calculations, which used the rarefaction velocity from the site data for  $c_u$  and  $c_v$ , failed to produce motions consistent with central mound formation. In the Mixed Company II numerical simulation these values, for the three deepest layers, were reduced to

$$\begin{aligned} c_v &= c_L \\ c_u &= c_L + 1000 \end{aligned}$$

which implied a compactibility of approximately 10% in those layers. The results of subsequent parametric calculations showed the effects of variations in these two parameters.

The high-pressure equation-of-state was assumed to be

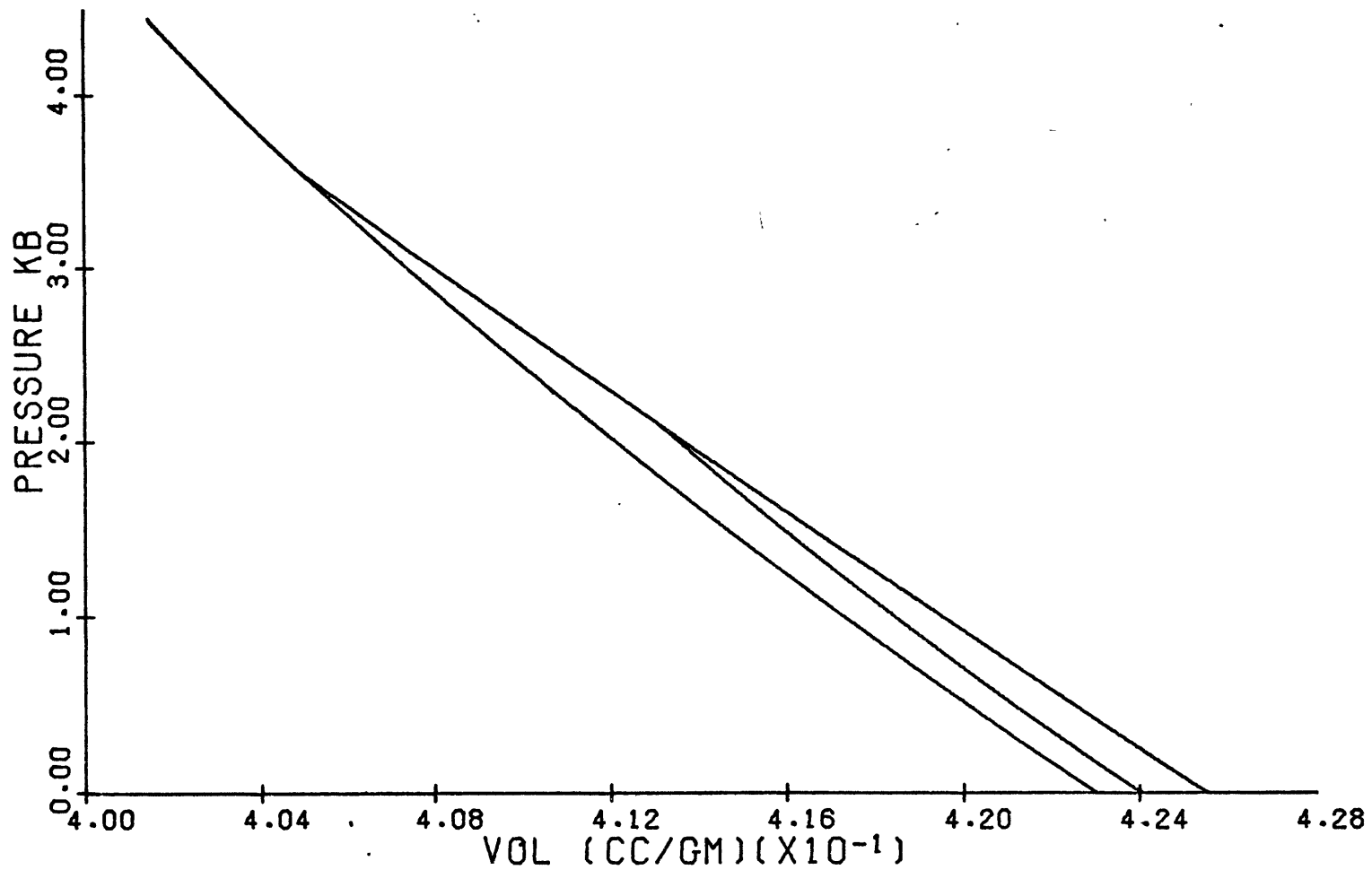


Figure 10. The model pressure - specific volume relation in the low pressure regime for Layer 2. Shown are the loading relation and unloading relations for  $\mu^*$  less than  $\mu_3$  and  $\mu^*$  equal to or greater than  $\mu_3$ .

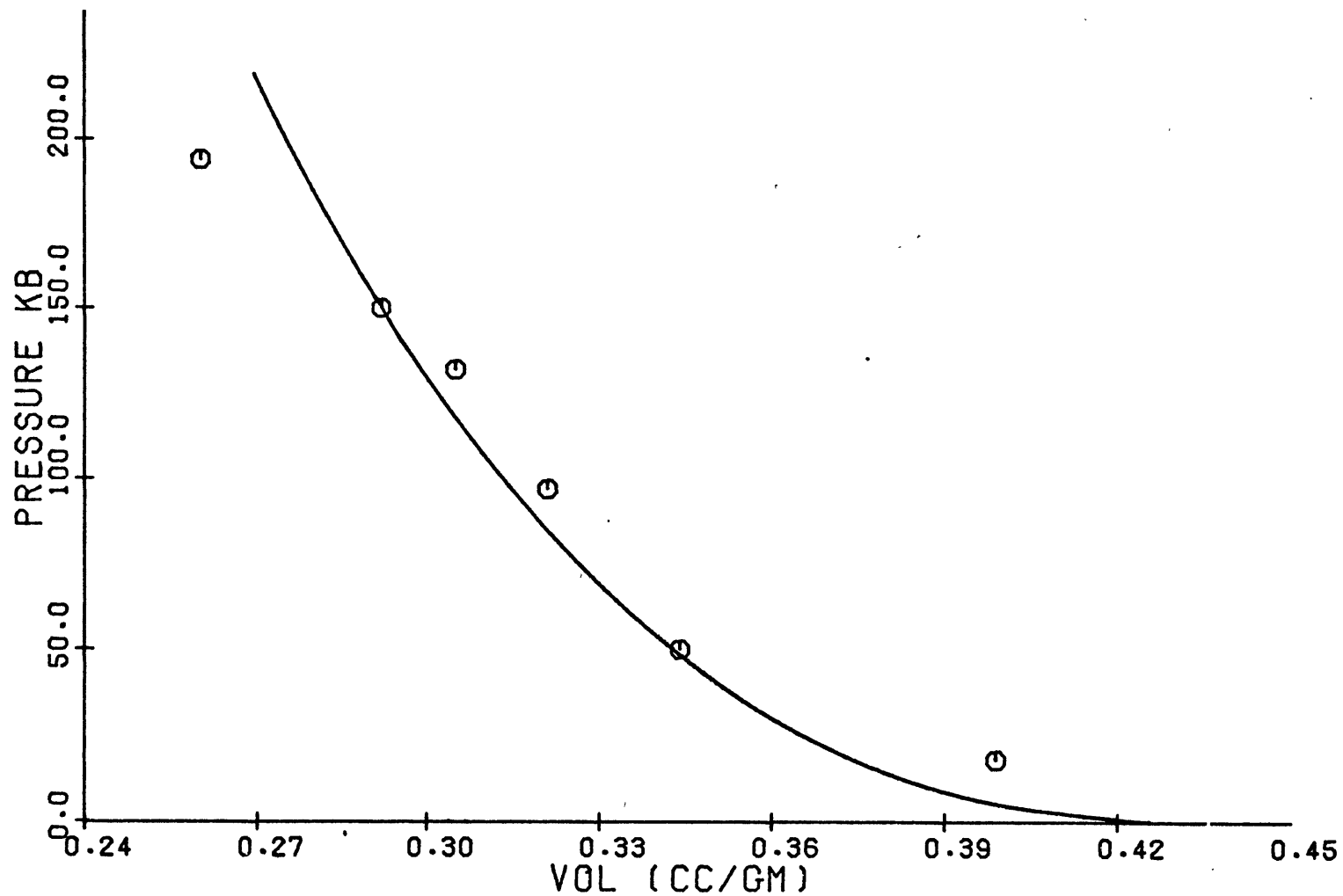


Figure 11. The model pressure - specific volume relation in the high pressure regime for Layer 2. Data points are Hugoniot information for Coconino sandstone as presented by Jones et al., (1968)

independent of  $\mu^*$ , which resulted in one relation describing both loading and unloading. The derivative of the equation-of-state in this regime was expressed by

$$\frac{dP}{d\mu} = K_m - (K_m - K_u) \exp\left(\frac{\mu_3 - \mu}{\mu_s}\right) \quad (3.10)$$

where  $K_m$  and  $\mu_s$  were parameters determined from appropriate high-pressure data. Relation (3.10) implied that

$$P = K_L \mu_3 + K_m(\mu - \mu_3) - (K_m - K_u) \mu_s \left[ 1 - \exp\left(\frac{\mu_3 - \mu}{\mu_s}\right) \right] \quad (3.11)$$

was the pressure-density relationship for this regime. The values for  $K_m$  and  $\mu_s$  were determined from Hugoniot data on Coconino sandstone at pressures above that required to close the air voids (Figure 11). The values of

$$K_m = 680 \text{ kbar}$$

$$\text{and } \mu_s = 0.3$$

provided the comparison shown in Figure 11 for layer 2, with the less porous material having lower specific volumes for pressures below 150 kbar, consistent with internal energy relations.

Although the model did not compare adequately with the data above 150 kbar, no pressure above 40 kbar ever occurred in the material during all calculations. The same value of  $K_m$ , and  $\mu_s = \mu_3 + 0.25$  were found suitable for all four layers.

The shear modulus,  $G$ , was also calculated in the equation-of-state model. In the low-pressure regime the shear modulus was determined from

$$G = \frac{dP}{d\mu} \left[ \frac{3(1-2\nu)}{2(1+\nu)} \right] \quad (3.12)$$

which allowed the Poisson's ratio to remain constant. In the high pressure regime, the shear modulus was a constant defined by

$$G = K_u \left[ \frac{3(1-2\nu_L)}{2(1+\nu_L)} \right] \quad (3.13)$$

where  $\nu_L$  was the constant Poisson's ratio of the low-pressure regime. This model is referred to as the hybrid  $\nu$  - G model (Zelasko and Baladi, 1971; Bratton, 1973).

The second basic relation used to describe the materials is the material yield surface. A simple Mohr-Coulomb and von Misses yield surface (Figure 12) that was independent of the third invariant of the deviator stresses was assumed for all materials. The yield surface,  $Y$ , was described by the relation

$$Y = \begin{cases} \tau_0 + P \tan \phi & P < P_{YLD} \\ Y_{MAX} & P \geq P_{YLD} \end{cases} \quad (3.14)$$

with  $\tau_0$  the cohesion,  $\phi$  the angle of internal friction,  $Y_{MAX}$  the von Mises yield strength, and  $P_{YLD}$  defined by

$$\tau_0 + P_{YLD} \tan \phi = Y_{MAX} \quad .$$

Material separation was assumed to occur when the value of the yield surface, for a calculation zone, reached zero. At the locations of material separation, all forces except artificial viscosity terms and gravity, were assumed to be removed. The results of initial simulation attempts indicated that, to achieve motions consistent with the formation of the observed crater, the yield description should be shifted to remove the cohesive strength of the material when the yield condition was first reached in each thermodynamic zone (as suggested by R. Port, Air Force Weapons Laboratory, personal communication, 1974). This shift was accomplished by the use of a parameter,  $S$ , evaluated for each zone, which modified the expressions containing  $\tau_0$  to

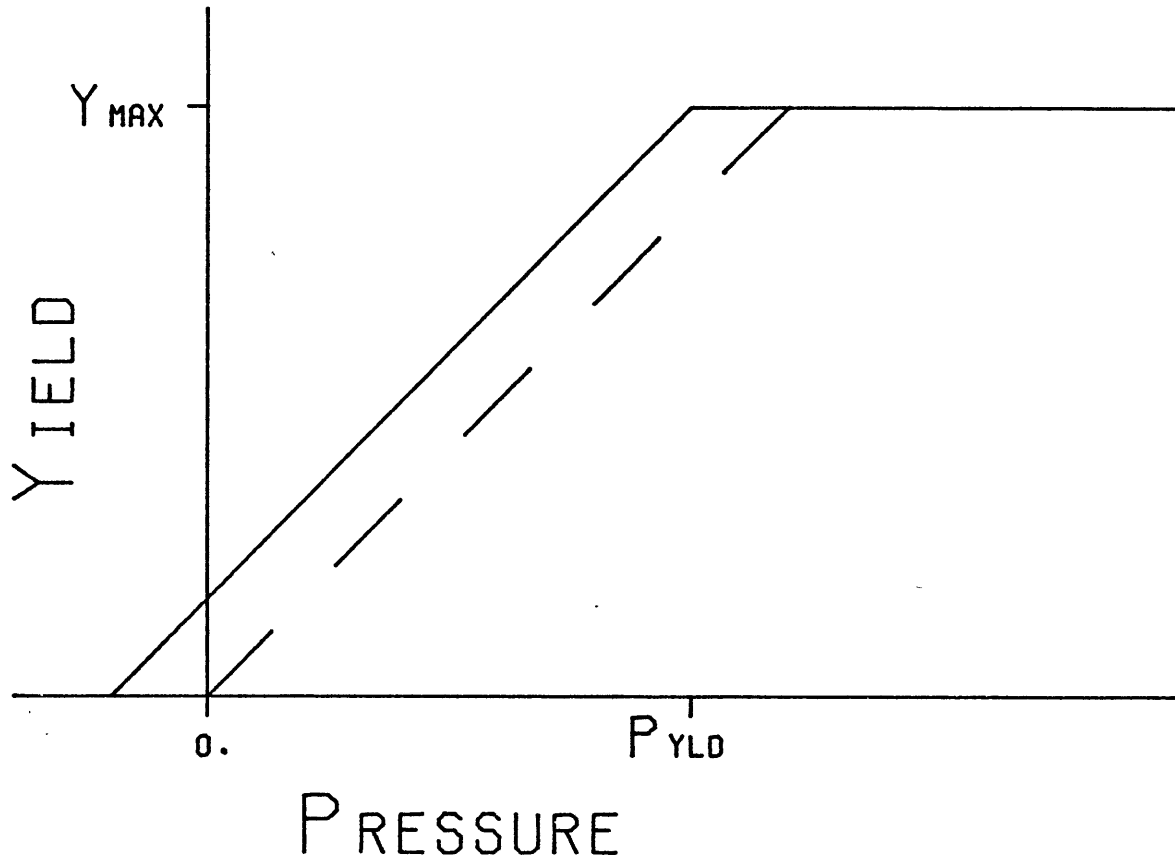


Figure 12. Schematic yield surface for materials. Solid line indicates original yield condition as a function of pressure. Dashed line indicates the shifted yield condition. No quantitative relation is expressed.

$\tau_0 (1-S)$ 

(3.15)

with  $S$  initially zero. The value of  $S$  was incremented by 0.04 when the yield condition was reached and during the subsequent twenty-four calculational cycles. The shift was accomplished in increments to avoid a drastic change in the yield surface description during one calculational cycle, which might result in calculational instability, and was always completed in less than 0.8 msec of simulated time.

Finally, a relation, called a flow rule, is required to describe the inelastic strain that occurs during flow with stress conditions limited by the yield surface. The associated flow rule (Niles et al., 1971) was used in the calculations except as will be noted. This flow rule was derived with the Method of Plastic Potential (Trulio et al., 1969) and results in a plastic volumetric increase, called "bulking", when the yield surface is a function of pressure. When the yield surface is independent of pressure, this flow rule reduces to the Prandtl - Reuss flow rule. Also, the Prandtl - Reuss flow rule was used if 1) the material was in tension, 2) the plastic volumetric strain had reached 0.1, or 3) the value of the yield surface was less than  $0.5 \tau_0$ . The first of the conditions was caused by uncertainties in the description of soil response to tension; the second condition limited the amount of bulking; and the third condition was caused by a singularity in the expression for the flow rule when the third invariant of the deviator stresses is ignored and the value of the yield surface is near zero.

The calculational grid spacing (Appendix I) was selected based on the decision that this study was primarily interested in conditions in and below the crater region. Therefore, the calculation grid and target points were concentrated in that region. Outside that region the grid spacing was increased geometrically to minimize the calculation time. This decision resulted in only limited comparisons between calculation and experiment instrumentation data.

Ballistic Extension Model. At the simulated time of 16.4 msec in the Mixed Company II calculation, the material in and below the crater region was calculated to be separated and moving ballistically (as will be demonstrated). Because of this complete separation, the AFTON calculation was stopped at 16.4 msec and a simplified ballistic analysis was accomplished to estimate the final crater shape. This analysis was accomplished for the region within 35 ft range and a depth of 20 ft with the velocity conditions at 16.4 msec as initial conditions. Each grid point was allowed to move ballistically (Appendix III) until the following three conditions were met:

- a) The grid point either immediately below or radially away was not moving,
- b) The vertical velocity was negative,
- c) The density of the material in the bottom, outward quarter-volume of the zone was at least 1.5 gm/cc.

The motion of a grid point was stopped after all these conditions, referred to as the stopping criteria, were once met.

Mixed Company II Numerical Simulation (MC 2.12)

The numerical simulation of the Mixed Company II experiment, designated MC 2.12, resulted in calculated flow-field conditions at a simulated time of 8.4 msec, Figures 13 and 14, which were consistent with the formation of a central mound. The material within a range of 12 ft and a depth of 20 ft had achieved upward velocities with the maximum vertical velocities near the vertical axis. Also, all the material within that region had separated and was in ballistic motion. A second velocity zone, centered near 18 ft range and 4 ft depth, was moving horizontally outward and again was completely separated. Only a flap of material in the top layer and beyond a range of 18 ft had significant velocities and had not separated. By 16.4 msec even this flap was completely separated, with little velocity change from the conditions that existed at 8.4 msec.

The model crater, Figure 15, was formed by 616.4 msec and a fallback phase of the problem was beginning. The radius and slope of the model true-crater wall, defined by the motionless material without extreme shear deformation, was consistent with the true crater profile. An extreme shear zone, with horizontal grid lines extending into an overturned flap, was calculated near the range of the observed southern crater wall and within the asymmetry of the apparent crater. The material below the original surface and between the uplift region and the apparent crater wall was continuing to move ballistically toward the crater wall. Also, the bottom radius of the central uplift was comparable to the deepest point of the true crater, located at a

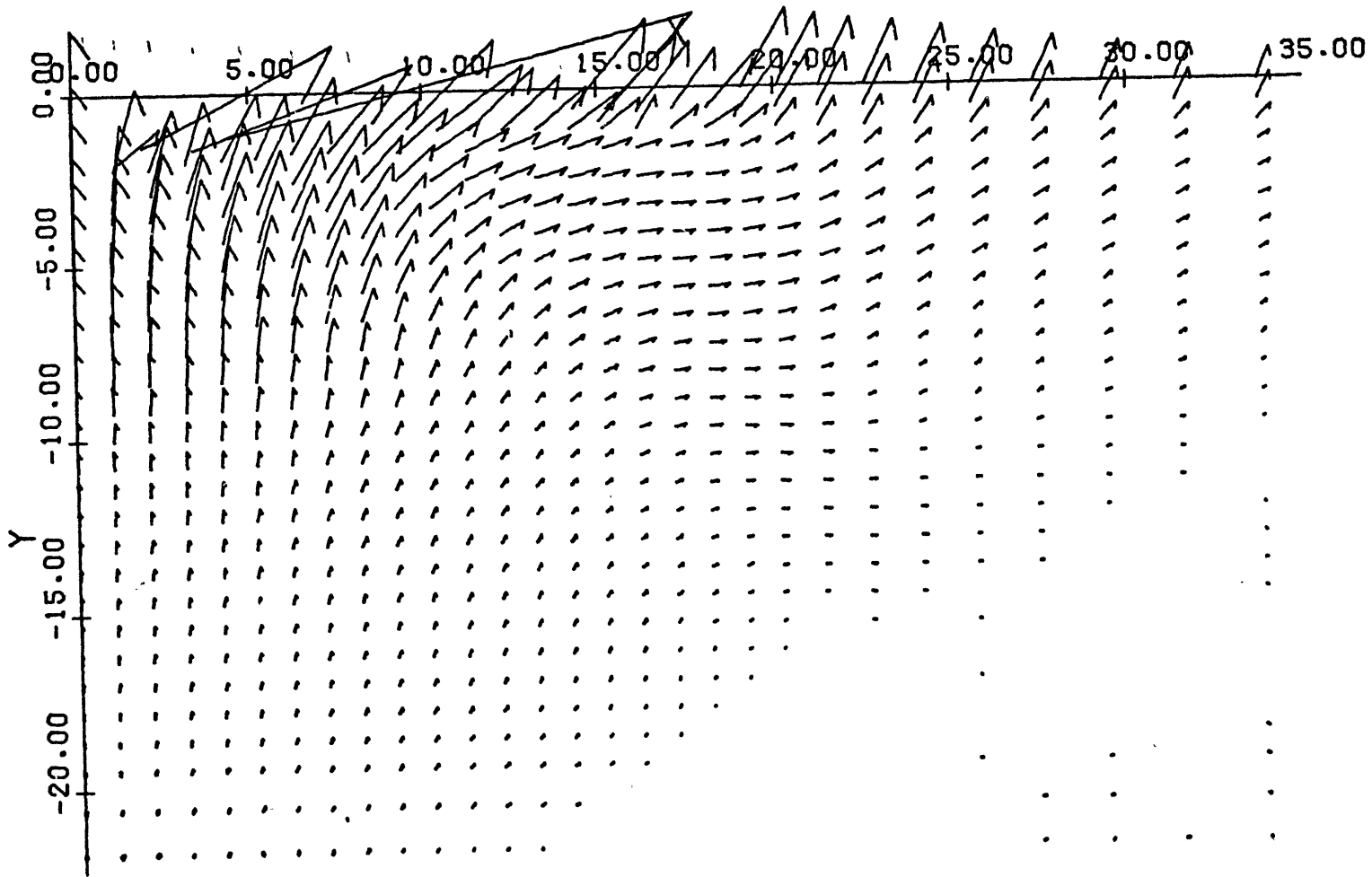


Figure 13. Velocity vector plot for MC 2.12 at 8.4 msec after detonation. Velocity is proportional to the length of the vector with the distance between axis marks equal 100 ft/sec. Axes are in ft.

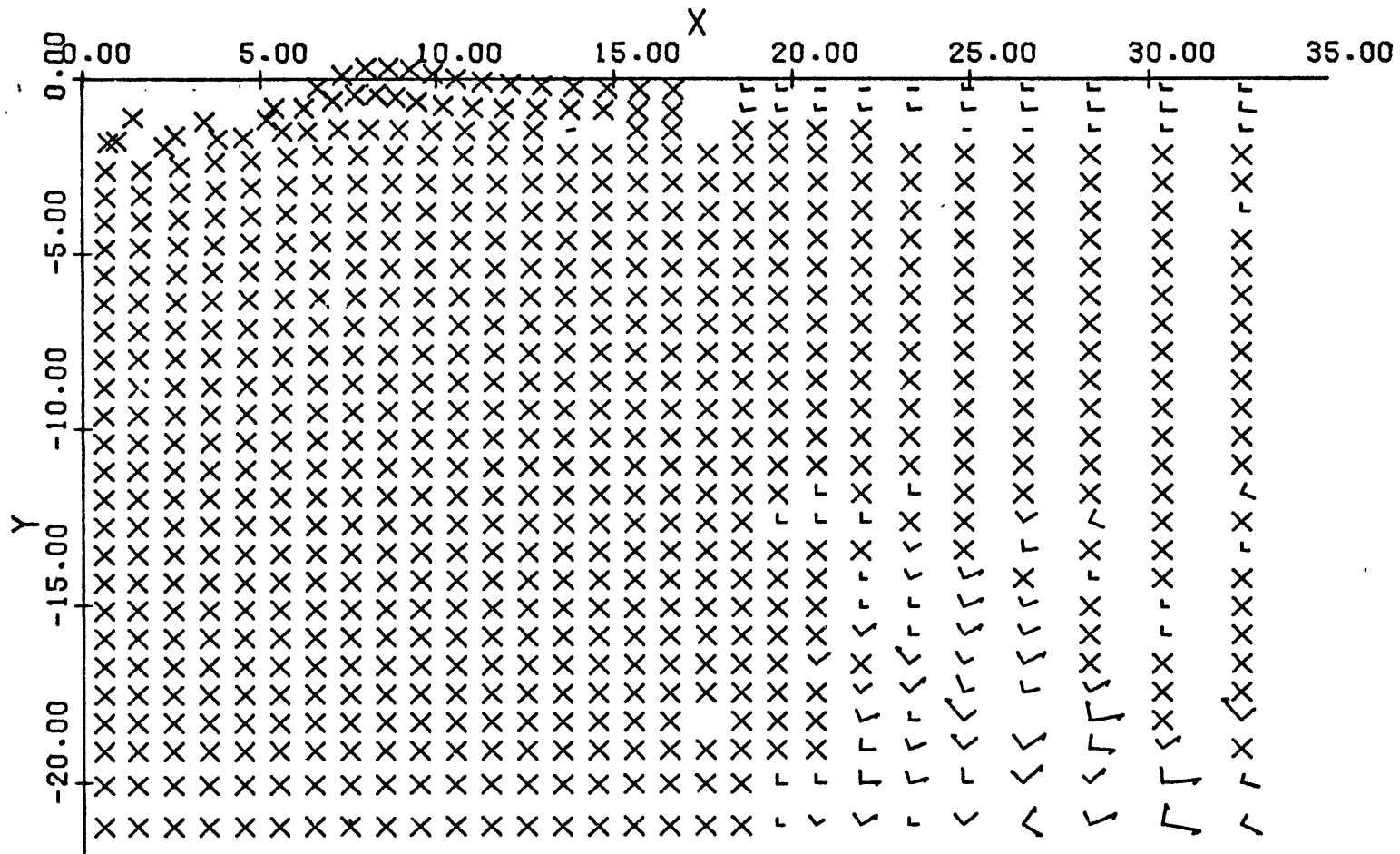


Figure 14. Principal stress axes plot for MC 2.12 at 8.4 msec after detonation. The marks, X, indicate material separation. Stresses are proportional to the square of the vector length with the distance between axis marks equal 1 kbar. All stresses are compressive. Figure axes are in ft.

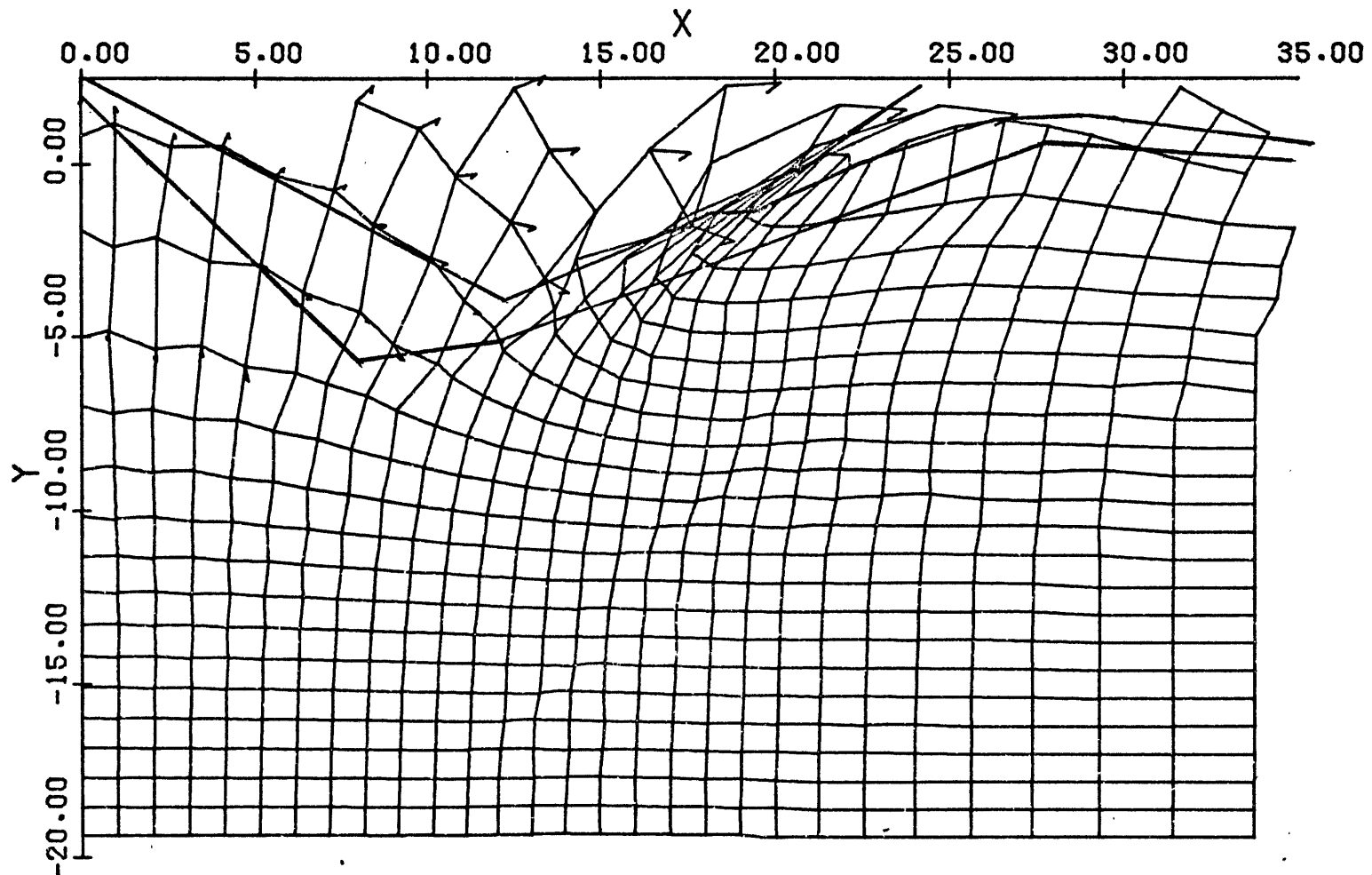


Figure 15. Calculation grid plot for MC 2.12 at 616.4 msec after detonation compared to observed apparent and true crater profiles along the southern radial of the Mixed Company II crater (Carnes, 1973b). Velocity of a grid point is proportional to the length of the vector with the distance between axis marks equal 50 ft/sec. Axes are in ft.

range of 8 ft.

Several deficiencies of the calculational results were also apparent. First, the top calculational line shown in Figure 15 at less than 30 ft range represented the interface that was initially at 1.8 ft depth, while the soil layer, even at 30 ft range, was above the 2.5 ft elevation allowed in the figure. However, the measurements of the near-surface motions in both Middle Gust and Mixed Company tests also showed initial upward spall velocities near the surface of at least 10 ft/sec caused by the direct-induced wave (Bratton, 1973; Port and Gajewski, 1973). These velocities were stopped by a second positive phase of air overpressure (Port and Gajewski, 1973) that would occur after the AFTON calculation was stopped and was ignored in the ballistic extension. The interaction of explosion products, aerodynamic forces, and particle-particle interactions rendered a ballistic treatment of ejecta distribution irrelevant. Also, the stopping of some grid points, such as the one located near the 18 ft range and the 0.0 ft depth, and the continued motion of other grid points through the crater wall showed that the stopping criteria were inadequate for model ejecta.

Another discrepancy, and of most concern to a discussion of central peaks, was that insufficient upward motions appeared to have been calculated to produce the height of the observed central mound. A continuation of the ballistic calculation resulted in the highest grid point on the symmetry axis in the figure eventually settling back to 2 ft below the original surface. As the next higher grid-point was computed to eventually

reach a height of 10 ft, the grid point in the figure probably represented the top of the calculated central mound for this model. An additional indication of the insufficient upward motion was the small upward displacement of the material at the 10 ft depth when compared to the 11 ft upward displacement of the colored grout that was placed at that depth. Possible causes for this discrepancy will be discussed after the results of parametric numerical experiments are described.

Even considering the displacement discrepancy, the results were in sufficient agreement with observations of the experimental event to warrant a description of the conditions that produced the velocity field calculated at 8.4 msec. These conditions were shown by calculation-space plots, Figures 16 and 17, at a time of 3.0 msec. The velocity-vector plot showed that a strong clockwise-rotational velocity wave had reached a depth of 14 ft near the vertical axis. Along the vertical axis the motion changed from downward to upward at 12.6 ft depth, or immediately behind the intersection of the rotational motion with the vertical axis. Motion behind the wave was upward, with inward and outward oscillations occurring closer to the origin. The acceleration-vector plot showed clearly the wave structure in the flow field. The accelerations beyond a radius of 24 ft were directed radially outward, except in the near-surface airblast region, and indicated the location of the compressional wave. The acceleration reversal, at a radius of 24 ft from the origin, indicated the location of maximum compression. All material within that radius was recovering from maximum compressions and

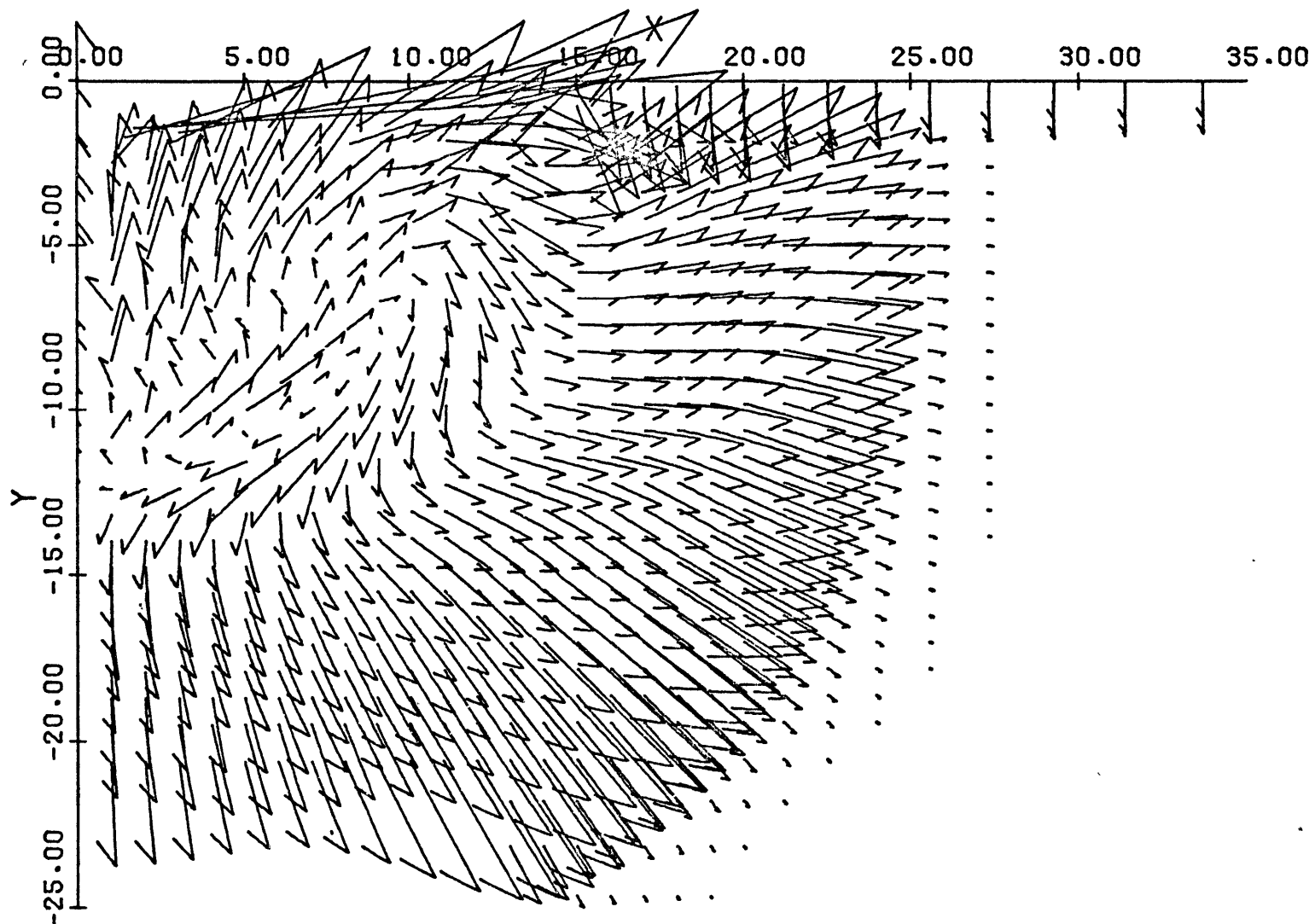


Figure 16. Velocity vector plot for MC 2.12 at 3.0 msec after detonation. Velocity is proportional to the vector length with the distance between axis marks equal 100 ft/sec. Axes are in ft.

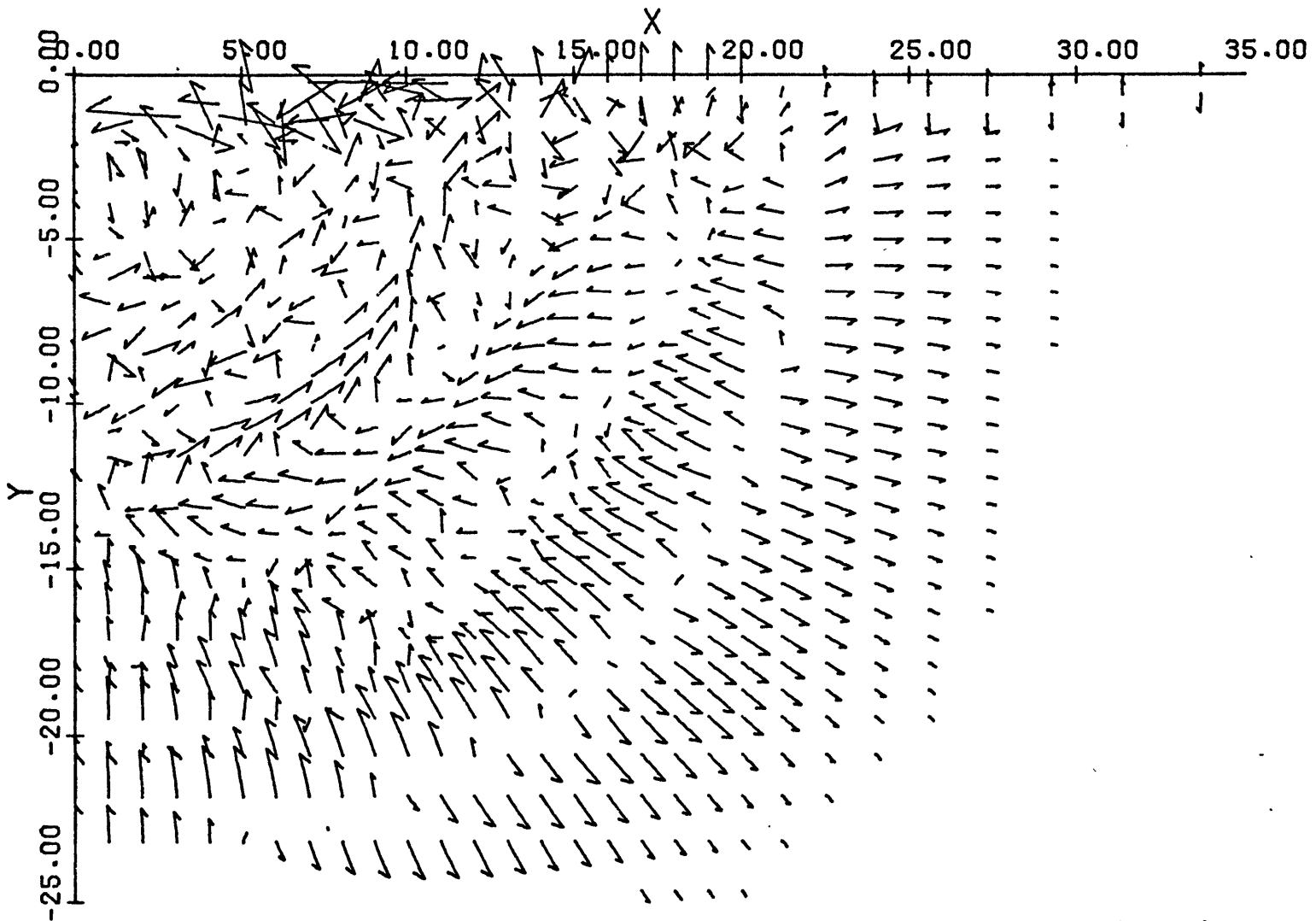


Figure 17. Acceleration vector plot for MC 2.12 at 3.0 msec after detonation. Acceleration is proportional to the square of the vector length with the distance between axis marks equal 100 KG's. Axes are in ft.

was, thus, described by the unloading models. The wave that produced the decrease in accelerations at the 20 ft radius was caused by a second increase in the overpressure model. The front of the rotational velocity wave, at 16 ft radius, was associated with accelerations which were parallel to the wave, indicating the wave was the principal shear wave. The velocity reversal on the vertical axis was, therefore, associated with the location of the principal shear wave. A series of calculated shear waves, produced by the "reflection" of the primary shear wave at the vertical axis, extended toward ground zero and controlled the sense of the horizontal velocities.

These wave relationships were also seen in the time histories, Figures 18 and 19, of the target point located on the vertical axis, where the geometric relations result in the simplest analysis of vertical motions. For the target point on the vertical axis and at an initial depth of 10 ft, the maximum stress occurred at 1.4 msec. The compressive wave was then followed by a pressure decrease that was interrupted, at 1.75 msec, by a combination of the second compressive wave and the reflection of the first wave from the material interface at 11.4 ft depth. The principal shear wave arrived at 2.3 msec, producing 1) a change in the maximum stress direction from vertical to horizontal; 2) a momentary period of a completely elastic stress state; and 3) a reversal of velocity from downward to upward. Behind the principal shear wave, the vertical stress was small while horizontal stresses were more gradually reduced until the material separated at 5.5 msec. At the time of separation the target point had an upward velocity of 12 ft/sec which would

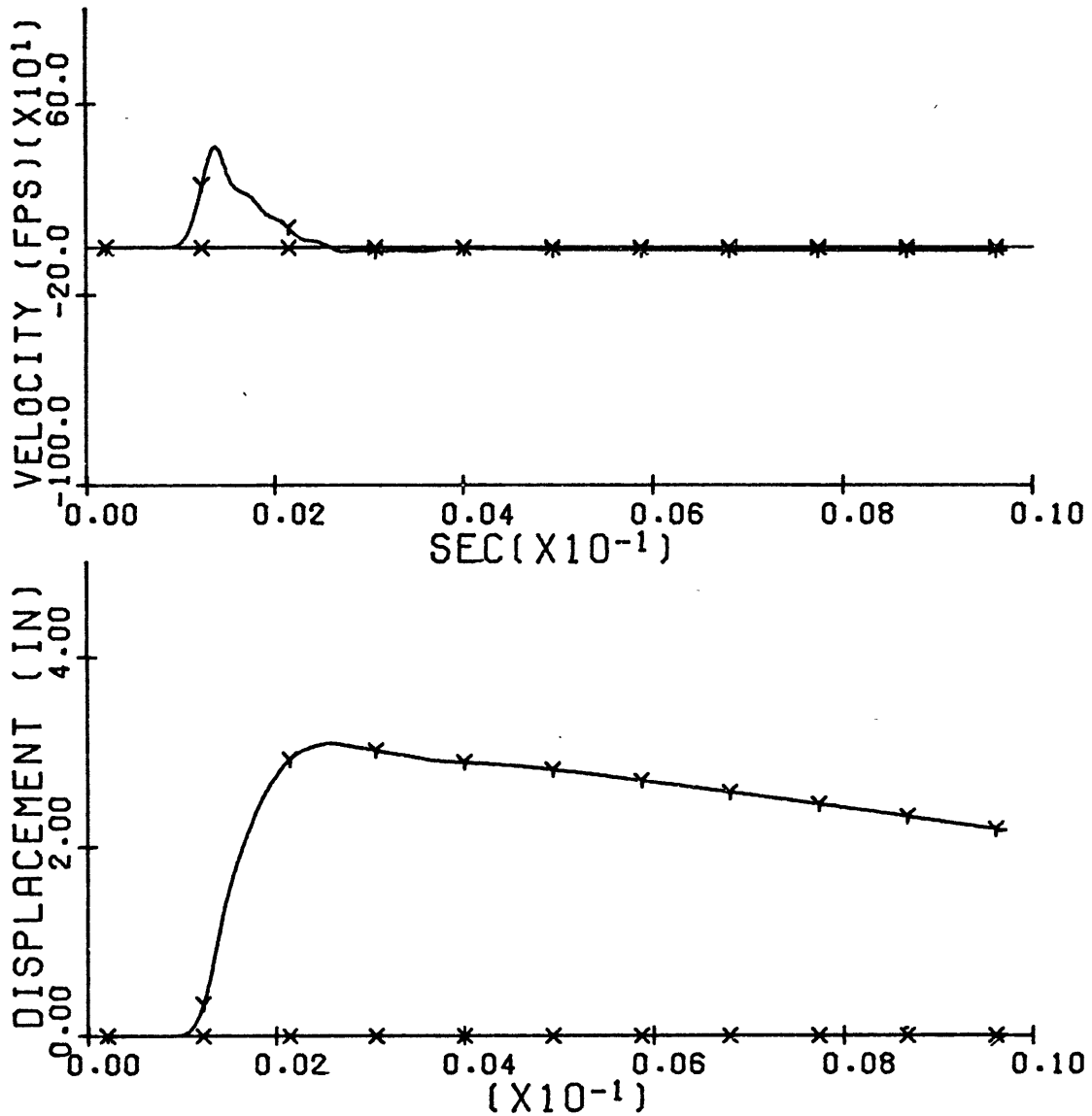
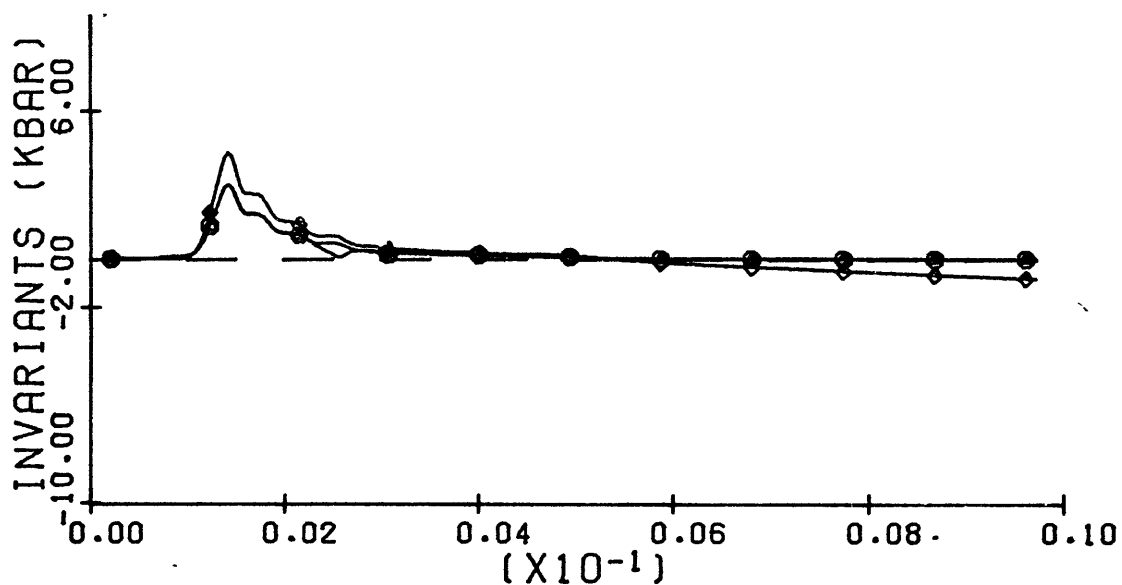
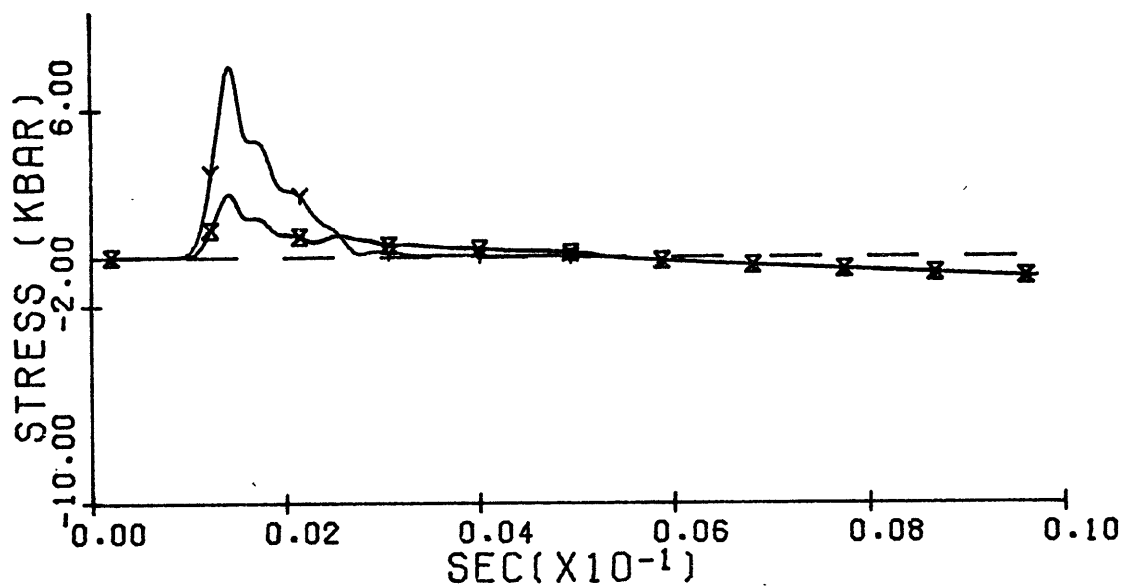


Figure 18. Motion time history for the target point originally located on the vertical axis at 10 ft depth in the MC 2.12 calculation. Positive Y values indicate downward motion.



Y - vertical

◇ - pressure

X - radial

△ - yield condition

Z - tangential

○ - second invariant

Figure 19. Stress time history for the target point of figure 18 with compressive stresses positive. Negative stresses indicate material separation.

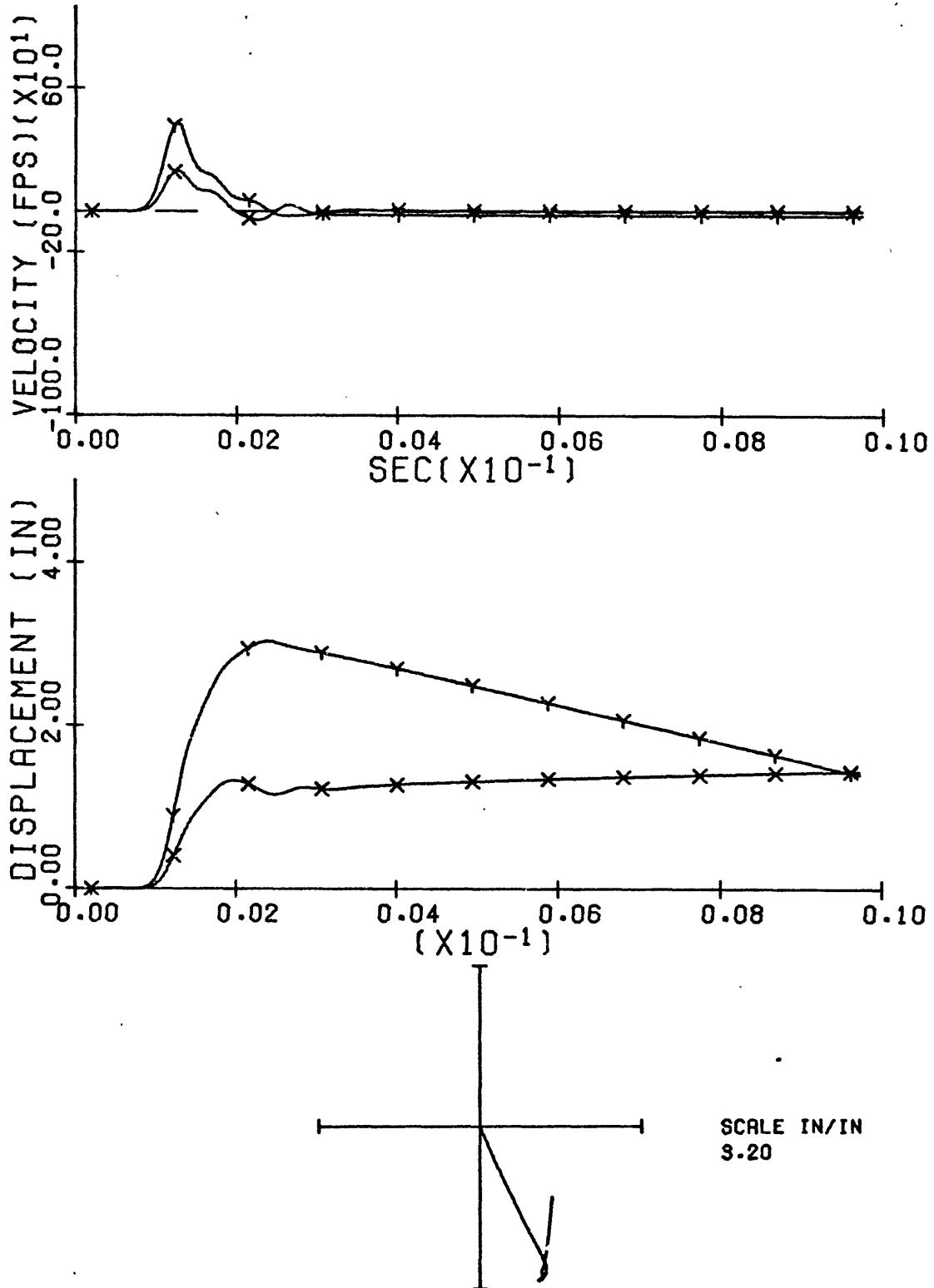
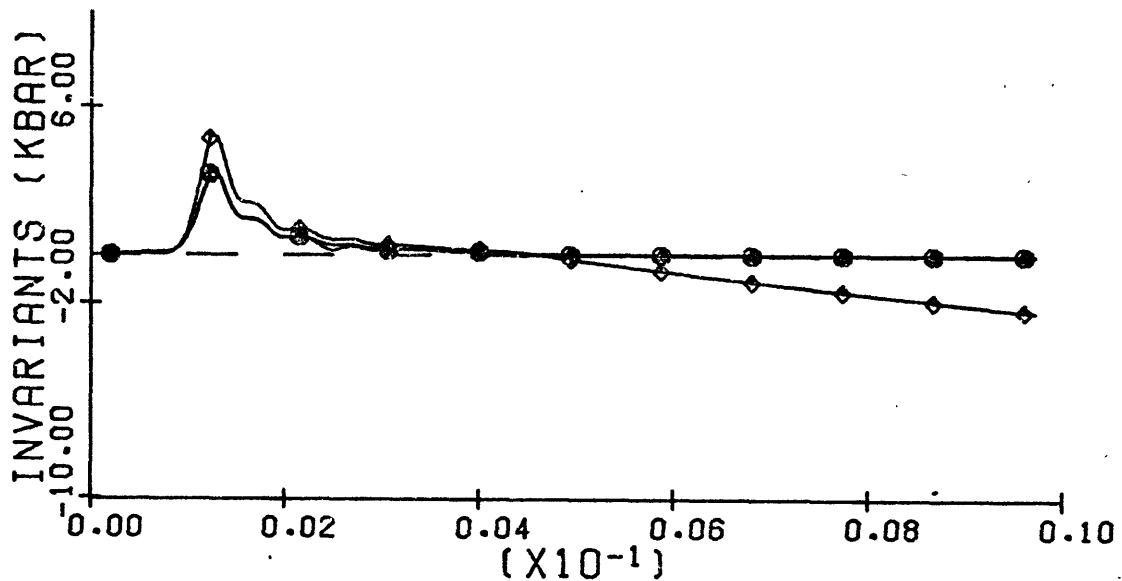
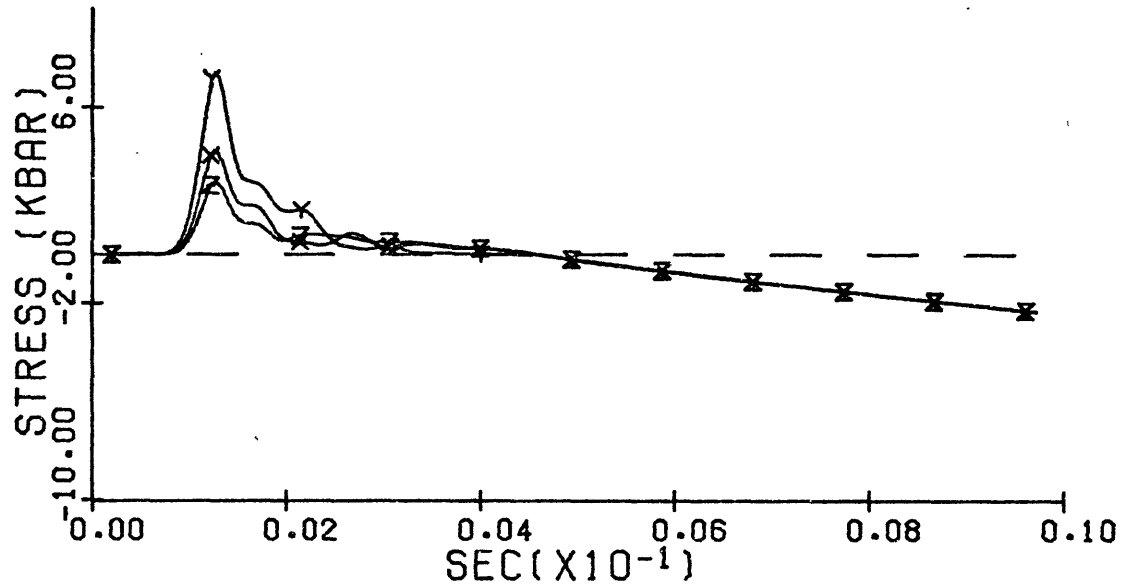


Figure 20. Motion time history of the target point originally located at 4 ft range and 8 ft depth in the MC 2.12 calculation. Positive Y values indicate downward motion; positive X values indicate outward motion. Target point path shown with downward motion down and outward motion to the right.



Y - vertical

◇ - pressure

X - radial

△ - yield condition

Z - tangential

○ - second invariant

Figure 21. Stress time history for the target point of figure 20 with compressive stresses positive. Negative stresses indicate material separation.

result in a maximum ballistic displacement of 2.2 ft.

The horizontal motions were examined in the time histories, Figures 20 and 21, of the target point initially located at a depth of 8 ft and a distance of 4 ft from the vertical axis. This point was first driven radially away from the origin by the compressional wave. The principal shear wave, which arrived near 2.2 msec, produced the inward velocity with a small enhancement of the downward velocity. The symmetry condition "reflected" the shear wave at the vertical axis, which resulted in a second shear arrival near 2.7 msec that produced upward and outward motion. Subsequent shear waves continued until the material separated, at 4.5 msec, after which the target point continued ballistically.

As noted before, a second region of primarily horizontal motion occurred in the calculation, centered near 18 ft range and 4 ft depth. Time histories in this region, Figures 22 and 23, showed an active period of 4 msec after which a condition of constant velocity was achieved. The constant-velocity condition was associated with no material density decrease, as shown by the stresses remaining near zero in contrast to the large negative stresses shown in the time histories below ground zero. Thus the materials were moving radially outward, and into a larger volume, in a velocity - range relation that resulted in a constant density. This region eventually formed the model true crater wall.

Two additional results of this simulation were of interest for shock-wave-cratering studies. First was a contour map,

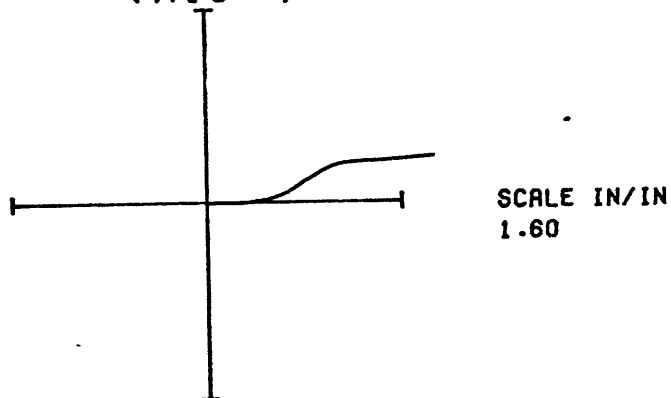
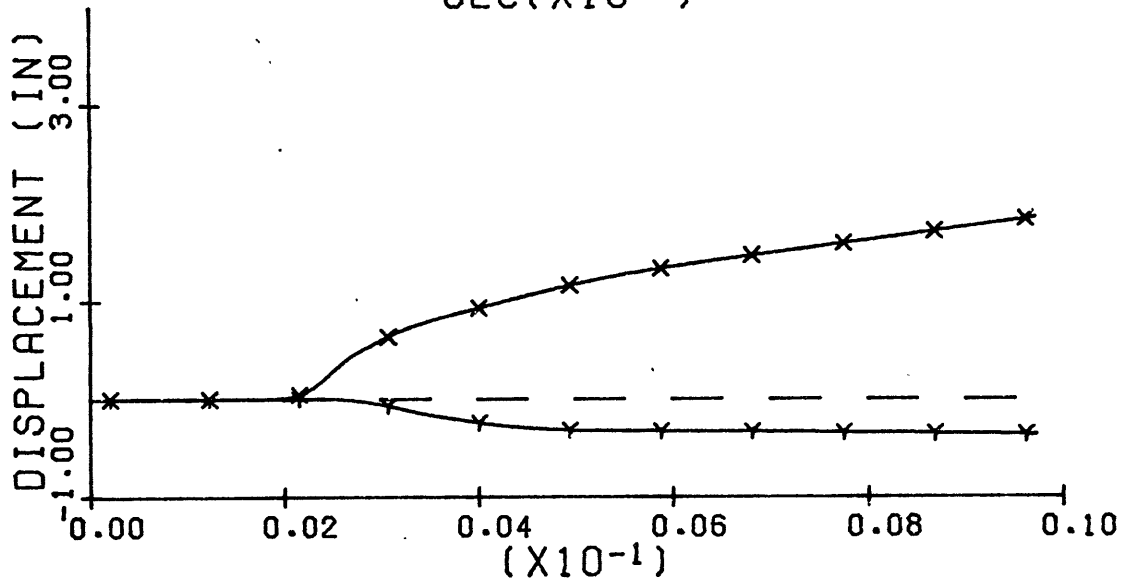
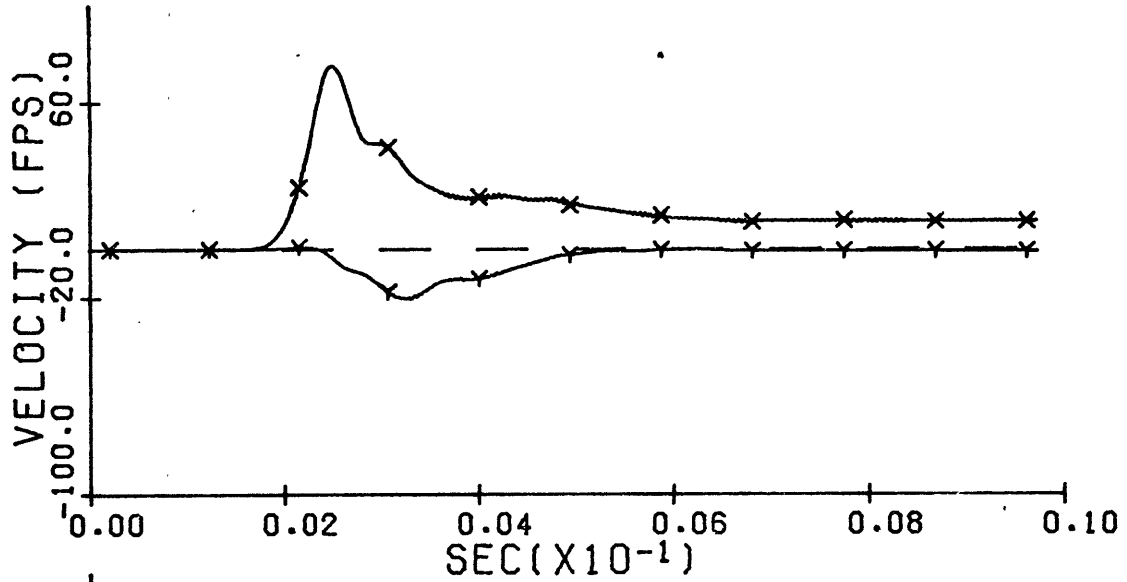
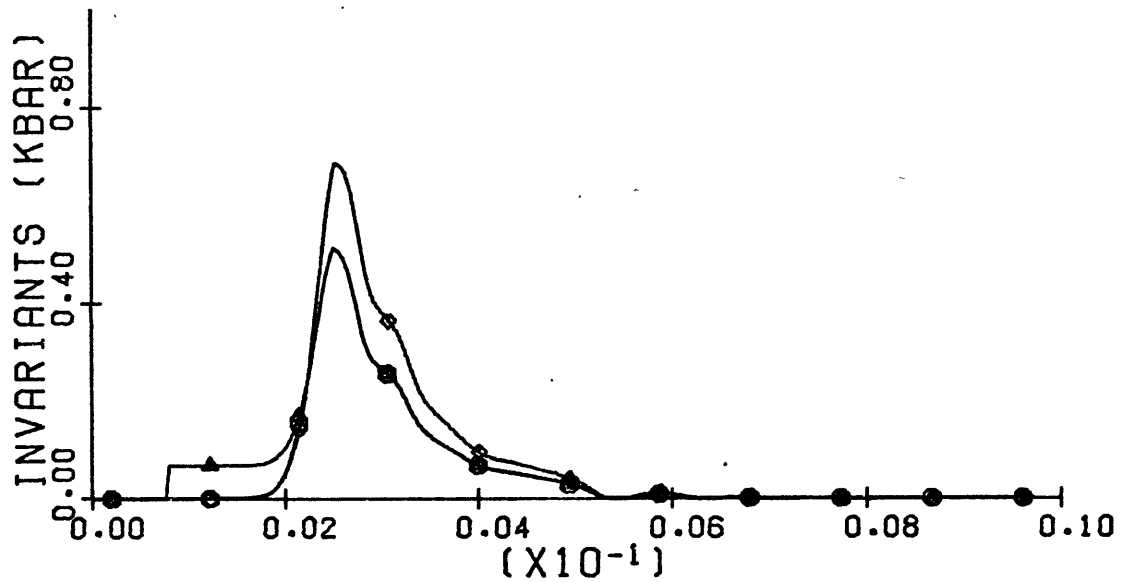
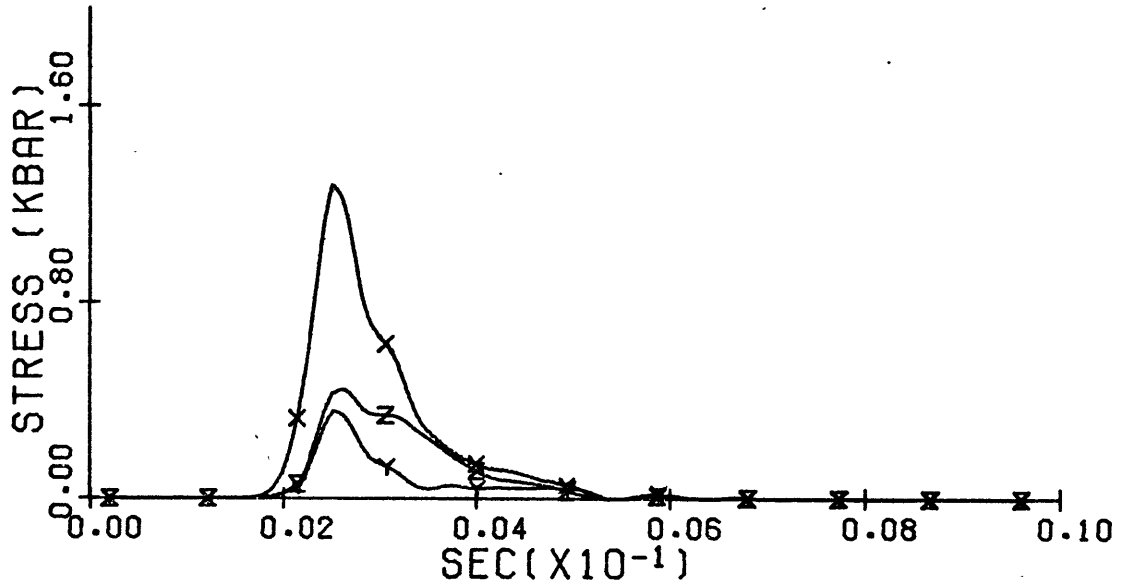


Figure 22. Motion time history of the target point originally located at 18 ft range and 4 ft depth in the MC 2.12 calculation. Positive Y values indicate downward motion; positive X values indicate outward motion. Target point path shown with downward motion down and outward motion to the right.



Y - vertical

◇ - pressure

X - radial

△ - yield condition

Z - tangential

○ - second invariant

Figure 23. Stress time history for the target point of figure 22 with compressive stresses positive.

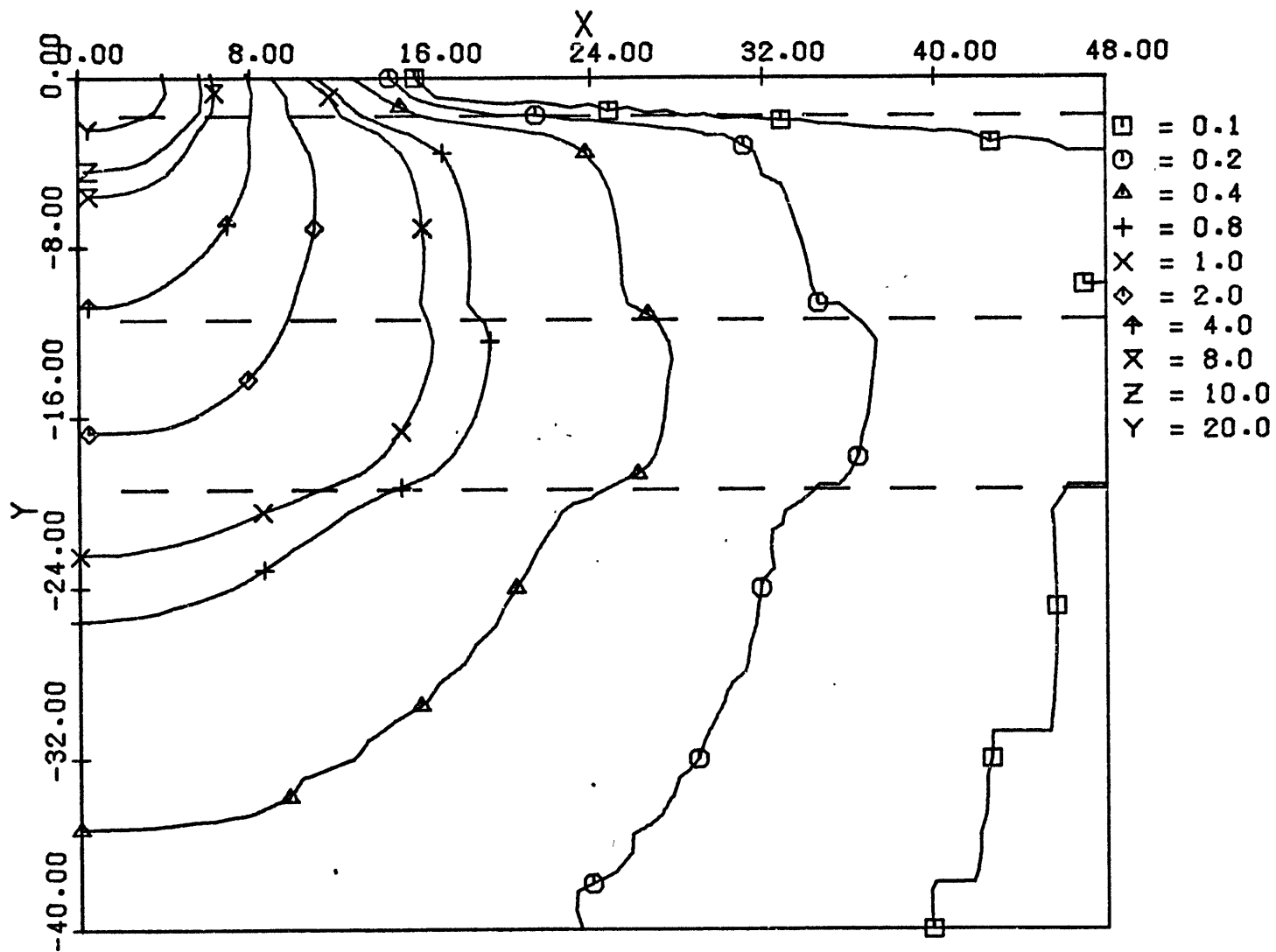


Figure 24. Maximum pressure contours as a function of original position for the MC 2.12 calculation. Dashed lines indicate layer interfaces. Peak pressures are in kbars; axes are in ft.

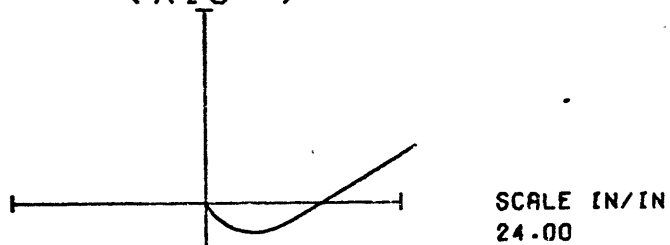
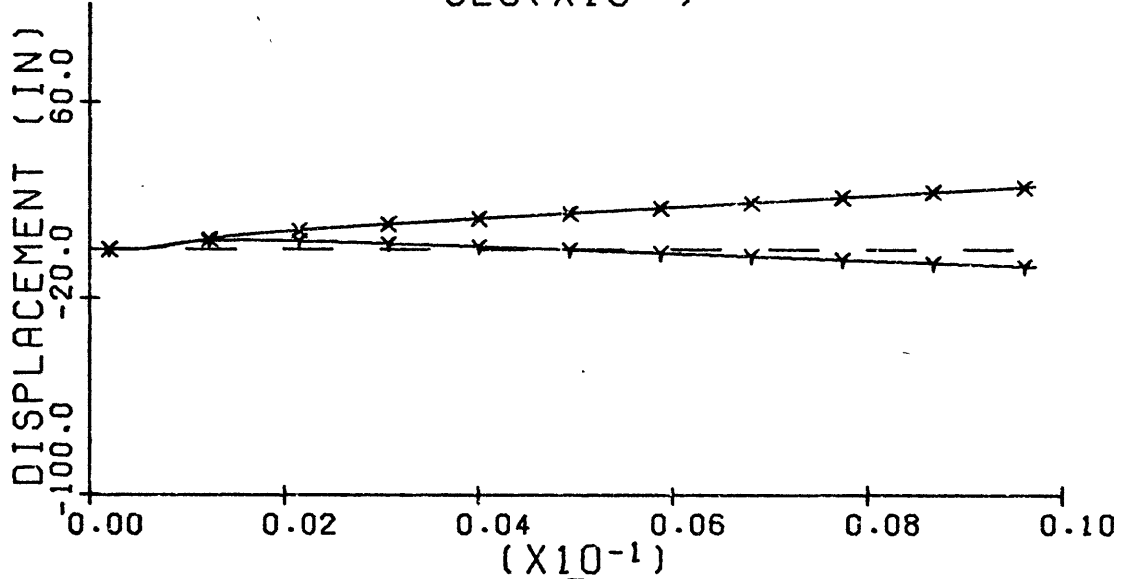
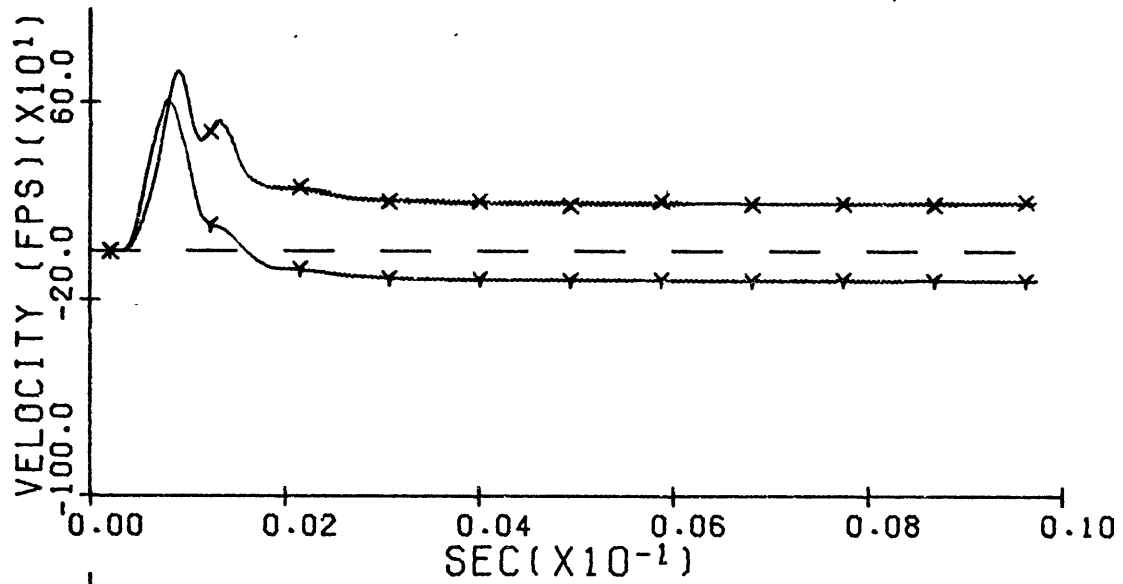


Figure 25. Motion time history of the target point originally located at 6 ft range and 1 ft depth in the MC 2.12 calculation. Positive Y values indicate downward motion; positive X values indicate outward motion. Target point path shown with downward motion down and outward motion to the right.

Figure 24, of peak pressures as a function of original position. This contour map indicated, by the absence of the 40 kbar contour, that the maximum pressure experienced anywhere in the calculational medium was less than 40 kbar. The transmission of high pressures in the medium below the 1.8 ft soil layer, and the absence of high pressures in the soil layer, indicated that only direct-induced signals were important in the lower medium. The increase of acoustic impedance in the layer between 11.4 and 19.2 ft depth also resulted in modification of the relation between maximum pressure and range. Second, the motion of the target point initially located at a range of 6 ft and a depth of 1 ft, Figure 25, simulated the path of material ejected to a long range. The particle path was similar to the motion of particles suggested by Gault et al. (1968) during the excavation stage of a crater formed by hypervelocity impact.

#### Numerical Parametric Study

The results of the Mixed Company II numerical simulation, MC 2.12, were applicable only to that experiment. Extension of those results to other occurrences of central mounds required information concerning the effects of material properties on central mound mechanics. This information was obtained through a parametric study of the influences of compactibility, layering, and material yielding models. In addition, as a first attempt to apply the study of central mounds to an examination of lunar evolution, the influence of a "fluid" material below a solid layer was examined. The results of the calculations in this parametric study indicated that 1) the calculation of upward

motions below the crater was dependent on the material compaction model, 2) the layering included in the Mixed Company II simulation only slightly influenced the upward velocities below the crater, 3) the bulking model included in the associated flow rule contributed significantly to the calculated upward motions, 4) upward velocities for grid points on the axis of symmetry were first calculated where strength effects were important, and 5) the presence of a lower, "fluid" layer modified the calculated response in an overlying, solid layer in a manner that may have eventually resulted in upward motions.

Compaction Model Effects. The results of the Distant Plain 6 and Nuclear Explosion numerical simulations had indicated that increased compaction of materials reduced the calculated upward velocities. The effects of changes in the compaction model on the MC 2.12 results were examined in two numerical experiments. In the first experiment, the values of the initial unloading sonic velocities,  $c_u$ , in the lower three layers were changed to

$$c_u = c_L + 3000$$

which increased the compactibility of the materials to 30%. In the second experiment, no compaction of the material in the lower three layers was allowed.

The calculation, MC 2.13, that included the increased compactibility resulted in a complete lack of upward motions below the crater. By 9.5 msec all vertical velocity components, Figure 26, below the crater region were either downward or had completely stopped. Further, there were no compressive stresses

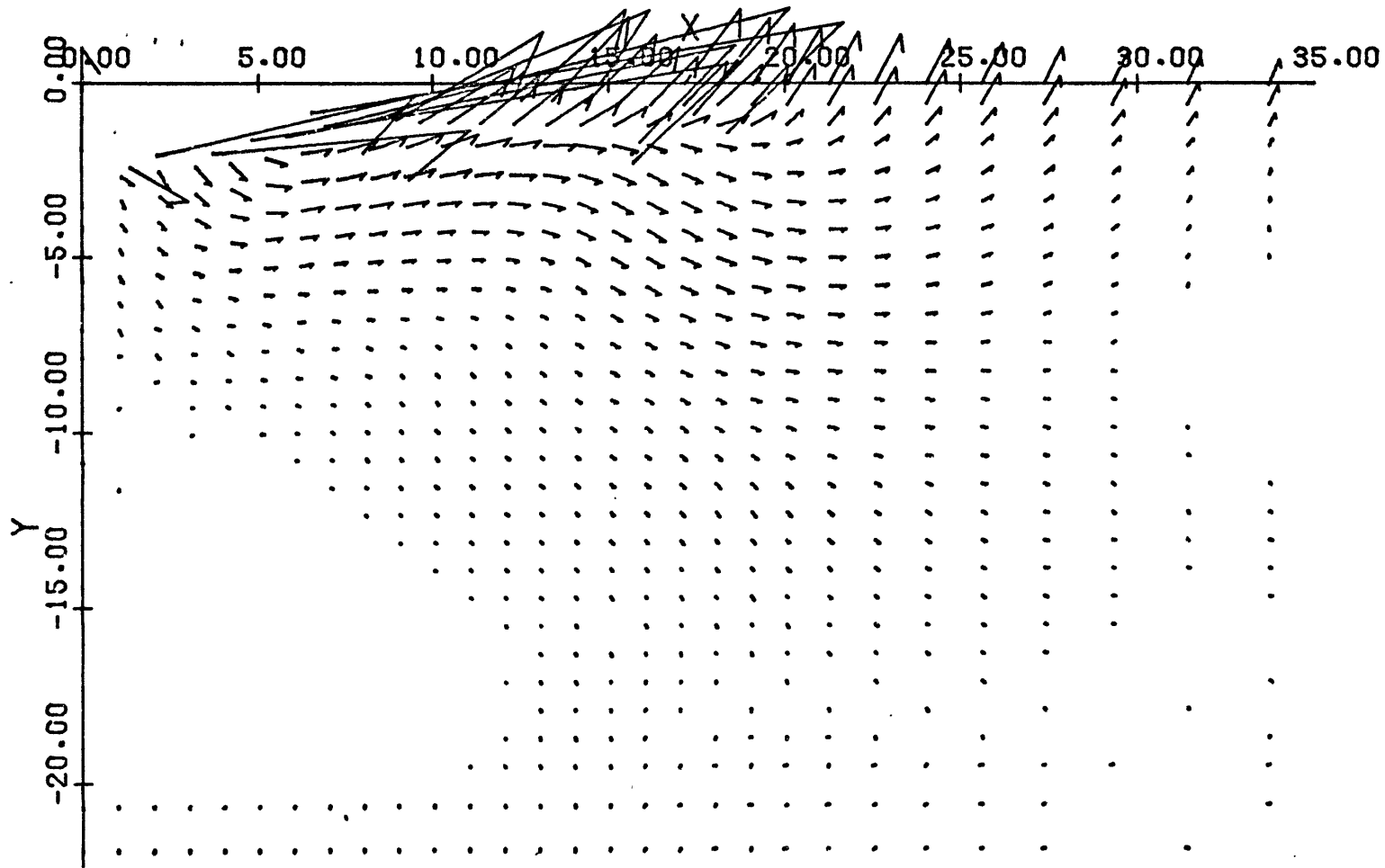


Figure 26. Velocity vector plot for MC 2.13 at 9.5 msec after detonation. Velocity is proportional to the vector length with the distance between axis marks equal 100 ft/sec. Axes are in ft.

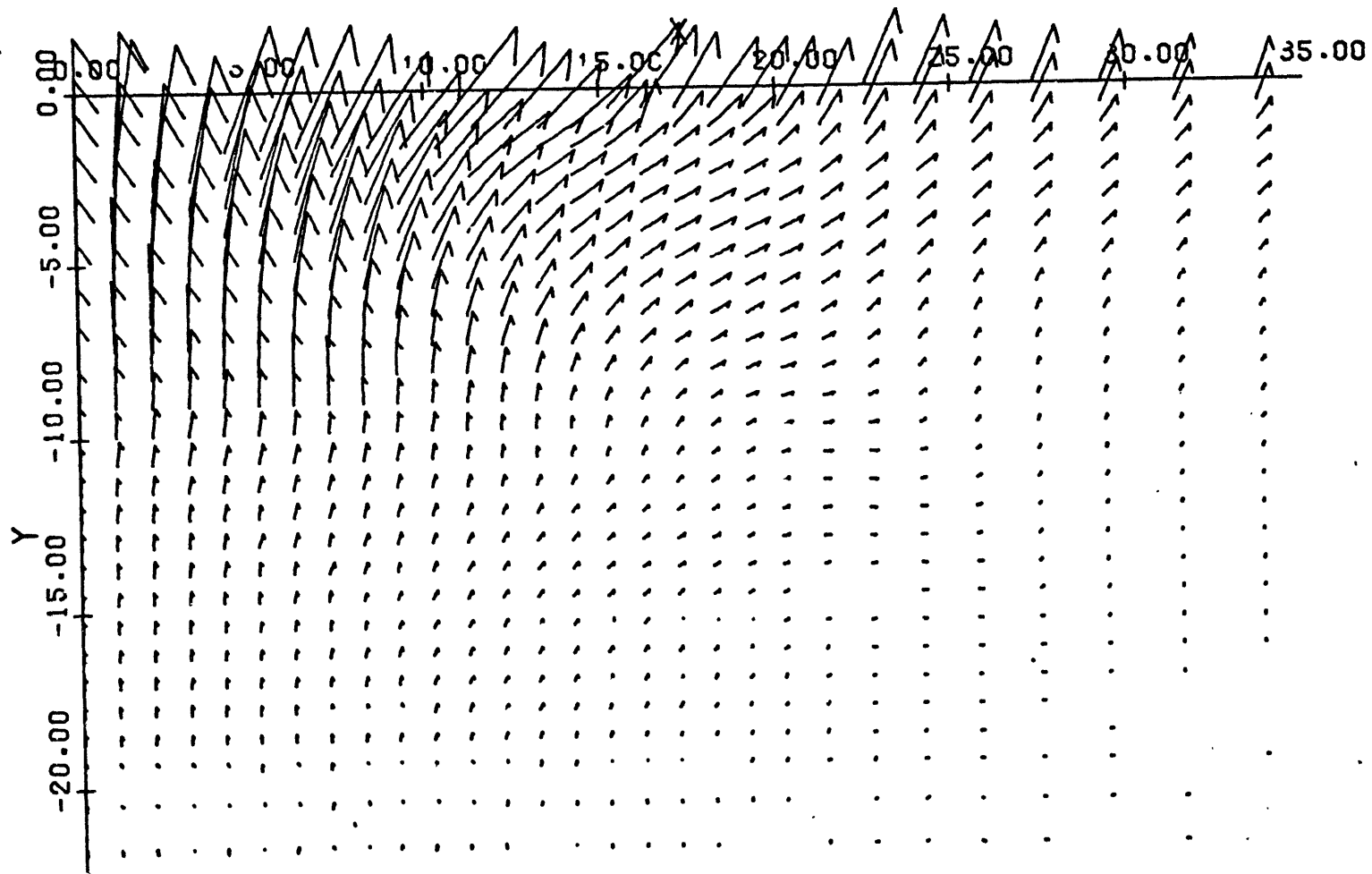


Figure 27. Velocity vector plot for MCP-03 at 8.2 msec after detonation. Velocity is proportional to the vector length with the distance between axis marks equal 100 ft/sec. Axes are in ft.

in the material below the crater to a depth of 35 ft to produce significant upward velocities after this time. A ballistic extrapolation of this velocity field would be expected to produce a crater of about 22 ft radius and a maximum depth below the original ground surface of 3 ft directly below ground zero with no central mound. These results occurred even though the calculated primary shear wave produced inward velocities, but not a change in maximum stress direction, as it propagated down the vertical axis.

The results of the calculation with incompactible lower layers, MCP-03, indicated motions qualitatively similar, Figure 27, to the MC 2.12 calculation, but with larger velocity magnitudes below the crater. The upward velocity, after material separation, for the target point on the vertical axis and initially 3 ft below the surface was 83 ft/sec, which was a factor of 2 greater than the velocity for the similar target point in the MC 2.12 calculation. However, because the magnitude of the upward velocity decreased more rapidly with depth in the MCP-03 results, the velocity of the target point at the 10 ft depth was only 16.3 ft/sec, or a factor of 1.35 greater than the equivalent value in the MC 2.12 calculation. That velocity would produce a ballistic displacement of only 4.1 ft upward. Also, because velocity conditions in the entire flow-field were increased, the model crater produced by a ballistic extension of this calculation would be expected to be less consistent with the observed crater than the MC 2.12 crater model. Therefore, a simple reduction in the model compactibility would not

provide an explanation of the discrepancy between the heights of the observed and calculated central mound.

A third numerical experiment, MCP-09, was accomplished because of the contrast in the results between the MC 2.12 calculation, with 10% compactibility, and the MC 2.13 calculation. The calculation MCP-09 was used to determine whether the upward velocities below the crater were dependent on the material compactibility or the entire unloading relation. In the MCP-09 calculation, the same values of  $c_u$  as MC 2.13 were used, but the compaction values were reduced to the MC 2.12 values.

The results of the calculation, MCP-09, indicated that the value of the final density after a cycle of loading and unloading was more important to central peak formation than an accurate description of the unloading path. The calculated flow field at 9.5 msec, Figure 28, was similar to the MC 2.12 calculation, with only small differences existing. The differences included a maximum 20% difference in the calculated vertical velocities along the axis of symmetry. In the MCP-09 calculation, the final velocities were all lower than the MC 2.12 results above 9 ft depth and higher below that depth, which would increase the height of the calculated central mound. Also, the horizontal velocities were generally lower and tended to be more inward in the MCP-09 calculation.

The similarity existed between the MC 2.12 and MCP-09 calculations despite a completely different early history of the two models. The flow field at 2.8 msec for MCP-09, Figure 29, was much different from the MC 2.12 flow field, Figure 16, at

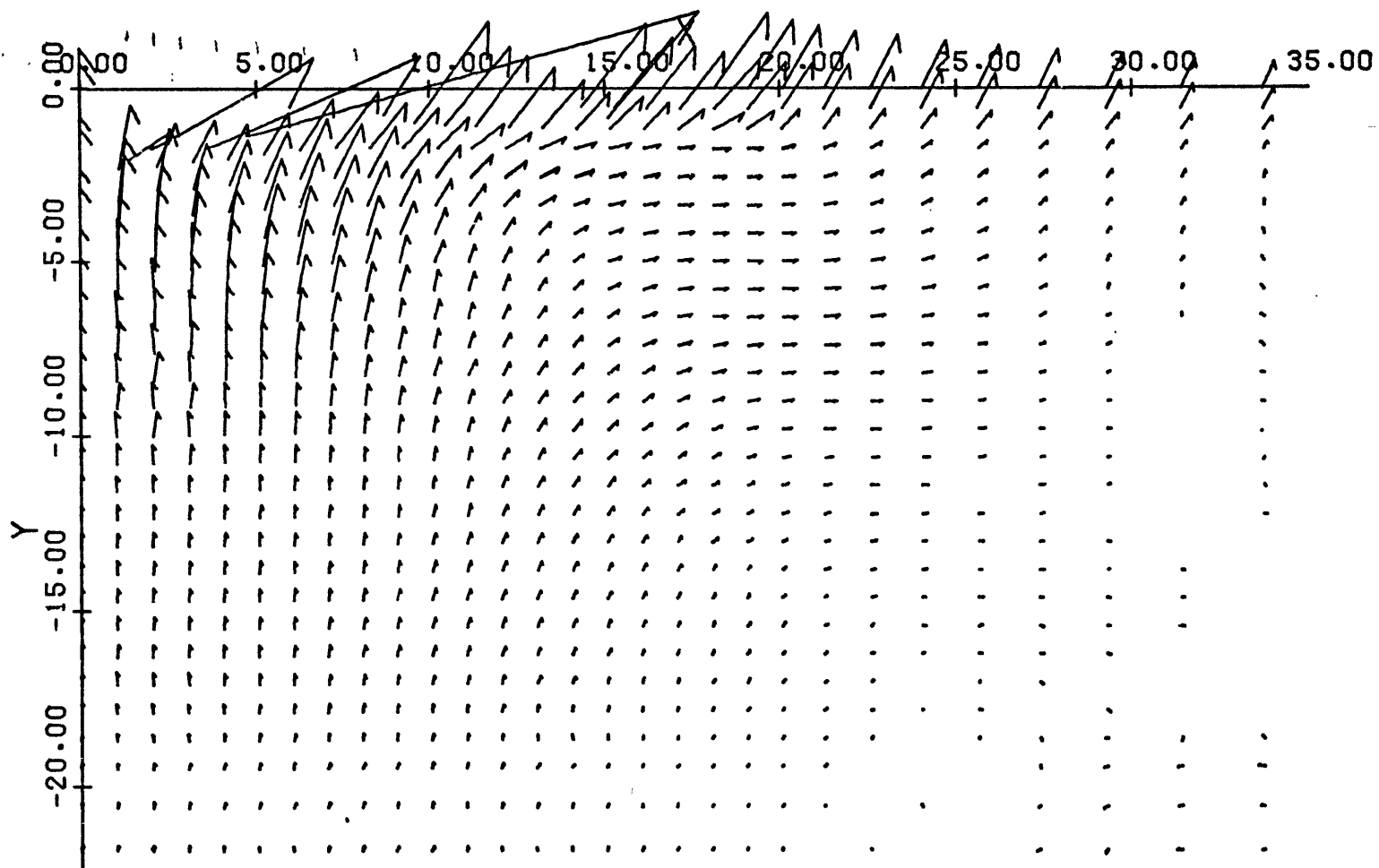


Figure 28. Velocity vector plot for MCP-09 at 9.5 msec after detonation. Velocity is proportional to the vector length with the distance between axis marks equal 100 ft/sec. Axes are in ft.

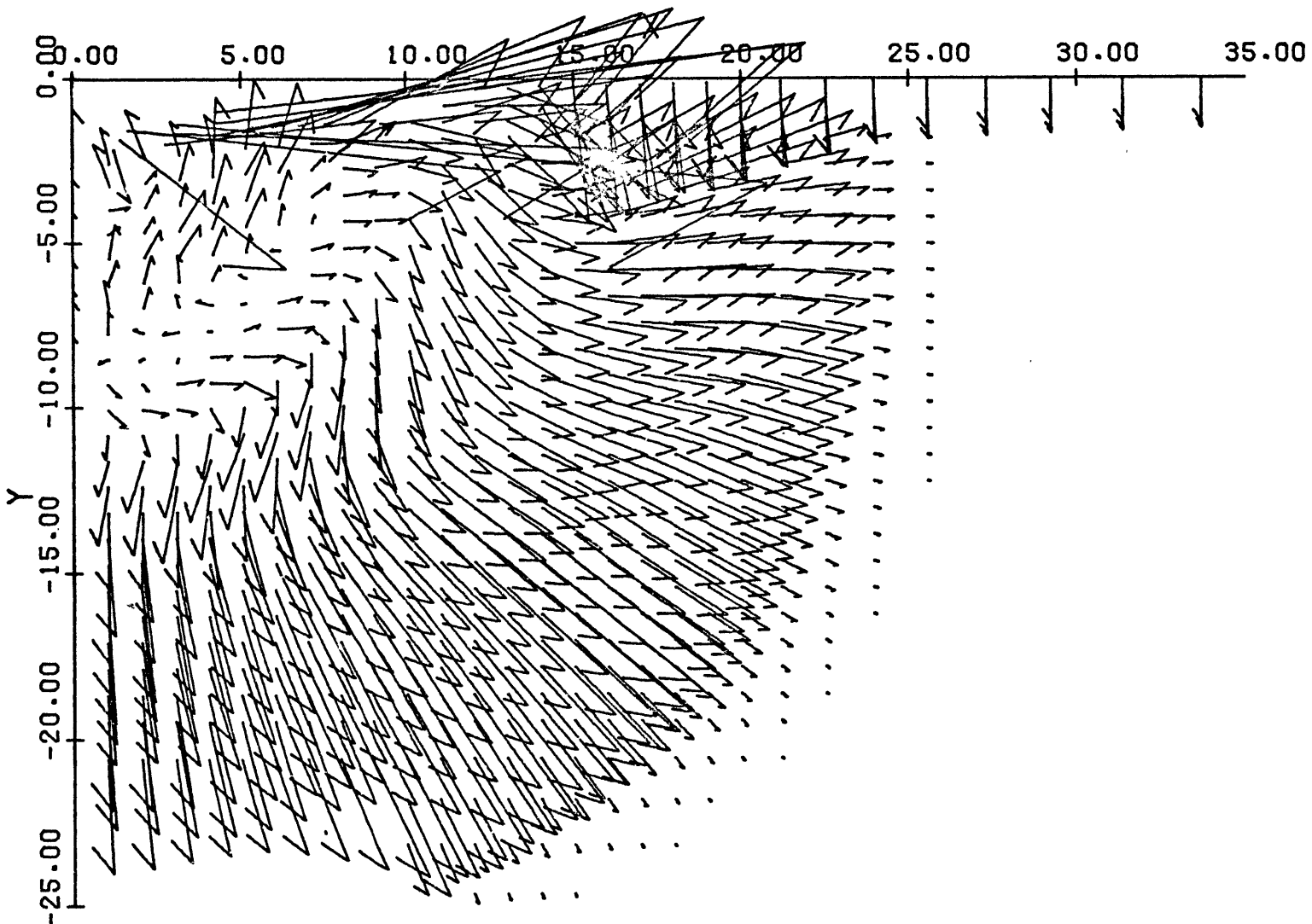


Figure 29. Velocity vector plot for MCP-09 at 2.8 msec after detonation. Velocity is proportional to the vector length with the distance between axis marks equal 100 ft/sec.. Axes are in ft.

3.0 msec. The primary shear wave produced lower inward velocities close to the axis as it passed. The maximum inward velocity in the MCP-09 calculation was 13 ft/sec at 11.6 ft depth, while in the MC 2.12 calculation it was 28 ft/sec at 12.3 ft depth. Also, upward velocities along the vertical axis did not occur below 9 ft depth, which was significantly shallower than the primary shear wave, or even its calculated reflection. Finally, in contrast to the MC 2.12 calculation, the maximum stress remained the vertical stress after the shear wave passed. All of these differences were caused by the different wave speeds of the two models.

Layering Effects. Three numerical calculations were used to determine the influence of the material layers that were modeled in the Mixed Company II simulation. Incompactible models for the lower three layers were used to simplify the analysis of the results and to emphasize the rebound effects. The first calculation, MCP-01, consisted of a homogeneous, incompactible halfspace with the properties of the second layer. In the second calculation, MCP-02, the soil layer of MC 2.12 was used over the MCP-01 halfspace. In the third experiment, MCP-03, the incompactible third-layer model was included from 11.4 ft to 19.2 ft depth, as previously described.

The influence of the soil layer was indicated by a comparison of velocity-vector plots, Figures 30 and 31, near 9 msec. These plots showed that near the vertical axis the flow field was similar. The flow was mostly upward, with velocities along the vertical axis 20% greater for MCP-02 than for MCP-01.

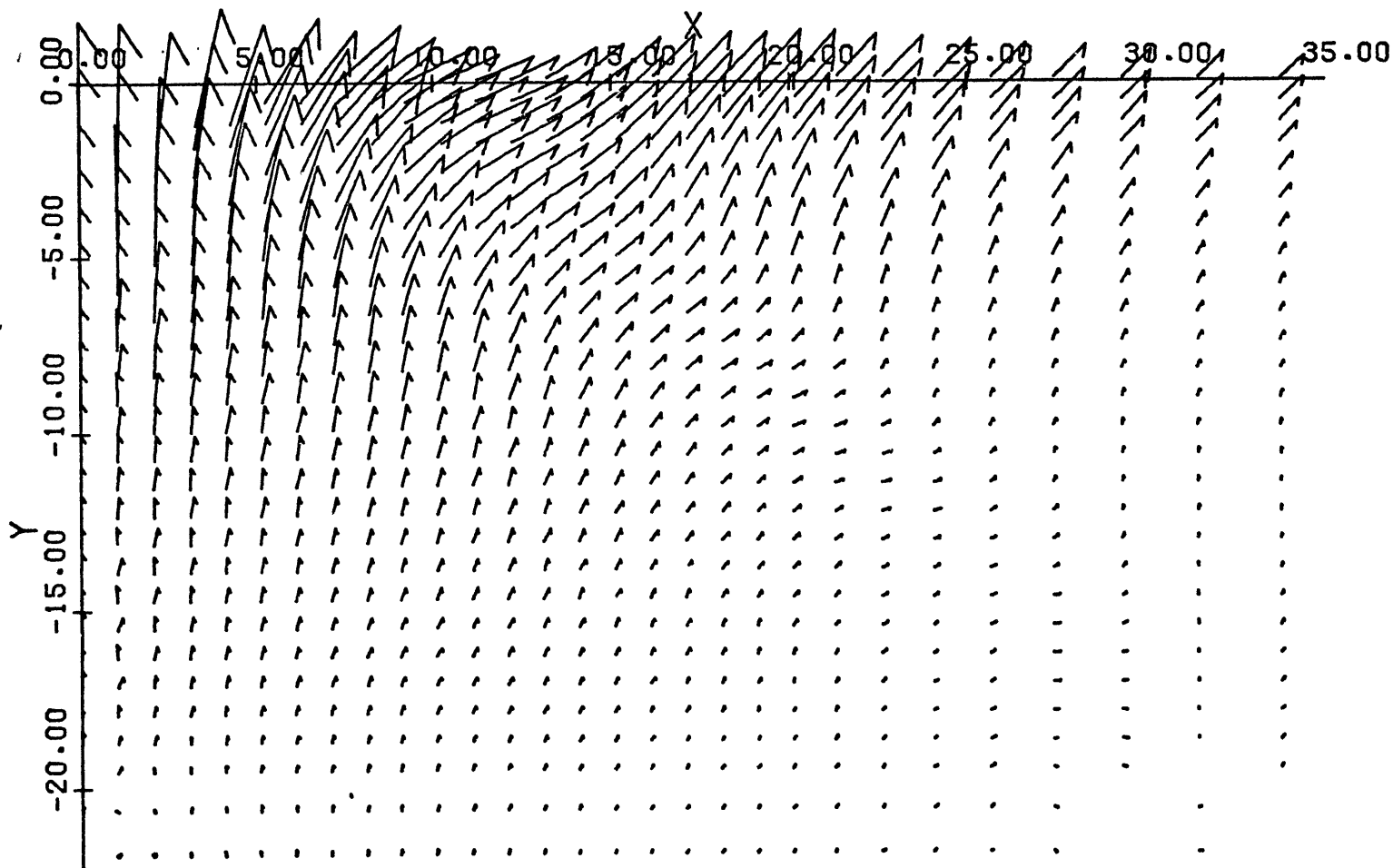


Figure 30. Velocity vector plot for MCP-01 at 8.4 msec after detonation. Velocity is proportional to the vector length with the distance between axis marks equal 100 ft/sec. Axes are in ft.

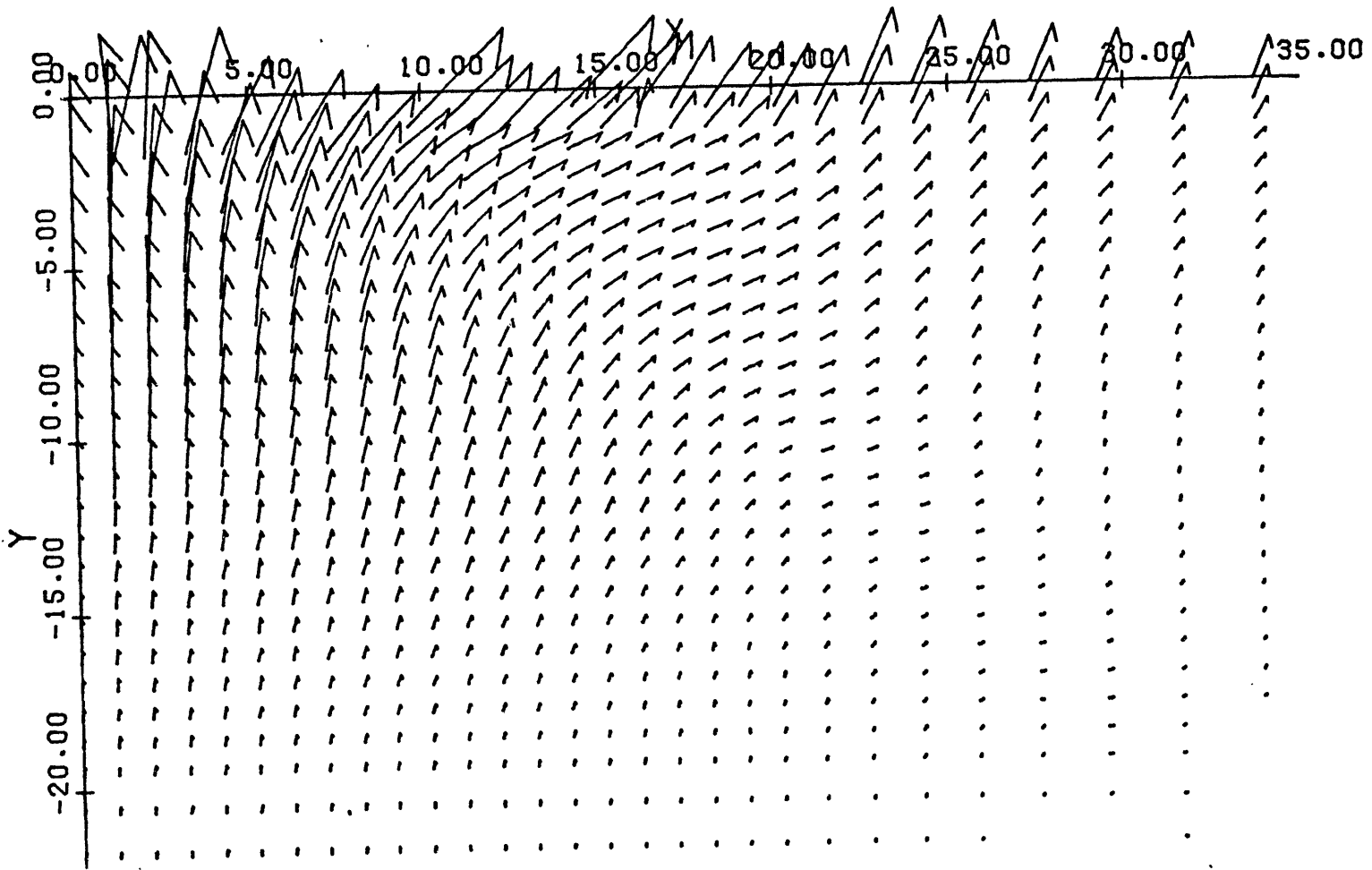


Figure 31. Velocity vector plot for MCP-02 at 9.5 msec after detonation. Velocity is proportional to the vector length with the distance between axis marks equal 100 ft/sec. Axes are in ft.

However, there was much greater upward motion of the region centered near 18 ft range and 4 ft depth in MCP-01 than in MCP-02. These results were caused by the hydrostat for the soil model. Since the maximum pressures in the soil near 18 ft were less than 100 bars (Figure 24), the soil responded as a soft material with lower density than the material below it. Therefore, the air overpressures were not effectively coupled at either the air-ground interface or the material interface at this range. Furthermore, the soil layer was 72% compactible, which reduced the subsequent upward motion of this layer. When the direct-induced wave arrived in the lower material, a larger amount of the upward momentum was transferred to the soil to produce upward motions in the soil. However, at the 20 kbar pressures in the material below ground zero, both the soil and the lower material had similar densities and bulk moduli, which resulted in effective stress-wave transmission in this region. The result was that the soil layer only slightly affected the strong direct-induced signal in the lower material, but reduced significantly the effects of the air shock away from ground zero.

Comparisons between the MCP-02 and MCP-03 calculations showed that the increased acoustic impedance of the third layer only slightly influenced the upward motions that contributed to the calculated central uplift. The final upward velocities for target points on the vertical axis and initially located from 3 to 6 ft depth were 18 ft/sec higher for MCP-03 than for MCP-02. However, those target points were located in material which was calculated to be ejected from the crater. At deeper

target points, the relationship between velocities changed until the final upward velocity of the target point at 10 ft depth in MCP-02 was 19 ft/sec, or almost 3 ft/sec higher than the value computed in MCP-03. The final velocities for lower target points on the vertical axis were also nearly equivalent in the MCP-02 and MCP-03 calculations.

In the calculations that included the third layer, the modeled von Mises yield strength controlled the yield condition during maximum stress conditions to a range of 6 ft above 16 ft depth in that layer. Although an additional calculation indicated that this control was not important to the calculated motions because of the limited region involved, the change of yield mode showed that the calculated response would be modified by increased stress-conditions.

Yield Model Effects. The yield model in the MC 2.12 calculation included a model of material strength that contained an assumed method of shifting the yield surface once the yield condition was met. This method had not been included in earlier numerical simulations of shock-wave-cratering events. Therefore, the requirement for the shift and alternate ways of accomplishing the shift were examined in three numerical experiments.

The requirement for the shift of the yield surface was tested by a calculation, MC 2.15, to examine if a complete absence of tensile strength would also produce the observed crater without shifting the yield surface. The same model as MC 2.12 was used in the MC 2.15 calculation except the parameter S was never changed from zero and the material was assumed to

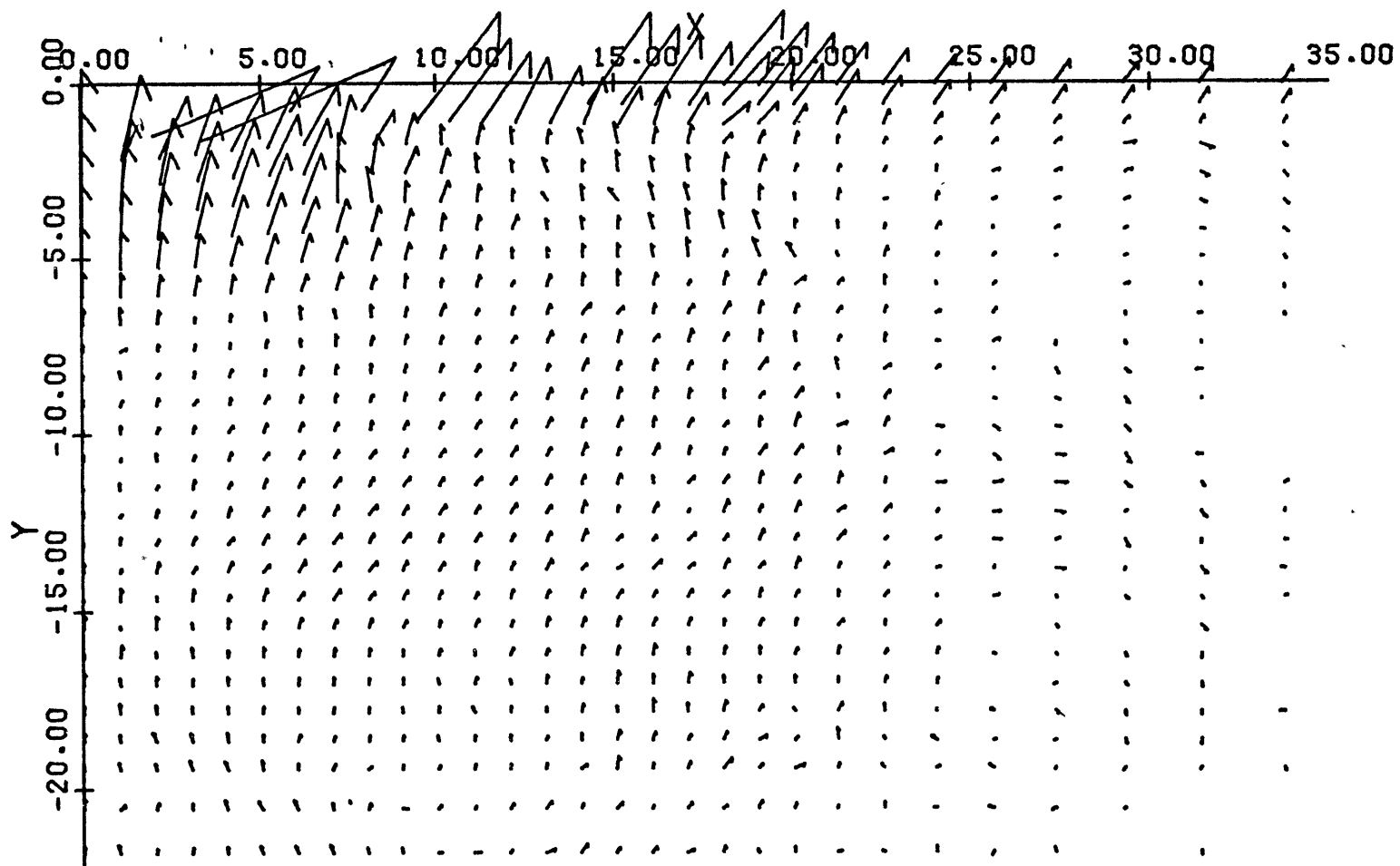


Figure 32. Velocity vector plot for MC 2.15 at 8.4 msec after detonation. Velocity is proportional to the vector length with the distance between axis marks equal 100 ft/sec. Axes are in ft.

separate whenever negative pressures occurred. This model resulted in a completely different flow field that was not consistent with the observed crater. The plot of velocity vectors at 8.4 msec, Figure 32, showed that, in the second layer, only the material to a range of 8 ft and a depth of 6 ft had large upward velocities. All the upward velocities below that depth were less than 10 ft/sec. Since there were no calculated stress conditions remaining at that time which would produce a change in this flow field, the MC 2.15 model was considered to be inadequate. This result indicated that a material model with no cohesion was required to simulate the formation of the central mound in the Mixed Company II event.

Alternate methods of accomplishing the shift of the yield surface were tested in two numerical experiments. The MCP-02 calculation (the two layer model of soil on an incompactible halfspace) was used as the standard model for these numerical experiments. In one calculation, the parameter S was incremented by 0.04 only during each of the first 25 calculational cycles that the yield condition was satisfied. In the second calculation, the parameter S was incremented by 0.04 only after the calculation of the yield condition was complete, which affected the yield surface only during subsequent calculational cycles. The calculated conditions during both of these numerical experiments showed little variation from the MCP-02 values.

The inclusion of a yield model in the computer code was a theoretical complication required because materials have finite strengths. In order to demonstrate the effects of the yield

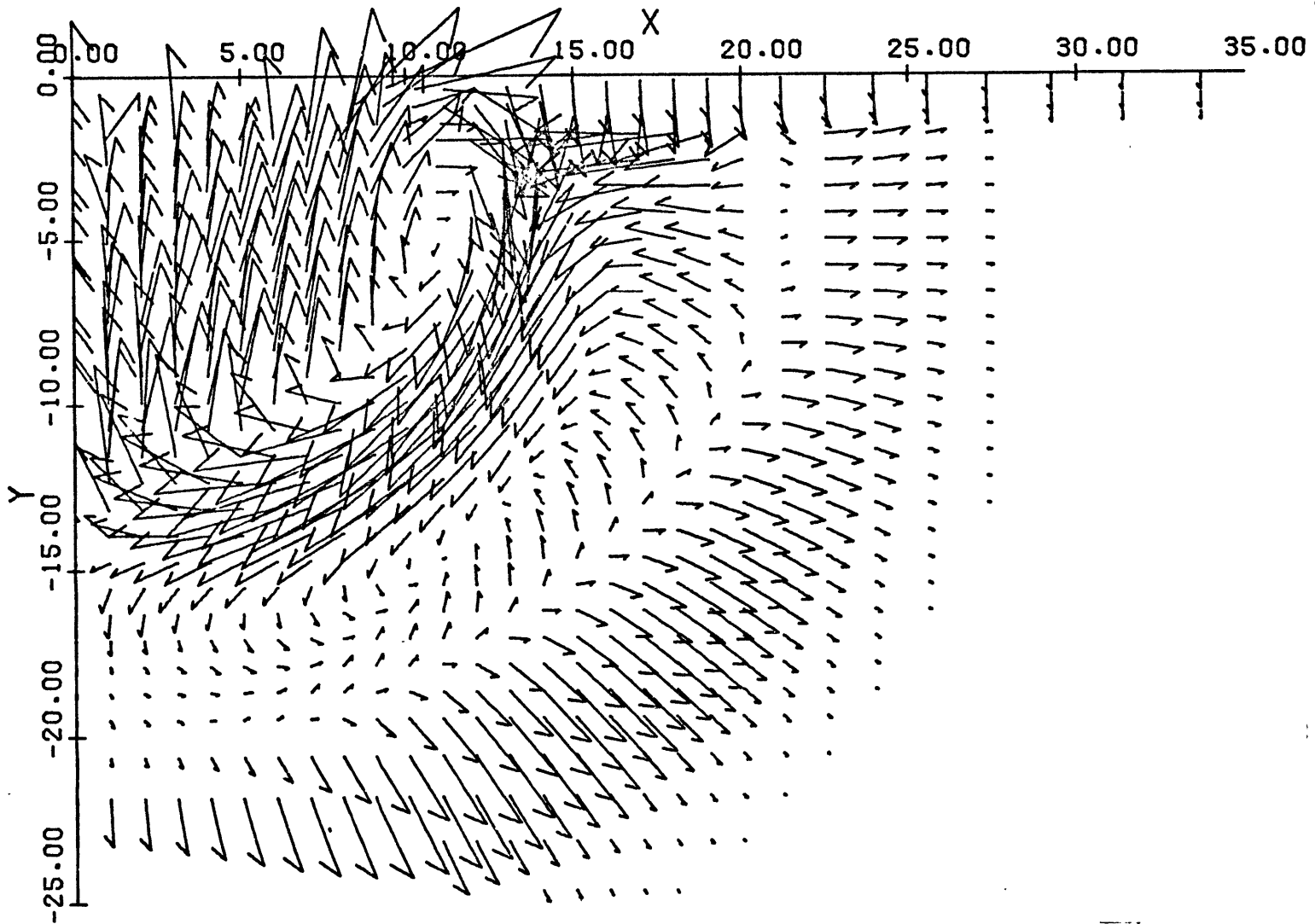


Figure 33. Velocity vector plot for MCP-06 at 3.2 msec after detonation. Velocity is proportional to the vector length with the distance between axis marks equal 200 ft/sec. Axes are in ft.

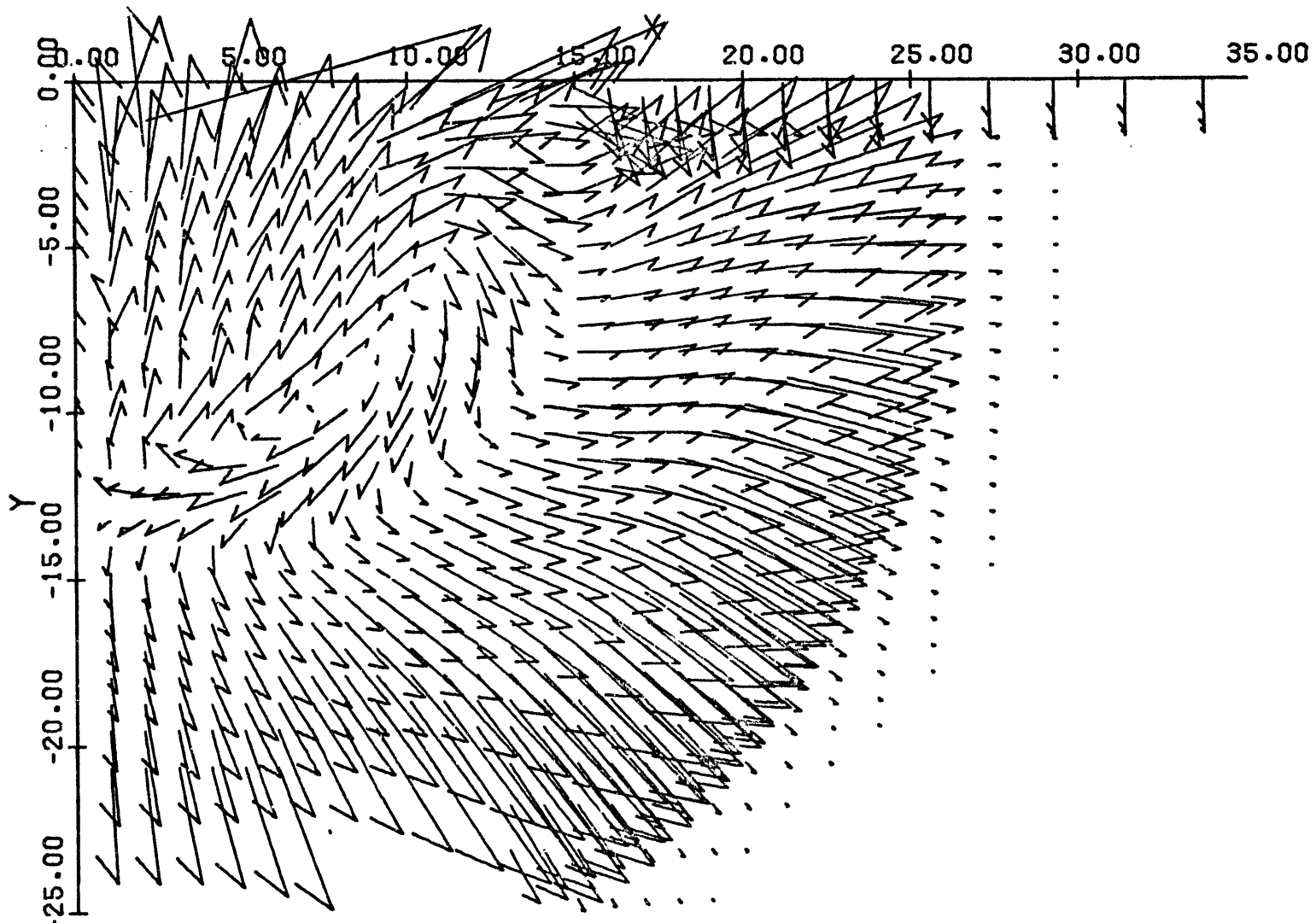


Figure 34. Velocity vector plot for MCP-02 at 3.2 msec after detonation. Velocity is proportional to the vector length with the distance between axis marks equal 100 ft/sec. Axes are in ft.

model on the calculated results, a no-yield assumption was used in one calculation. The MCP-02 model was used as a standard for this calculation (designated MCP-06), but the yield condition in the halfspace below the soil was completely ignored.

A comparison of velocity-vector plots at 3.2 msec, Figures 33 and 34 (note change in velocity scale), showed that the yield model reduced the velocities experienced during the unloading from maximum stresses. In the no-yield model, the maximum downward velocity and maximum normal stress of the compressional wave near the vertical axis were nearly equal to the analogous values when the yield model was included. However, in the no-yield case these values were immediately reduced after maximum compression, so that the downward velocity was only 5 ft/sec by 20 ft depth. The change in velocity direction, that occurred at a 21 ft radius from the origin, was associated with a change from positive to negative pressures, which did not occur in the MCP-02 calculation. Significant inward velocities, as high as 127 ft/sec at 2.6 ft depth and 17 ft range, occurred before the arrival of the shear wave caused clockwise rotation. The shear wave produced downward velocities as high as 135 ft/sec near the surface with inward velocities as high as 150 ft/sec at the 12.3 ft depth and 7 ft range. These values were five times as large as velocities produced by the calculated shear wave in the MCP-02 model. Behind the shear wave, the upward velocity on the vertical axis reached 147 ft/sec at 12.3 ft depth and remained near 100 ft/sec to 1.8 ft depth.

The yield model in the Mixed Company II numerical simulation

included the associated flow rule, the use of which in numerical ground-motion simulations is a recent development. As late as 1971, the Prandtl-Reuss flow rule was used to describe plastic stress-strain relations in numerical ground-motion simulations (Zelasko and Baladi, 1971; Trullio et al., 1969). As noted before, the only difference between the two flow rules, if the yield surface is independent of the third invariant of the deviator stresses, is the bulking included in the associated flow rule when the yield surface is a function of pressure. The effect of the associated flow rule was examined in a numerical experiment, MCP-05, in which the Prandtl-Reuss flow rule was used with the MCP-02 model.

The MCP-05 calculation resulted in a completely different response of the medium to the applied boundary conditions. Calculated motion remained predominantly downward and away from the axis of symmetry until 10 msec with no rotational motion, which was an outstanding feature of the MCP-02 calculation at 3.2 msec. At 10 msec, inward velocities as high as 2 ft/sec were calculated to a depth of 26 ft and range of 33 ft; however, vertical motion was still downward at velocities less than 10 ft/sec within a range of 15 ft. By the simulated time of 11.4 msec, the downward motion near the vertical axis had stopped and upward velocities as high as 10 ft/sec were calculated near the vertical axis to a depth of 20 ft. Also, at this time, the motion below 9 ft depth was inward with velocities less than 2 ft/sec, and material separation had occurred along the axis to a depth of 4 ft. The material-separation front proceeded downward and

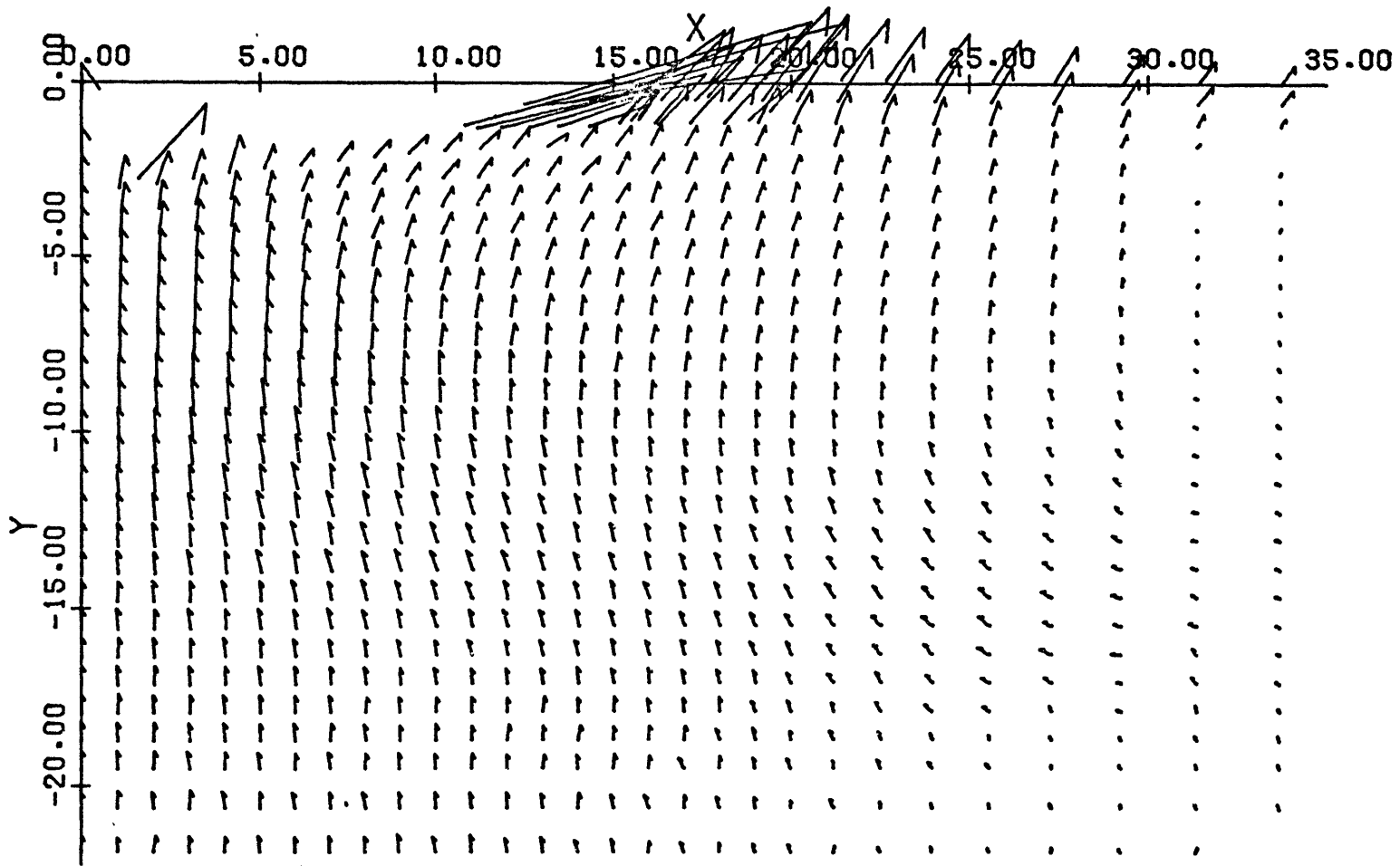


Figure 35. Velocity vector plot for MCP-05 at 19.9 msec after detonation. Velocity is proportional to the vector length with the distance between axis marks equal 50 ft/sec. Axes are in ft.

outward, at a speed of 3000 ft/sec, until by 19.9 msec the flow pattern shown in Figure 35 had developed with stresses within a 23 ft radius from the origin calculated to be near zero. During the entire calculation, upward velocities never exceeded 15 ft/sec in the halfspace below the model soil layer.

In the Mixed Company II numerical simulation and all subsequently described calculations, the yield condition for the material below the soil layer was usually determined from the Mohr-Coulomb relation as a result of the high von Mises limits. Therefore, the effect, on the MCP-02 calculation, of lowering the von Mises limit was tested. For this test, designated MCP-21, the von Mises limit in the material below 1.8 ft depth was set at 0.21 kbar; and, because calculated displacements were too large to allow calculation with a completely Lagrangian coordinate system, the generalized coordinate capability of the AFTON-2A code (Trulio, 1966) was used for grid points initially at and above 10.6 ft depth. The grid points in that region had fixed radial coordinates but were allowed to move vertically to retain proper stratigraphic relations. The properties of the mass that was transported across calculational faces were determined from the values in the zone out of which the material was being transported, and were "backward" transport terms (Trulio, 1964; Cooper, 1971). The coordinate system remained Lagrangian below 10.6 ft depth.

The time and location of the first upward motion on the vertical axis were accurately determined in this calculation. Near the vertical axis, upward velocities were first calculated

between 5.6 msec (Figure 36) and 6.9 msec (Figure 37) with downward motion near the axis still calculated below 18 ft and above 7 ft depth. The velocity transition region, near 16 ft depth and 5 ft range, was not associated with exceptional stress or acceleration conditions and only represented the null region of a continuous decrease in outward velocities. Continuation of the calculation to 10.5 msec, Figure 38, showed that velocities with inward components as large as 2.5 ft/sec and upward components as large as 20 ft/sec were calculated below 10 ft depth. The first upward motion on the vertical axis occurred near 12 ft depth at a simulated time of 6.3 msec.

The motion and stress histories, Figures 39 and 40, of that target point were, therefore, especially pertinent to an examination of the mechanics of central mound formation. The first signal was an elastic precursor that arrived at 1.4 msec and caused the stress conditions to reach the yield surface. The plastic wave then arrived at 1.9 msec, when the maximum compression and downward velocity were reached. In this plastic wave, the stress deviators were controlled by the von Mises yield condition and, therefore, the associated flow rule became equivalent to the Prandtl-Reuss flow rule. Also there was a significant difference between the maximum and minimum normal-stress values. After the maximum stresses occurred, the stresses were rapidly reduced, under elastic conditions, interrupted only by the second compressional signal. A lower stress state was then reached and maintained for a period of 3 msec, during which the yield surface again controlled the deviator stresses. This

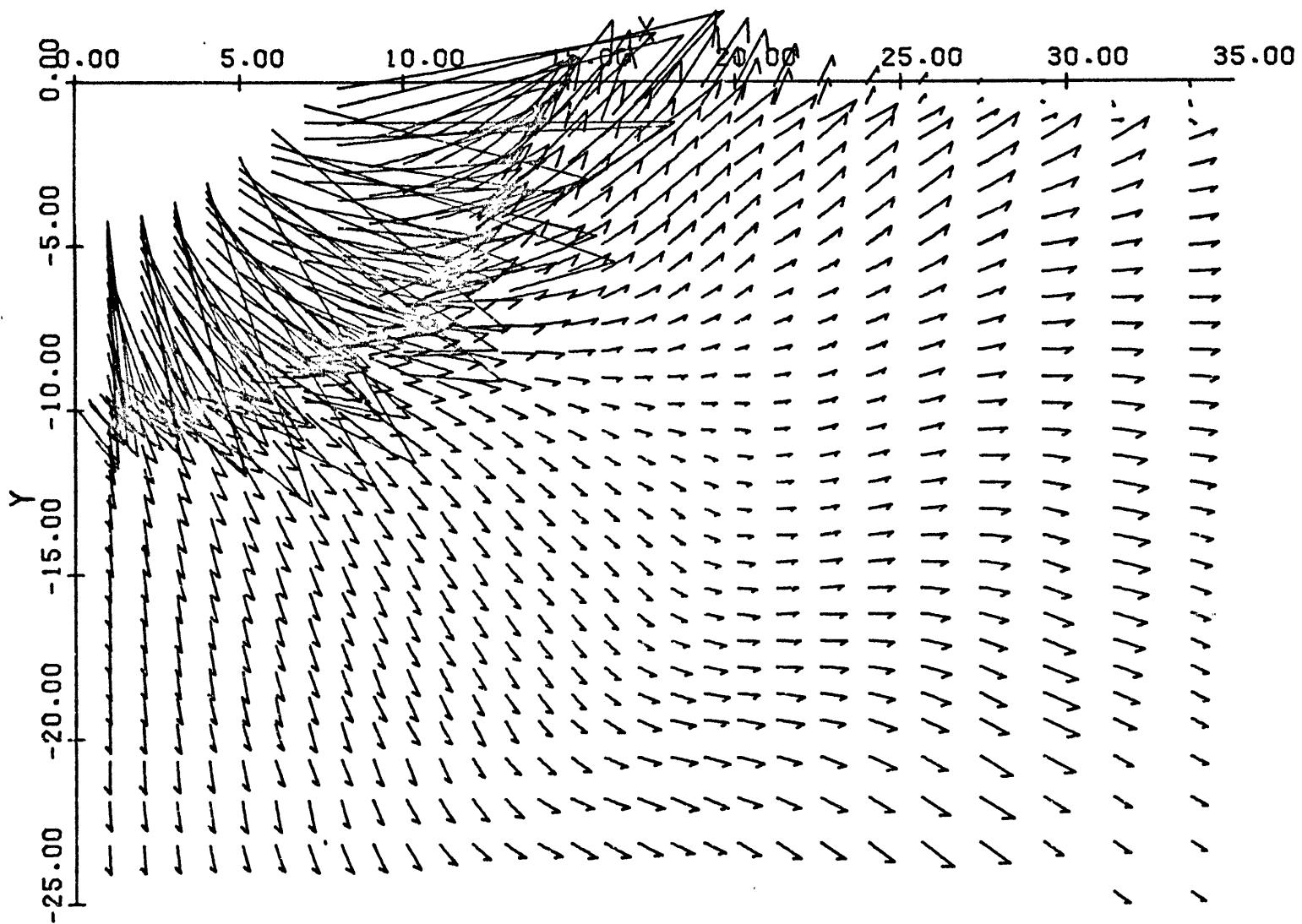


Figure 36. Velocity vector plot for MCP-21 at 5.6 msec after detonation. Velocity is proportional to the vector length with the distance between axis marks equal 100 ft/sec. Axes are in ft.

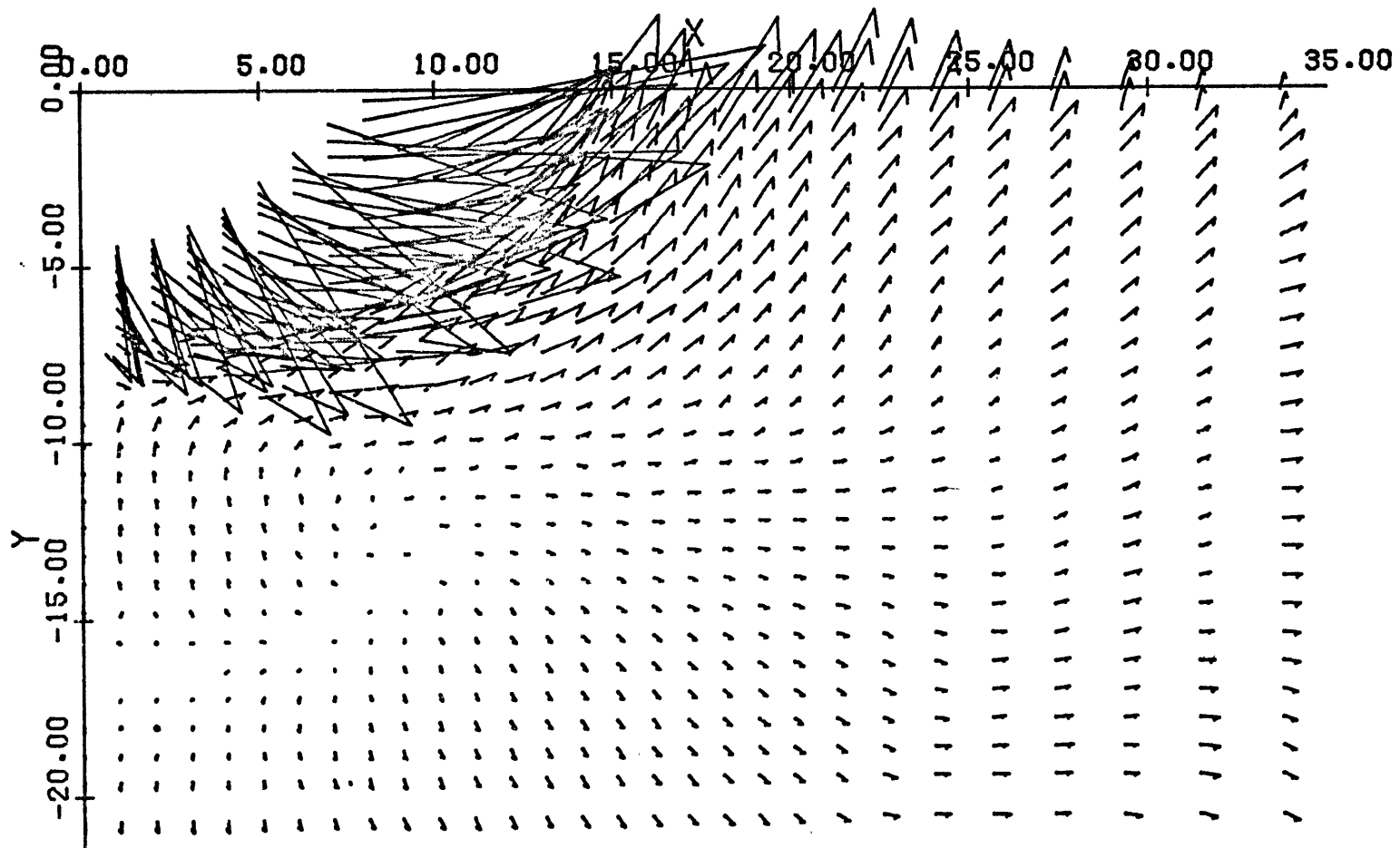


Figure 37. Velocity vector plot for MCP-21 at 6.9 msec after detonation. Velocity is proportional to the vector length with the distance between axis marks equal 100 ft/sec. Axes are in ft.

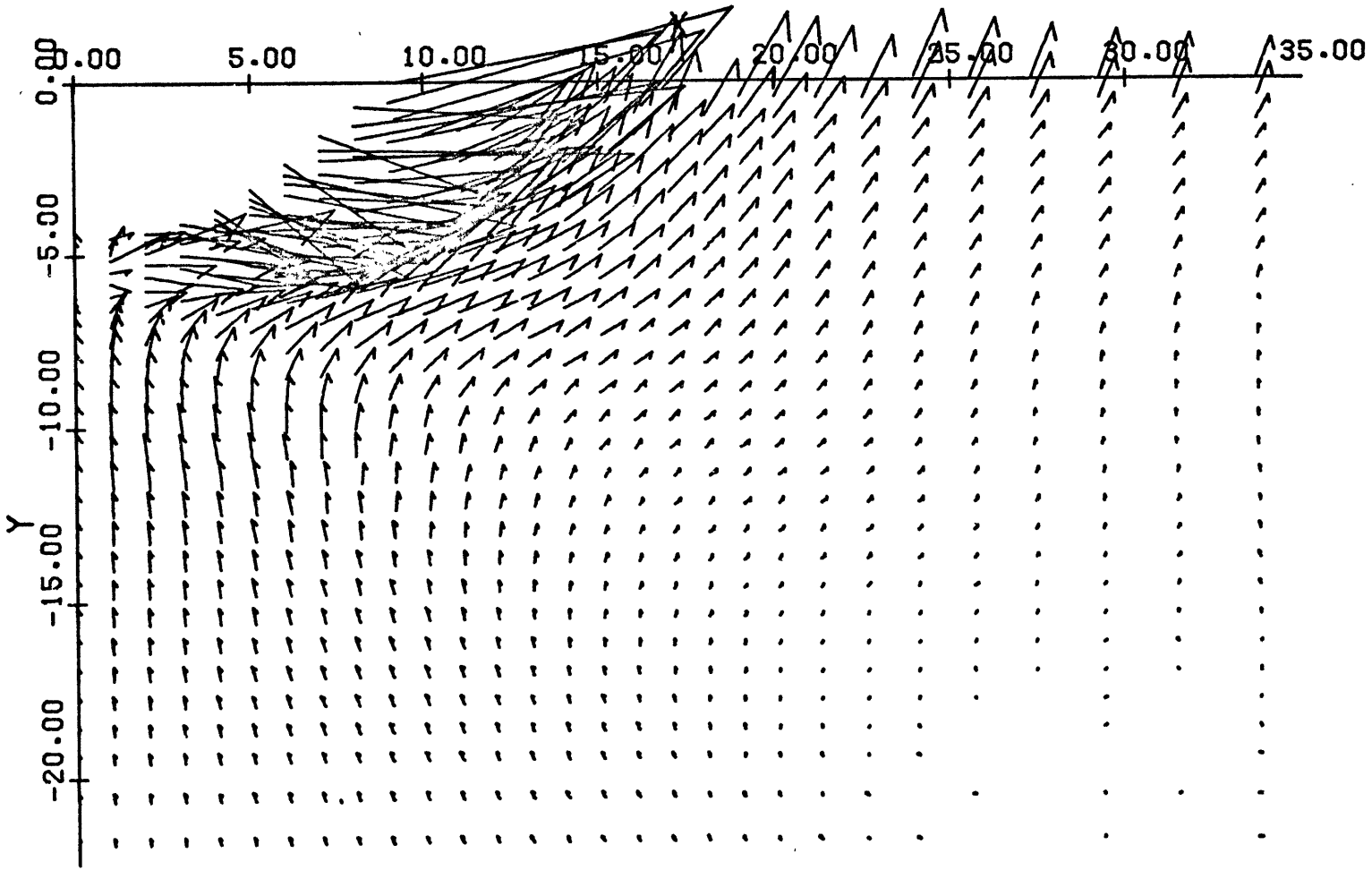


Figure 38. Velocity vector plot for MCP-21 at 10.5 msec after detonation. Velocity is proportional to the vector length with the distance between axis marks equal 100 ft/sec. Axes are in ft.

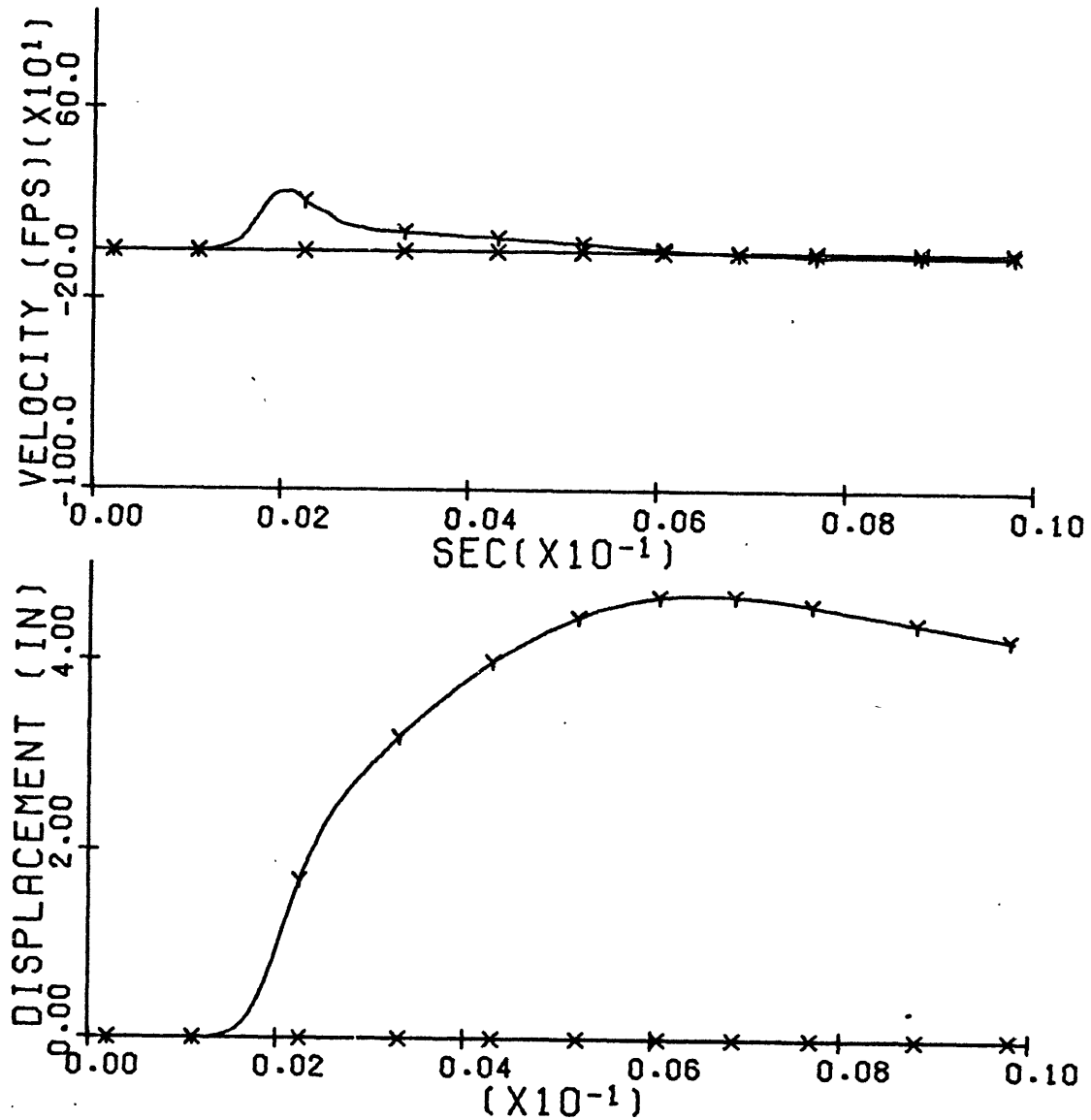


Figure 39. Motion time history for the target point originally located on the vertical axis at 12 ft depth in the MCP-21 calculation. Positive Y values indicate downward motion.

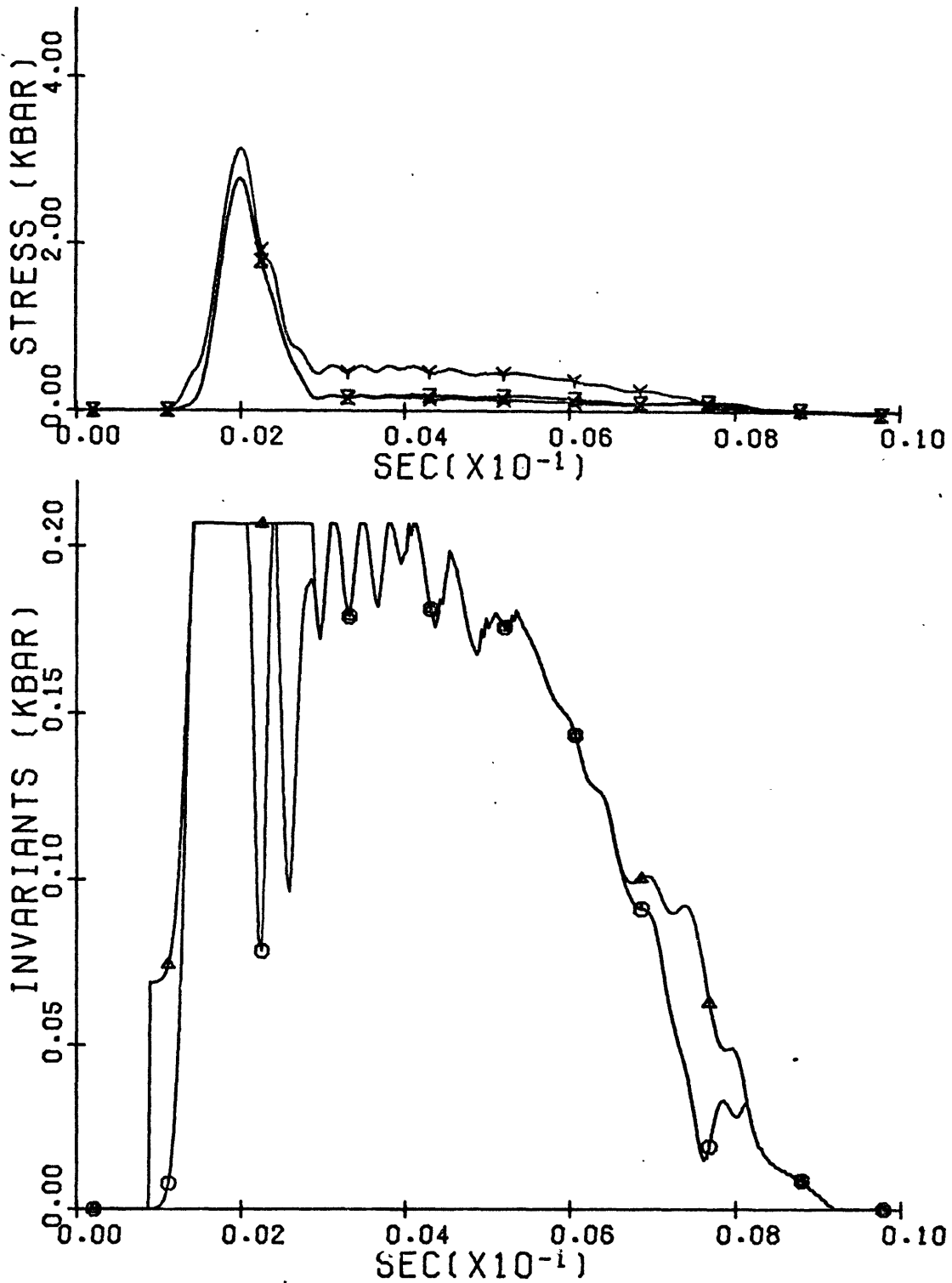
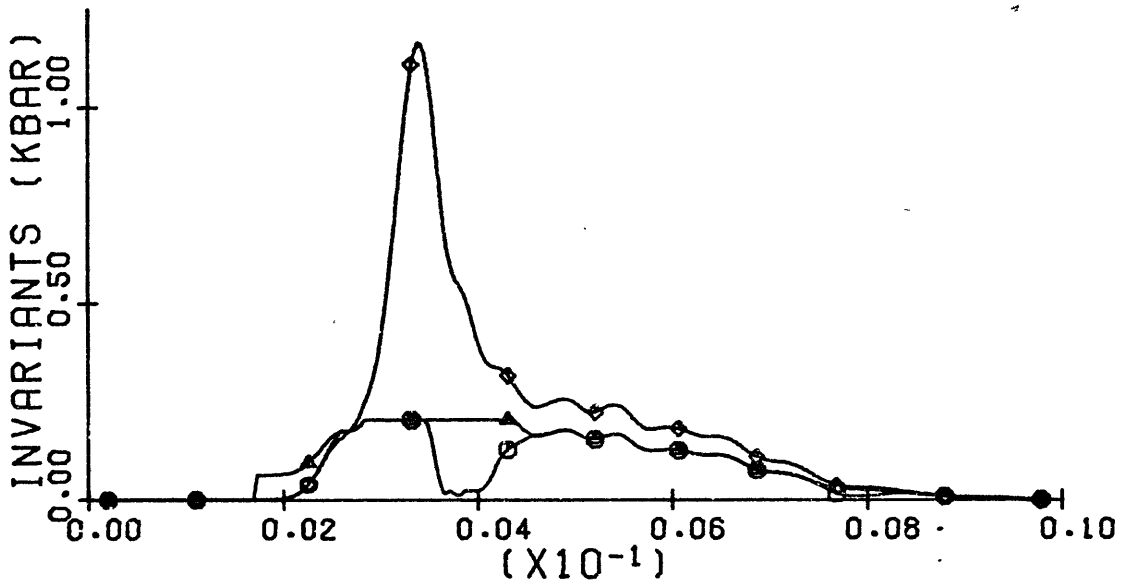
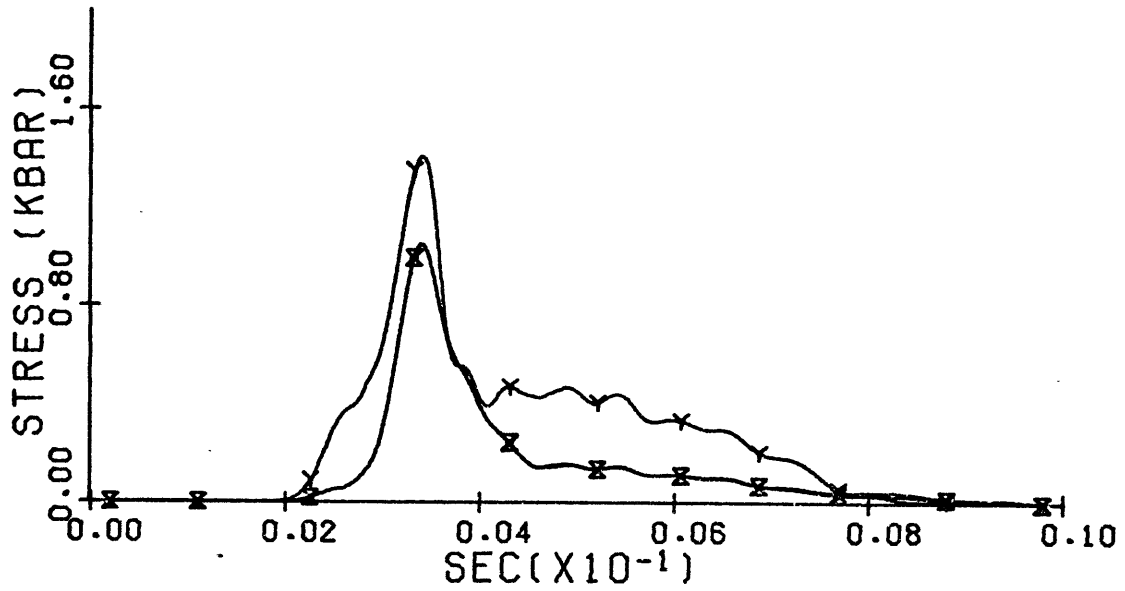


Figure 40. Stress time history for the target point of Figure 39 with compressive stresses positive. Y is vertical; X is radial; Z is tangential;  $\Delta$  is yield condition;  $\circ$  is the second invariant of the deviator stresses. The constant yield condition between 1 and 3 msec is the von Mises yield condition.



Y - vertical

◇ - pressure

X - radial

△ - yield condition

Z - tangential

○ - second invariant

Figure 41. Stress time history for the target point originally located on the vertical axis at 20 ft depth in the MCP-21 calculation. Compressive stresses are positive.

time, however, the yield surface was controlled by the Mohr-Coulomb relation, which resulted in volumetric bulking. Thus, while nearly constant stress conditions were maintained, because of the downward momentum of the material above this target point, the downward velocity was continuously reduced until the motion stopped at 6.3 msec and reversed direction. After 6.3 msec the vertical compressive stress was reduced while the horizontal normal stresses remained significant, which resulted in elastic deformation while the vertical stress approached zero. The reduction of the vertical stress lowered the pressure and, therefore, the yield condition so that the horizontal stresses were finally reduced by material yield, until material separation occurred at 9 msec.

The stress time history of the target point on the vertical axis and initially at 20 ft depth, Figure 41, provided an example of the elastic-precursor development that is actually observed in shock experiments (Ahrens and Rosenberg, 1968), and served as a simple demonstration that strength effects were properly treated by the AFTON-2A code. The first calculated stress wave arrived near a simulated time of 2.5 msec, after traveling most of the distance from the surface at a compressional wave speed of 8000 ft/sec. The main plastic wave, however, travelled with the stresses controlled by the von Mises yield condition, and the wave speed was

$$c_b = \left( \frac{K}{\rho_i} \right)^{1/2} \quad (3.16)$$

which, from relation (3.4), became

$$c_b = c_p \left[ \frac{1+\nu}{3(1-\nu)} \right]^{1/2} \quad (3.17)$$

The wave speed,  $c_b$ , computed from (3.17) was 5656 ft/sec, which was consistent with the maximum-pressure arrival near 3.5 msec. Further, from Ahrens and Rosenberg (1968), the Hugoniot elastic limit is related to the von Mises yield condition by

$$Y_{MAX} = \frac{3G P_e}{3B + 4G} \quad (3.18)$$

with  $P_e$  the maximum elastic normal stress and  $B$  the bulk modulus. Relation (3.18) was transformed to

$$P_e = 2 Y_{MAX} \left[ \frac{1-\nu}{1-2\nu} \right] \quad (3.19)$$

by elastic relations between  $B$ ,  $G$ , and  $\nu$ . With the values used in MCP-21, relation (3.19) implied a  $P_e$  of 0.56 kbar, which was the maximum normal stress at the time the von Mises yield condition was reached.

Lower "Fluid" Layer. An initial attempt was also made to apply the study of central mounds to an examination of lunar evolution. Two lunar craters, Lansberg (0°N, 26.5°W) and Reinhold (3°N, 23°W) are very similar except that Lansberg has a central peak (Figure 42) while Reinhold has no such feature (Figure 43). Reinhold is 27.5 miles in diameter and 1.7 miles deep (Schmitt et al., 1967), and Lansberg is 25 miles in diameter and 1.6 miles deep (Eggleton, 1965). These two craters are within 125 miles of each other, both being southwest of Copernicus in Oceanus Porcellarum, and are probably located in similar material. The main difference between the two craters,

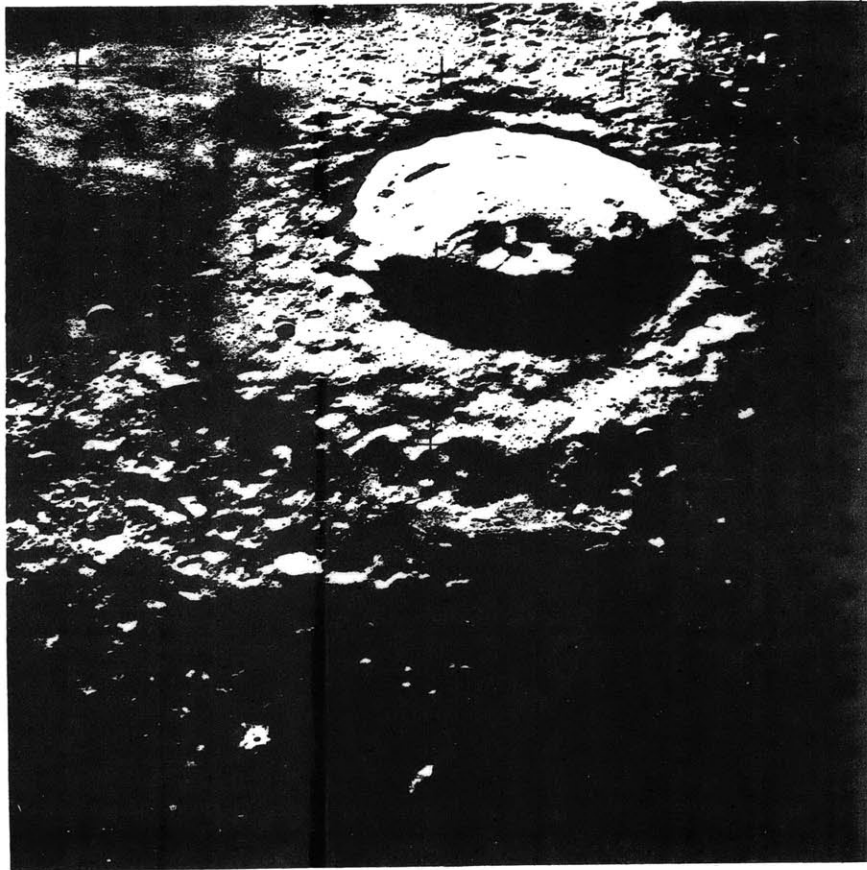


Figure 42. The lunar crater Lansberg, located near  $0^{\circ}\text{N}$ ,  $26.5^{\circ}\text{W}$  with a pronounced central peak. Crater diameter is 25 miles (Eggleton, 1965). NASA photograph AS-14-70-9824, Apollo 14.

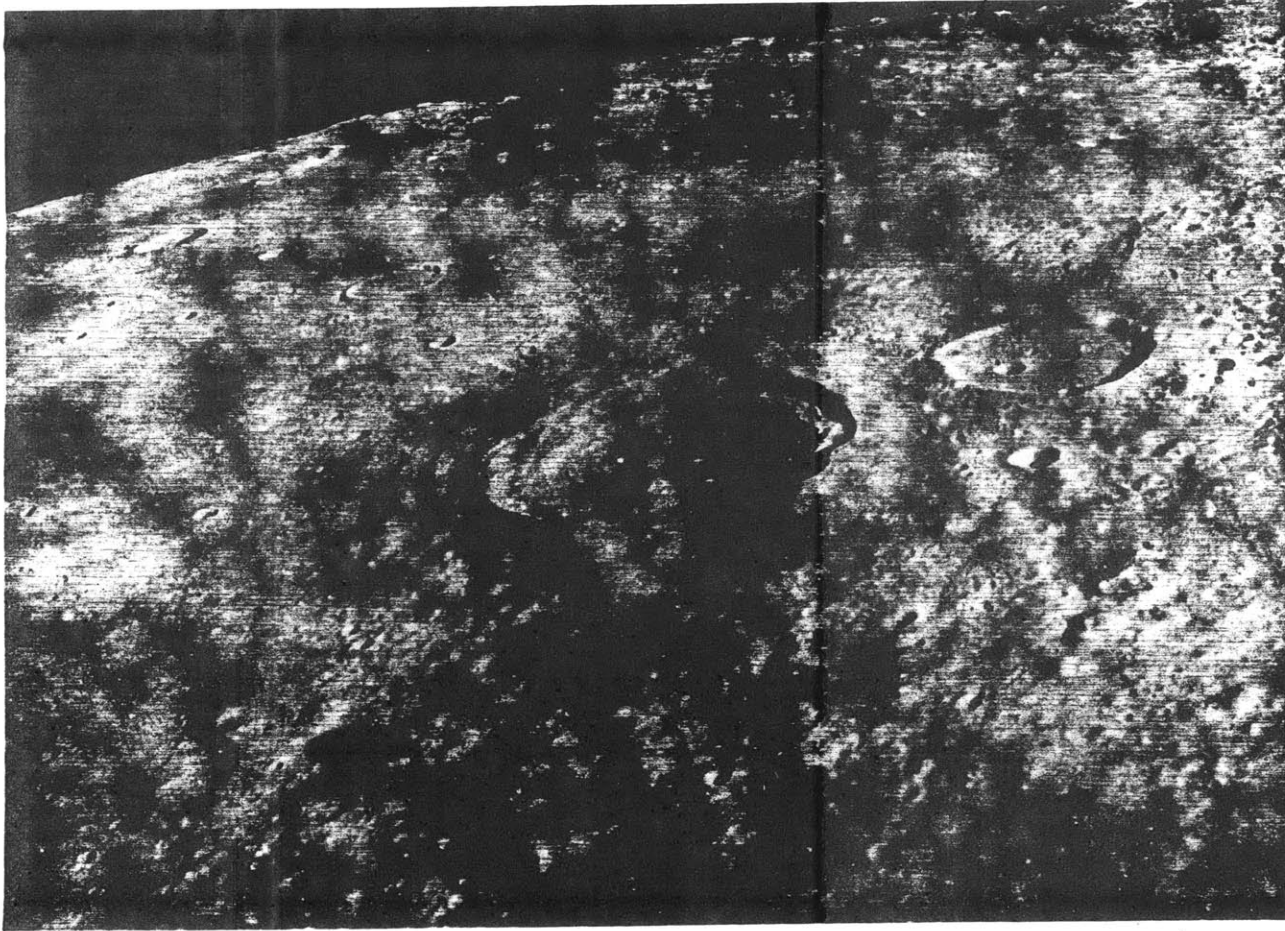


Figure 43. The lunar crater Reinhold, located near  $3^{\circ}\text{N}$ ,  $23^{\circ}\text{W}$  with no pronounced central peak. Crater diameter is 27.5 miles (Schmitt et al., 1967). NASA photograph AS-12-51-7543, Apollo 12.

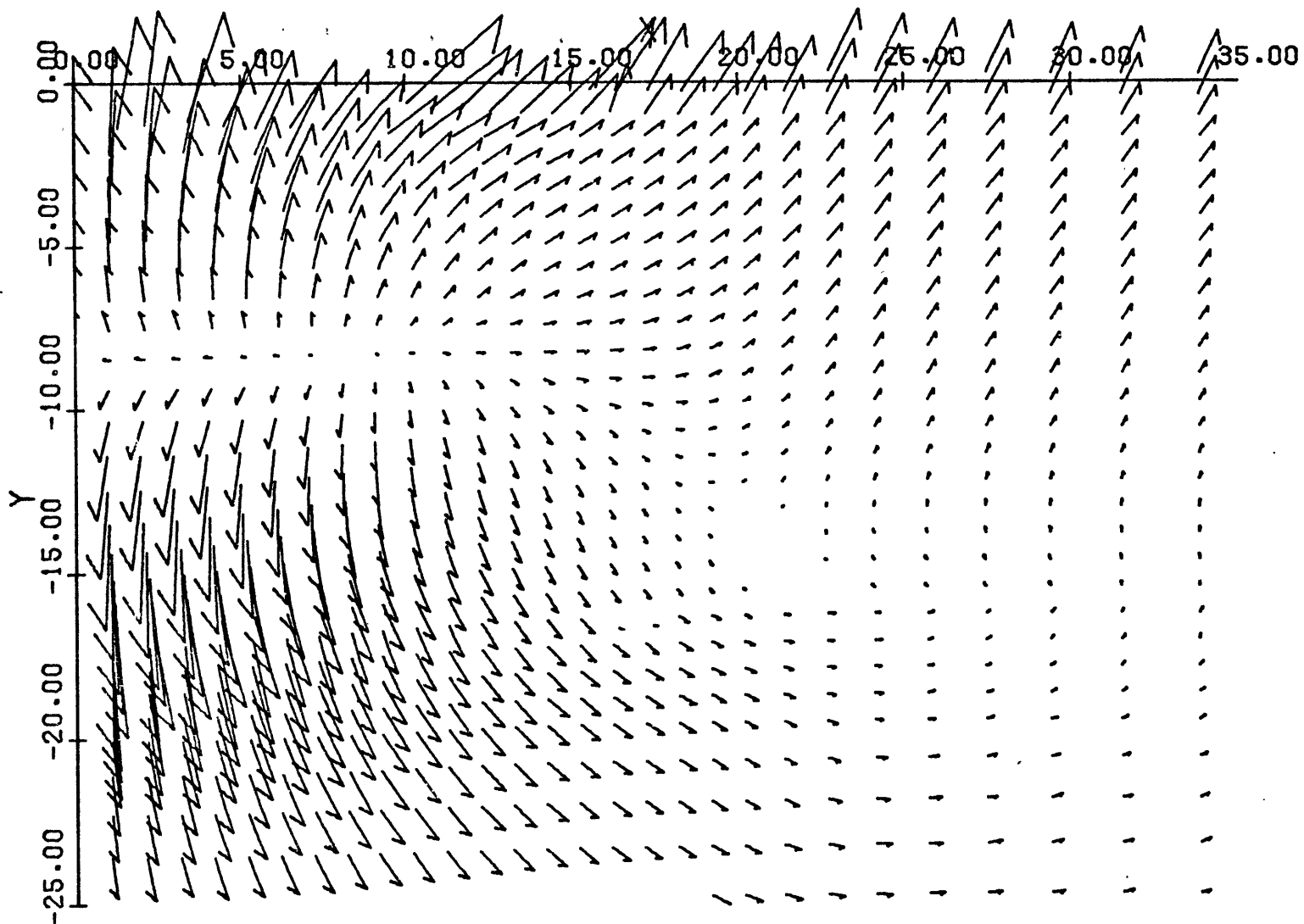


Figure 44. Velocity vector plot for MCP-12 at 16.6 msec after detonation. Velocity is proportional to the vector length with distance between axis marks equal 100 ft/sec. Axes are in ft.

other than the presence of a central mound, is that Lansberg is overlain by Oceanus Porcellarum material while Reinhold overlies that material (Schmitt et al., 1967).

One explanation of the relationship between these two craters is that conditions favoring central mound formation existed at the time Lansberg was formed and were sufficiently modified by the time of the Reinhold event to prevent the formation of a similar mound. Perhaps, at the time Lansberg was formed, a solid crust, approximately one crater radius thick, existed over a molten layer; while, by the time Reinhold was formed, the crust was much thicker. Such a relation of a growing crust is contained in several published thermal models (Toksoz et al., 1972; McConnell and Gast, 1972) and is used by Simmons et al. (1973) to account for the discontinuous increase in seismic velocity at a depth of 15 miles with a constant seismic velocity in the depth interval 15 to 30 miles on the moon.

The impact calculations required to test fully such a model of the relation between these two craters were not accomplished. However, a calculation, MCP-12, was completed that inserted a model "fluid" halfspace below 16.2 ft depth in the MCP-02 model to provide a preliminary test of the influence of such a medium. In the MCP-12 calculation the "fluid" was modeled by an incompressible hydrostat, with the values

Initial density - 2.47 gm/cc

Seismic velocity - 6000 ft/sec

$\mu_3$  - 0.0229

Poisson's ratio - 0.45

and, to simulate viscosity, a constant yield surface value of 34.5 bars for compressive pressures with material separation assumed for negative stresses. Also, since the transmitting boundary assumed impinging elastic waves, the bottom boundary was located at 156.2 ft depth. A special "sliding" interface condition, that limited the shear stress transmitted across the interface to the shear capability of the fluid (Niles et al., 1971), was used at the solid - fluid interface.

The calculated flow field at 16.6 msec, Figure 44, showed that the "fluid" layer extensively influenced the motions of the solid material above the interface. This effect was particularly strong in a cylindrical region of 15 ft range and below 9 ft depth where the motion, instead of being upward as in the MCP-02 calculation, was downward with velocities as high as 70 ft/sec. This motion was producing large downward material displacements with the cylinder of solid material, which was completely separated, moving into a developing depression in the "fluid". The motion in this "fluid" was similar to that calculated by Harlow and Shannon (1967) for the splash of a liquid drop into a deep pool, and an extension of this calculation would be expected to develop large upward velocities near the axis of symmetry as the fluid recovered under gravitational flow. The amount of this recovery would be controlled by the properties of the fluid, which is speculated to control also the development of a central mound formed by the solid material as that material is redirected upward by the fluid.

Chapter IV. Discussion and ConclusionsDiscussion

Evaluation of Results. Numerical modeling of physical events is subject to two basic causes of error. One of these causes is the numerical error caused by replacing the space and time continuums with a discrete grid on which calculations are accomplished at specific moments in time. This form affects the accuracy of the calculated numerical values and usually can be reduced by decreasing the grid spacing and calculational time increments. Evaluation of this form of error in complex calculations can only be inexact; however, from previous investigations of numerical error in the AFTON-2A code (Cooper, 1971; Trulio et al., 1967), such errors are not expected to affect seriously relations between calculated values. The second, and more serious, cause of error is the use of invalid mathematical models for the actual physical processes. This cause of error can not only result in numerical values that are incorrect, but also can result in a calculated response that is completely invalid.

The Mixed Company II numerical simulation, MC 2.12, was subject to modeling errors of both forms in the three models. The first was the model of the overpressure boundary condition used to simulate the high-explosive event. This model has been suggested (Trulio and Perl, 1973) to underestimate the overpressure impulse of the Middle Gust III event by at least 40% at ground zero. The second was the model of the ground response

to the overpressure boundary conditions during the first 16.4 msec. This model included only approximations of 1) the test site, 2) the properties of the materials at that site, and 3) descriptions of physical relations. The third model was the ballistic extension of the calculated conditions at 16.4 msec.

A necessary, but not sufficient, condition for the models to provide a simulation of the actual physical processes is that the calculated final conditions are the same as the final conditions observed after the physical event. The results of the Mixed Company II numerical simulation do not completely meet this condition; however, the calculation may still be useful to a study of central peak mechanics if the inadequacies of the models do not include the causes of central mound formation.

Thus, the interpretation that the model produced insufficient displacements below ground zero is considered to be the major discrepancy of the simulation. Since the ballistic extension model is not expected to underestimate the displacements, the cause of this discrepancy is thought to exist in at least one of the first two models. One possible cause is that the impulse of the model overpressure was too low. An increase of the overpressure impulse would cause a stronger shear wave and more bulking, because the stresses and the compressional pressure duration would be greater. Another possible cause is that the dependence of the yield surface on the third invariant of the deviator stresses was not included in the yield model. In many natural materials the yield surface is dependent on the third invariant (White, 1973), which indicates that the yield

model used in the numerical calculations was incomplete. Other possible causes of the discrepancy include errors in the values used to model the test site and numerical error.

Mechanical Model of Central Mound Formation. However, the development of a model of the causes of central mound formation is warranted because the final conditions calculated in the Mixed Company II numerical simulation are sufficiently similar to the observed conditions after the physical experiment. The results of the numerical experiments (Table IV) can be used as a guide to this model. In this model, the principal cause of central mound formation is the rebound of material following the maximum shock pressure. If this rebound is sufficiently reduced by compaction of the materials, a central mound will not form in the crater unless there is a material below the bottom of the crater that responds like a fluid to produce a gravitational splash jet. The rebound must occur in the region where material strengths are sufficient to retard some of the outward displacements caused by the initial compressional wave. The formation of the central mound is enhanced by the bulking of material as the material brecciates and by the inward motion caused by the principal shear wave. Inward displacements, however, are associated with a ductile response of the material. The presence of material discontinuities below the forming crater will reflect stress waves that might add to the formation of a central mound. Because of the reduced density in the region forming the central uplift, a period of material separation exists that may allow the gravitational sliding of the crater

TABLE IV  
SUMMARY OF NUMERICAL SIMULATION RESULTS

	<u>Model Designation</u>	<u>Baseline Model</u>	<u>Model Change</u>	<u>Major Result</u>	<u>Page Ref.</u>
1.	MC 2.12*	Numerical Simulation of Mixed Company II with a Hydrostatic Compaction Factor (page 53) of 10%		Generally Consistent with Observations	61
2.	MC 2.13*	MC 2.12	30% Compaction	No Central Mound	80
3.	MCP-09*	MC 2.13 MC 2.12	10% Compaction Different Release Adiabat	Like MC 2.12	84
4.	MC 2.15	MC 2.12	Cohesion Retained	No Central Mound	91
5.	MCP-02*	No Compaction Two Layers	-	Central Mound	87
6.	MCP-01	MCP-02	No Soil	Little Change In Central Mound	87
7.	MCP-03	MC 2.12	No Compaction	Increased Velocities	83
		MCP-02	4 Layers	Little Change	90
8.	MCP-05*	MCP-02	No Bulking (page 59)	Completely Different	97

(table continued)

TABLE IV (CONTINUED)

	<u>Model Designation</u>	<u>Baseline Model</u>	<u>Model Change</u>	<u>Major Result</u>	<u>Page Ref.</u>
9.	MCP-06	MCP-02	No Yield	Large Transient Velocities	96
10.	MCP-07	MCP-02	Shift During Yield	No Change	93
11.	MCP-08	MCP-02	Shift After Yield	No Change	93
12.	MCP-12*	MCP-02	"Fluid" Layer	Probable Fluid Splash	112
13.	MCP-21*	MCP-02	0.21 Kbar Yield	Deeper Upward Motions	99

\* Important Implications For Central Peak Formation

walls along deep slip surfaces to produce additional inward displacements.

Applications to Previous Information. The general applicability of this mechanical model of central mound formation can be tested by comparisons with previous observations of central mound occurrence. Such a model should also provide a means of understanding and evaluating previous calculations.

Comparisons should first be made with the high-explosive experiments to determine if such a model is successful under loading conditions similar to those for which the model was first determined. The absence of central peaks in the 20 ton detonations in Canada would be attributed to the compactibility of the top 25 ft of soil at that site. The presence of central mounds in the higher-yield experiments would indicate that the lower, less-compactible material was being significantly influenced. The ductile characteristics of the deformation in those central mounds can either be attributed to the independence of the yield surface on confining pressure, or to a "fluid" action of the material below 25 ft depth. The occurrence of a central mound in the 100 ton spherical event, and not in the 100 ton hemispherical event, can be attributed to an increased pre-compaction of the soil below the spherical charge combined with an increased overpressure impulse at ground zero. The mechanical model is also applicable to the Mixed Company test series. The Mixed Company I and III high-explosive detonations certainly caused higher stresses in the medium, which caused more ductile-like behavior of the layer at 12 ft, than the Mixed

Company II experiment. This ductile-like behavior resulted in less-pronounced central mounds in the first and third experiments than the large breccia cone of the Mixed Company II event. Further evidence of the effect of a change in yield mode is provided by the central mound of the Mixed Company I experiment with the intact flanks and the brecciated central core. The Middle Gust series is less easily interpreted because of the jointing in the test sites; however, the test series does indicate that the more ductile-like behavior of the material at the Middle Gust sites than at the Mixed Company site resulted in more subdued central mounds. The transition from central mounds to the central trough of the Middle Gust III event was caused by the higher stresses that reached the lower shale layer. Comparisons between the three test series illustrate the influence of compactibility on the occurrence of central mounds, and of yield mode on the deformation in the central mound.

Comparisons with impact structures provide a test of the applicability of the model to a different form of loading. As the presence of shatter cones indicates, the maximum stresses in the central mounds were above, but near, the Hugoniot elastic limit, producing ductile failure with eventual inward displacements. The change in the yield mode at increased depths results in a central mound with a breccia core of reduced density. The dependence on gravity, suggested by Hartmann (1972), would be caused by the initial overburden stresses reducing the porosity of deeper material, combined with the additional rebound caused by the dynamic excavation of the crater. The increased

pressures caused by the lithostatic load would also cause a higher Mohr-Coulomb yield value, which would increase the bulking and shear-wave magnitude. The change from central peaks to peak rings may be caused by a gravitational collapse of the breccia core or a complete penetration of a solid crust. The transition from simple to complex impact structures in Canada may be caused by similar gravity influences combined with a weathering of the Canadian shield to a depth of one to two miles, with an increased jointing, porosity, and a reduced material strength.

A further test of the model is actually provided by its use to explain why central peaks do not occur in some shock-wave-cratering events. The Barringer crater has no central mound because it was formed in porous sandstone. All the nuclear tests occurred in, or over, compactible material. The hypervelocity impact experiments in loose sand targets produced only simple crater shapes.

An understanding of the results of previous calculations is facilitated by use of the mechanical model. Since the ELK-31 soil model was precompactd before the beginning of the calculation, upward motions were calculated only in that numerical simulation of the Distant Plain 6 experiment. Upward motions were calculated in the Sierra Madera numerical simulation, which was considered to model successfully the event. However, the motions in this calculation resulted from invalid physical models. In particular, a no-strength condition was assumed once the calculated pressure in a zone was negative. Because of this

assumption, the calculation actually simulated the response to gravitational force of a perfect fluid surrounding an initial void. Evidence supporting this interpretation of the calculation is that the calculated motions required a simulated time of 15 sec to develop fully and were still prevalent at a simulated time of 30 sec. Errors in the calculational model which probably reduced the earlier upward velocities included the use of information from only a Hugoniot curve to determine all the parameters of an equation-of-state, and an initial yield strength of 0.2 kbar that was independent of pressure.

### Conclusions

Based on results of the numerical calculations, four major conclusions were reached:

- 1) A central peak will form in a crater in a solid medium when the rebound of material from maximum compression is sufficient.
- 2) The rebound mound must occur in the region of the medium where material yields but the material strength is significant compared to the maximum stresses.
- 3) The rebound mound is significantly enhanced by plastic volumetric increases that occur during yielding when material strength is a function of pressure.
- 4) The presence of a fluid-like material below a solid layer might also cause the formation of a central peak in a shock-produced crater.

These conclusions form the basis of a model of the mechanics

of central peak formation.

Because the observed occurrence and structural relations of central peaks in craters produced by high explosive, nuclear, and hypervelocity impact events can be explained using the mechanical model, I conclude that this model describes the causes of central mound formation in shock-wave-cratering events. These peaks are structures that are controlled primarily by the properties of the cratered medium. The properties of the source of energy for the cratering event influence central mound formation only by modifying the stress distribution in the cratered medium. Shear waves and stress-wave reflections from discontinuous increases in acoustic impedance enhance central mound formation, but are not the primary cause. Deep gravitational sliding may occur and increase the inward displacement of material, but this process is an effect rather than a cause of central mound formation.

Also, since the occurrence and structure of a central uplift is controlled by the properties of the cratered medium at the time of the shock-wave-cratering event, these structures provide a record of those properties. With the mechanical model as a guide, this record may be useful in examining the evolutionary and spatial relations of the media in which shock-wave-cratering events have occurred. Evolutionary models of solar-system bodies can be constrained by the structure of craters observed in spacecraft photography.

Because the processes of the mechanical model are described in the calculational code, that code becomes a tool that can be

used to examine occurrences of central peaks. Such an application to larger-scale events with higher maximum pressures and different loading conditions will require extensive modifications to the actual code used during this study. These changes include a more general equation-of-state, an active inclusion of initial lithostatic stresses, and a different scheme of grid definition. However, the modifications can be made within the present calculational structure of the AFTON-2A code.

### Future Work

The results of the MCP-12 numerical experiment indicate that the presence of a "fluid" below a solid crust will change significantly the response of the crust to a shock-wave-cratering event. The manner of this change is speculated to eventually result in the development of upward motions in the solid medium. Therefore, the structural relations between the craters Lansberg and Reinhold might be the result of a growing lunar crust. A program to simulate numerically the events which caused these two craters is recommended. While such a simulation could be completely accomplished with the AFTON-2A code, I recommend that only the early part of the Lansberg calculation, to develop the velocity distribution in the lower layer, be accomplished with that code. The results of this part would then be used as initial conditions in a code that explicitly and more efficiently treated viscous flow.

Both laboratory and numerical experiments should be accomplished to determine if the momentum and energy density of a hypervelocity impact have any special influence on the general

structural characteristics of an impact crater. Since crater size has been related to the energy of the event (Baldwin, 1973), if the influence of momentum could be determined then the mass and velocity of the impacting body could be estimated. If the influence of energy density on crater structure could be determined, then the density of the impacting body could also be determined.

In the yield model used to accomplish the calculations, the assumption that the yield surface was independent of the third invariant of the deviator stresses is not valid generally. The general associated-flow-rule is dependent on the third invariant (Trulio et al., 1969), and at least one model of the dependence of the yield surface on the third invariant exists (White, 1973). The need for including this addition in the AFTON-2A yield model should be examined further.

Data on occurrence of central peaks should be reviewed for spatial and age relationships. For example, if the lunar craters of 25 miles diameter that had central mounds had similar age characteristics, then conditions favorable to central mound formation would have occurred at the time those craters were formed. Then, if that time varied with crater size, the evolution of those conditions could be examined. Also, Manley et al. (1973) reported that the distribution of central peaks in the cratered areas on Mars is characterized by clusters and seems non-random. They stated that the curve of central peak frequency vs. crater diameter has a maximum at a crater diameter of 5 to 7.5 miles and decreases rapidly as the diameter increases.

They also reported that large numbers of central peaks occur in craters of 2.5 to 7.5 mile diameters, with 10% of those craters having multiple peaks. The physical model of Mars should be examined for special conditions which would favor central mound formation between 1 and 4 miles deep. Similar examinations should also be made of the photographic information on Mercury. Such studies would provide important guides to evolutionary models.

## Appendix I.

Computation Parameters

The complete set of computation parameters for all the numerical experiments described in the text may be divided into two categories. The first category includes the parameters that were not varied during any of the problems. These parameters are given once in this appendix and apply to all the numerical experiments. The second category includes the parameters that were varied for at least one of the numerical experiments. These parameters are given for the reference calculations and the variations are described for each of the other numerical experiments.

Constant Numerical Parameters

1. Explosive Yield - 20 tons TNT
2. Initial time - 0.206 msec
3. Gravitational acceleration - 32.2ft/sec
4. Artificial Viscosity coefficients
  - Bulk linear constant - 0.06
  - Bulk quadratic constant - 4.0
  - Deviatoric quadratic constant - 4.0
  - Deviatoric linear constant - 0.06
5. Calculation Grid definition

## Radial Coordinates:

	Initial (ft)	Number	Initial Spacing (ft)	Growth Rate
First Region	0	21	1.0	1.0
Second Region	20	40	1.2	1.1

## 5. Continued

## Vertical Coordinates

	Initial (ft)	Number	Initial Spacing (ft)	Growth Rate
First Region	0.	4	-0.6	1.0
Second Region	-1.8	22	-0.8	1.0
Third Region	-19.4	16*	-1.13	1.1

\*for MCP-12 changed to 27

## 6. Initial target point coordinates - 100 locations formed by combinations of:

X Coordinate (ft) 0., 2., 4., 6., 8., 10., 14.,  
18., 22., 26.

Y Coordinate (ft) -1., -2., -3., -4., -6., -8., -10.,  
-12., -16., -20.

## 7. Material Properties

	<u>Layer 1</u>	<u>Layer 2</u>	<u>Layer 3</u>	<u>Layer 4</u>
Initial Density (gm/cc)	1.875	2.35	2.47	2.35
$\mu_3$	0.2366	0.051	0.0229	0.051
$\mu_s$	0.50	0.30	0.27	0.30
$K_m$ (kbars)	680	680	680	680
Sublimation Energy ( $\times 10^{12}$ ergs/gm)	0.02	0.02	0.02	0.02
A ( $\times 10^{-12}$ gms/erg)	3	3	3	3

## Problem Specifications.

a. MC 2.12	<u>Layer 1</u>	<u>Layer 2</u>	<u>Layer 3</u>	<u>Layer 4</u>
Depth to top (ft)	0.0	-1.8	-11.4	-19.4
$c_L$ (ft/sec)	500	8000	9000	8000
$c_u$ (ft/sec)	1250	9000	10000	9000
$c_v$ (ft/sec)	500	8000	9000	8000

a. MC 2.12 (continued)

	<u>Layer 1</u>	<u>Layer 2</u>	<u>Layer 3</u>	<u>Layer 4</u>
Poisson's Ratio	0.25	0.20	0.25	0.20
$\tau_o$ (bars)	0.7	68	51	68
$\tan \phi$	0.466	0.7	0.75	1.0
$Y_{MAX}$ (kbars)	0.5	7.5	2.1	11.6
tension limit (bars)	0	-68	-68	-68

b. MC 2.13: MC 2.12 with the changes

	<u>Layer 1</u>	<u>Layer 2</u>	<u>Layer 3</u>	<u>Layer 4</u>
$c_u$ (ft/sec)	1250	11000	12000	11000

c. MC 2.15: MC 2.12 with no yield surface shift and the changes

	<u>Layer 1</u>	<u>Layer 2</u>	<u>Layer 3</u>	<u>Layer 4</u>
tension limit (bars)	0	0	0	0

d. MCP-01: MCP-02 with Layer 2 in the Layer 1 position also.

e. MCP-02:	<u>Layer 1</u>	<u>Layer 2</u>
Depth of top (ft)	0.0	-1.8
$c_L$ (ft/sec)	500	8000
$c_u$ (ft/sec)	1250	8000
$c_v$ (ft/sec)	500	8000
Poisson's Ratio	0.25	0.20
$\tau_o$ (bars)	0.7	68
$\tan \phi$	0.466	0.7
$Y_{MAX}$ (kbars)	0.5	7.5
tension limit (bars)	0	-68

f. MCP-03: MCP-02 with the changes

	<u>Layer 3</u>
depth to top (ft)	-11.4
depth to bottom (ft)	-19.4
$c_L$ (ft/sec)	9000
$c_u$ (ft/sec)	9000
$c_v$ (ft/sec)	9000
Poisson's Ratio	0.25
$\tau_o$ (bars)	51
$\tan \phi$	0.75
$Y_{MAX}$ (kbars)	2.1
tension limit (bars)	-68

g. MCP-05: MCP-02 with the Prandtl-Reuss flow rule only.

h. MCP-06: MCP-02 with no yield allowed.

i. MCP-07: MCP-02 with yield surface shifted only before yield calculation.

j. MCP-08: MCP-02 with yield surface shifted only after yield calculation.

k. MCP-09: MC 2.12 with the changes

	<u>Layer 1</u>	<u>Layer 2</u>	<u>Layer 3</u>	<u>Layer 4</u>
$c_u$ (ft/sec)	1250	11000	12000	11000
$c_v$ (ft/sec)	500	4775	6164	4775

l. MCP-12: MCP-02 with the changes

	<u>Layer 3</u>
depth to top (ft)	-16.2
$c_L$ (ft/sec)	6000
$c_u$ (ft/sec)	6000
$c_v$ (ft/sec)	6000
Poisson's ratio	0.45
$\tau_o$ (bars)	34
$\tan \phi$	.75
$Y_{MAX}$ (bars)	34
tension limit (bars)	0

m. MCP-21: MCP-02 with the change that  $Y_{MAX}$  in Layer 2 was 0.21 kbars.

## Appendix II.

The AFTON-2A Code

The theory of the AFTON-2A code has been documented in Air Force Weapons Laboratory technical reports (Trulio, 1966; Trulio et al., 1969; Niles et al., 1971). Since the work accomplished during this study did not include any modification of that theory, this description is not significantly different from the description provided in those reports. However, in order to provide a more complete document, the description of the theory of the AFTON-2A code by Niles et al. (1971) will be repeated.

Finite Difference Meshes and Zones in AFTON-2A

The finite difference technique used in the AFTON codes is of the "time-marching" kind. That is, the space continuum is replaced by a discrete mesh of points, and, starting with a system in a known state at some initial time, the variables of the motion are updated by a discrete time increment at all points of the space mesh, according to the finite difference equations of motion. The updating process is then repeated using the just-calculated values of the variables of the motion as fresh initial value data, and so on. Owing to the assumed symmetry of the motion, a space mesh for AFTON-2A need only be defined as an array of points in a single azimuthal plane, the variables of the motion having identical values at corresponding points of all azimuthal planes. The points of an AFTON-2A finite difference mesh are logically equivalent to the corner

points of a set of unit squares which cover a rectangular region in one-to-one fashion. The mesh points are therefore the vertices of quadrilaterals which can be produced by the continuous distortion of a rectangular array of unit squares. The region of two-dimensional axisymmetric flow is thus covered by elementary quadrilaterals; these quadrilaterals are the "zones" of the finite difference mesh. Actually, it is basic to the method of differencing which underlies the AFTON codes that real physical systems have finite extension in a direction normal to the symmetry plane in which the quadrilaterals lie. A quadrilateral zone is thus just a cross-section of a quadrilateral wedge in a single azimuthal plane of symmetry. The quadrilateral wedge, a solid figure, is the basic geometric entity of the AFTON-2A finite difference mesh, and is shown schematically in Figure II-1. It is a polyhedron bounded by two nearly-parallel azimuthal planes, and having similar quadrilateral cross-sections in all azimuthal planes between the two. Four trapezoidal faces normal to the central quadrilateral complete the polyhedron.

The integral equations and associated finite difference equations which are basic to AFTON-2A have been written in sufficient generality to include non-Lagrangian as well as Lagrangian descriptions of continuum motion. The code itself contains a subroutine which defines the coordinate system to be used for any given problem. However, the Lagrangian case will be discussed, since the finite difference technique as it applies to AFTON-2A is most simply explained for that case.



The points of the finite difference mesh are then mass points whose velocities provide a discrete approximation to the material velocity field of the continuous medium.

In the Lagrangian case each quadrilateral wedge is a finite mass element consisting of the same material particles at one time as at any other time, and a quadrilateral zone - a cross-section of a quadrilateral wedge in a symmetry plane - is defined by one specific set of co-planar particles. Motion of the vertices of a quadrilateral wedge therefore produces a distortion or strain in the wedge and causes changes in all the flow variables, for a finite element of material.

The Calculation of Thermodynamic Variables in AFTON-2A for Lagrangian Meshes.

The variables of the motion are divided into two classes, namely, those associated with the vertices of zones, and those associated with their interiors. The first class (dynamic variables) consists of mesh or grid point positions and their time derivatives (i.e., their velocities) while the second class (thermodynamic variables) includes strain, stress, and internal energy. For the calculation of zone-centered variables two assumptions are made:

- a. A material element which initially occupies the region enclosed by a quadrilateral wedge always has the shape of a quadrilateral wedge (i.e., straight lines of mass-points deform to straight lines of mass-points.)
- b. Zone-centered variables are constant in value throughout a quadrilateral wedge at any given time,

and also change at a constant rate during any particular timestep.

With respect to assumption (a), the particles initially comprising a side of a quadrilateral zone will, in general, not remain co-linear; likewise, the corresponding face of the quadrilateral wedge associated with the zone usually will not, in physical reality, remain a quadrilateral. Rather, a trapezoidal Lagrangian surface of the quadrilateral wedge will deform into a more general curved shape. Assumption (a) therefore imposes a nonphysical constraint on the system, which is part of the price paid for replacing the space continuum by a discrete mesh of points. Obviously, assumption (b) entails a similar nonphysical restriction; real physical stresses and strains generally vary continuously over finite distances.

The calculation of the change in the volume of a quadrilateral wedge produced by the motion of the vertices of its associated quadrilateral zone provides the key to the construction of the finite difference equations of AFTON-2A. In making the calculation, the following definitions and conventions are adopted:

1.  $V$ ,  $\underline{R}$ ,  $\underline{U}$ ,  $\underline{A}$  denote volume, position vector, material velocity vector, and vector area, respectively.
2. The superscripts  $n$  and  $n-1$  refer to a "later time"  $t^n$ , and an "earlier time"  $t^{n-1}$ , separated by the interval  $\Delta t^{n-\frac{1}{2}} = t^n - t^{n-1}$ .
3. If no superscript is attached to a variable, it is understood to be defined at some time between  $t^{n-1}$

and  $t^n$ . In particular, the position vector of a point, without a superscript, is by definition equal to the arithmetic mean of the positions of the point at the two times  $t^n$  and  $t^{n-1}$ , i.e.,

$$\underline{r} = \frac{1}{2} ( \underline{r}^n + \underline{r}^{n-1} ) \quad (\text{II-1})$$

4. The particle velocity of a point is related to its position  $\underline{r}^{n-1}$  and  $\underline{r}^n$  at the times  $t^{n-1}$  and  $t^n$  according to

$$\underline{u} = \frac{\underline{r}^n - \underline{r}^{n-1}}{\Delta t^{n-\frac{1}{2}}} \quad (\text{II-2})$$

5. Position and velocity subscripts refer to the mesh points labeled as numbers in Figures II-1 and II-2.

The underlined subscripts 2, 3, a, and d, shown schematically in Figure II-2, refer to points on the side of zone "a". The coordinates of point 2, for example, are defined by the equations

$$x_{\underline{2}} = \left( \frac{x_2^2 + x_2 x_3 + x_3^2}{3} \right)^{1/2} \quad (\text{II-3})$$

and

$$y_{\underline{2}} = \frac{(x_3 - x_{\underline{2}}) y_2 + (x_{\underline{2}} - x_2) y_3}{x_3 - x_2} \quad (\text{II-4})$$

The coordinates of the points 3, a and d are found in a similar fashion.

Equation (II-2) involves the kind of discretization error entailed in assumption (b) above; in this case the velocity is taken to be constant over a finite time interval, namely  $\Delta t$ .

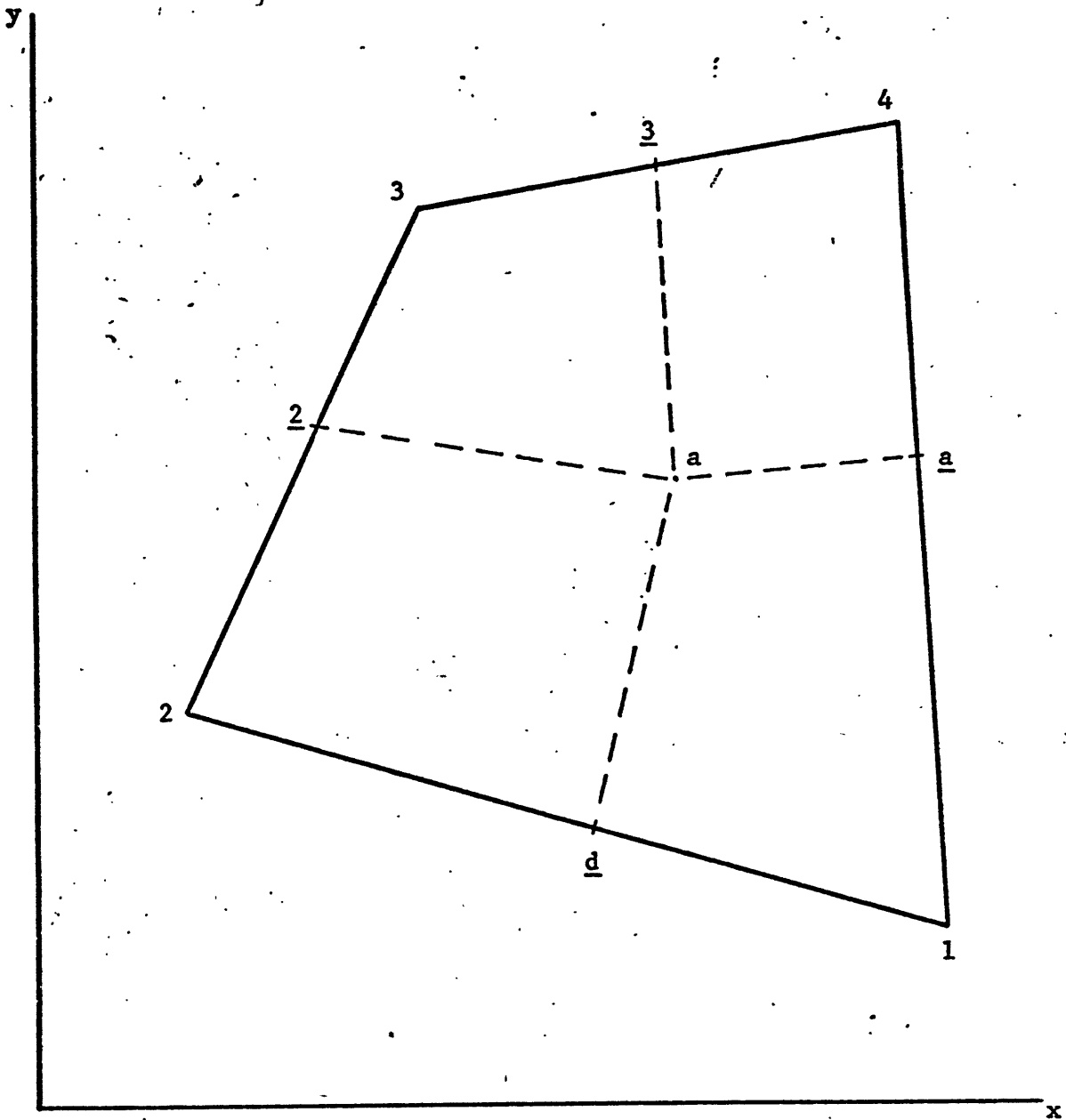


Figure II-2. Projection of the Cross-Section of a Quadrilateral Zone in the x-y Plane.

An exact calculation of the volume of a quadrilateral wedge shows that

$$\frac{V^n - V^{n-1}}{\Delta t^{n-1/2}} = \sum_{i=1}^4 \underline{A}_i^{n-1/2} \cdot \underline{U}_i^{n-1/2} \quad (\text{II-5})$$

where the index  $i$  refers to the vertices 1,2,3,4 of the quadrilateral designated "a" in Figure II-2.

In the limit of an infinitesimal timestep, the vector area  $\underline{A}_i$  is composed of a portion of the two trapezoidal surfaces whose intersection contains the point  $i$ . For example,  $\underline{A}_3$  corresponds to the shaded area in Figure II-1 when  $i = 3$  and thus

$$\underline{A}_3 = \underline{A}_{23} + \underline{A}_{33} \quad (\text{II-6})$$

$\underline{A}_{23}$  and  $\underline{A}_{33}$  are calculated as described below for the general vector area,  $\underline{A}_{ij}$ .

The vector area  $\underline{A}_{ij}$  is the trapezoidal surface of the quadrilateral wedge between the vertices  $i, j$  of Figure II-1. The sense of the vector area  $\underline{A}_{ij}$  is that of the outer normal to the surface. Thus, for example, if one encounters point  $i = 3$ , and then the point  $j = 4$ , as the perimeter of the quadrilateral wedge is traversed clockwise, then

$$\underline{A}_{ij} = \underline{A}_{34} = \frac{1}{2} [(\underline{r}_\beta - \underline{r}_\gamma) \times (\underline{r}_\alpha - \underline{r}_\gamma)] \quad (\text{II-7})$$

which per angle  $\phi$  can be shown to reduce to

$$\underline{A}_{34} = \frac{1}{2} (x_3 + x_4) \begin{bmatrix} y_3 - y_4 \\ x_4 - x_3 \\ 0 \end{bmatrix} \quad (\text{II-8})$$

However, the vector areas  $\underline{A}_i$  can be expressed directly in terms of the vertices of quadrilateral "a" as shown below for  $\underline{A}_3$ .

$$\underline{A}_3 = \begin{bmatrix} A_{3x} \\ A_{3y} \\ 0 \end{bmatrix} = \frac{1}{6} \begin{bmatrix} y_2(x_2 + x_3) - y_4(x_3 + x_4) + A_{23} + A_{34} \\ -x_2(x_2 + x_3) + x_4(x_3 + x_4) \\ 0 \end{bmatrix} \quad (\text{II-9})$$

where

$$A_{23}^n = x_2^n y_3^n - x_3^n y_2^n \quad (\text{II-10})$$

Equation (II-5) has the geometric interpretation that the change in the volume of a quadrilateral wedge in a time interval  $\Delta t$  is equal to the algebraic sum of the volumes swept out by the four trapezoidal faces of the wedge normal to the x-y plane, if appropriate portions of each face move with a uniform velocity equal to the velocity of the vertex. The volume change so calculated is exact, regardless of the time interval  $\Delta t$  or of the positions of the vertices of the quadrilateral zone at the beginning and end of the interval.

According to assumption (b), thermodynamic variables such as stresses and internal energies are considered to be properties of quadrilateral wedges as a whole. These variables are updated for general stresses and strains by an extension of a standard

numerical hydrodynamic procedure in which a finite difference analog of the First Law is satisfied simultaneously with the constitutive equation for a given medium. In the hydrodynamic case, the change in the internal energy of a quadrilateral wedge is just its volume change given by Eq. (II-5), multiplied by the negative of the arithmetic mean of the pressures in the wedge at the times  $t^{n-1}$  and  $t^n$ .

$$E^n - E^{n-1} = -PQ (V^n - V^{n-1}) \quad (\text{II-11})$$

where  $PQ$  denotes  $(P + Q)^{n-\frac{1}{2}}$ . If an equation of state is used to eliminate the new pressure (i.e., the pressure at time  $t^n$ ) from the finite difference analog of the First Law, then the fact that equations of state generally involve the internal energy renders the First Law analog an implicit equation for the new internal energy.

$$P^n = g(\rho^n, E^n) \quad (\text{II-12})$$

Here  $g$ , the equation of state, is some (known) function of two variables, and  $P$ ,  $E$ ,  $\rho$  denote the pressure, internal energy and density of the quadrilateral wedge, respectively, the mass being constant in the Lagrangian case under discussion. Also,  $Q$  is a generalization of the artificial viscosity of von Neumann and Richtmyer (1950).  $Q$  is computed explicitly knowing  $V$ , while  $P^n$  and  $E^n$  should be obtained by solving Eqs. (II-11) and (II-12) simultaneously. In this calculation, it is worth noting that if

the pressure in the quadrilateral wedge were indeed uniform and equal to its mean value on the time interval  $\Delta t$ , then the calculation of the change in the internal energy of the wedge, as well as its volume change, would be exact.

For general axisymmetric two-dimensional motion, the procedure for writing an exact finite difference analog of the First Law is not so obvious as for hydrodynamic motion. In fact, an exact analog of the First Law can be written only for triangular zones and not for more general polygons such as quadrilaterals.

In obtaining a finite difference analog of the First Law for general stress and strain, the change in the volume of the zone, as given in Eq. (II-5), is of prime importance. Introducing this expression for the volume change into Eq. (II-11) leads directly to a finite difference analog of the First Law which can be used for any stress, hydrodynamic or otherwise, and which is exact in the hydrodynamic case under assumptions (a) and (b). This combination of Eqs. (II-5) and (II-11) for the zone "a" is

$$E^n - E^{n-1} = \Delta t \sum_{i=1}^4 \underline{U}_i \cdot \underline{F}_i \quad (\text{II-13})$$

where for hydrodynamic motion, the forces  $\underline{F}_1, \dots, \underline{F}_4$  in Eq. (II-13) are given by the equations of the form

$$\underline{F}_i = (PQ) (\underline{A}_{\underline{e}_i} + \underline{A}_{\underline{d}_i}) \quad (\text{II-14})$$

To compute the change in internal energy for general stresses the scalar hydrodynamic stress (PQ) of Eq. (II-14) is replaced by the stress tensor  $\sigma_{ij}$ . Again, in accord with assumption (b),  $\sigma_{ij}$  is assumed to be constant during a timestep throughout any particular quadrilateral wedge. The definitions of the forces  $\underline{F}_1, \dots, \underline{F}_4$  then become

$$\underline{F}_i = \sigma_{ij} \cdot ( \underline{A}_{a1} + \underline{A}_{1d} ) \quad (\text{II-15})$$

etc., where the multiplication called for in Eq. (II-15) is that of a matrix with a vector.

As an expression for the change of internal energy, the right-hand member of Eq. (II-13) presents one obvious problem: its terms are all defined only on the surface of a material element, whereas "internal" energy is in fact a quantity associated in an essential way with the interior of a material region. To transform Eq. (II-13) so that it involves only interior areas of a quadrilateral wedge, an elementary geometric theorem is used. This theorem, which is a cornerstone of the finite difference method embodied in the AFTON codes, simply states that the sum of the vector areas of any polyhedral surface is zero, where the sense of the vector area associated with each face of the polyhedron is understood to be that of the outer normal to the enclosed volume. The meaning of the theorem can be exhibited in the following geometric way. Viewed from any aspect at a sufficiently great distance, a polyhedron presents a cross-section which is at one and the same time the

projection of the front side of the polyhedron on a plane normal to the viewer's line of sight, and also of its back side. The area of the cross-section is equal in magnitude to the component of the resultant vector area of the plane surfaces making up the front side of the polyhedron, and is also the negative of the corresponding component of the resultant area of the faces of the back side (see Figure II-3). Since the faces of the front and back side make up the entire (closed) polyhedral surface, the sum of all the vector areas is plainly zero.

With respect to the calculation of internal energy changes, Eq. (II-13) can be transformed so that its forces refer only to trapezoidal surfaces in the interior of the quadrilateral wedge plus the wedge faces. The theorem just discussed implies, for example, that the sum of the trapezoidal area  $\underline{A}_{ld}$ ,  $\underline{A}_{da}$ ,  $\underline{A}_{aa}$  and  $\underline{A}_{al}$ , plus the sum of the areas of the two azimuthal surfaces of the wedge,  $\underline{A}_{w1}$ , is zero. Therefore

$$\underline{A}_{al} + \underline{A}_{ld} = -(\underline{A}_{da} + \underline{A}_{aa} + 2\underline{A}_{w1}) . \quad (\text{II-16})$$

The vector area,  $\underline{A}_{w1}$ , of the quadrilateral cross-section or wedge face is defined as follows

$$\underline{A}_{w1} = \frac{1}{2} [(\underline{r}_d - \underline{r}_a) \times (\underline{r}_l - \underline{r}_a)] . \quad (\text{II-17})$$

Thus, Eq. (II-13) can be written in the form

$$\begin{aligned} E^n - E^{n-1} = \Delta t [ & \underline{F}_{da}(\underline{U}_1 - \underline{U}_4) + \underline{F}_{da}(\underline{U}_2 - \underline{U}_1) + \underline{F}_{2a}(\underline{U}_3 - \underline{U}_2) + \underline{F}_{2a}(\underline{U}_4 - \underline{U}_3) \\ & + \underline{F}_{w1} \cdot \underline{U}_1 + \underline{F}_{w2} \cdot \underline{U}_2 + \underline{F}_{w3} \cdot \underline{U}_3 + \underline{F}_{w4} \cdot \underline{U}_4 ] . \end{aligned} \quad (\text{II-18})$$

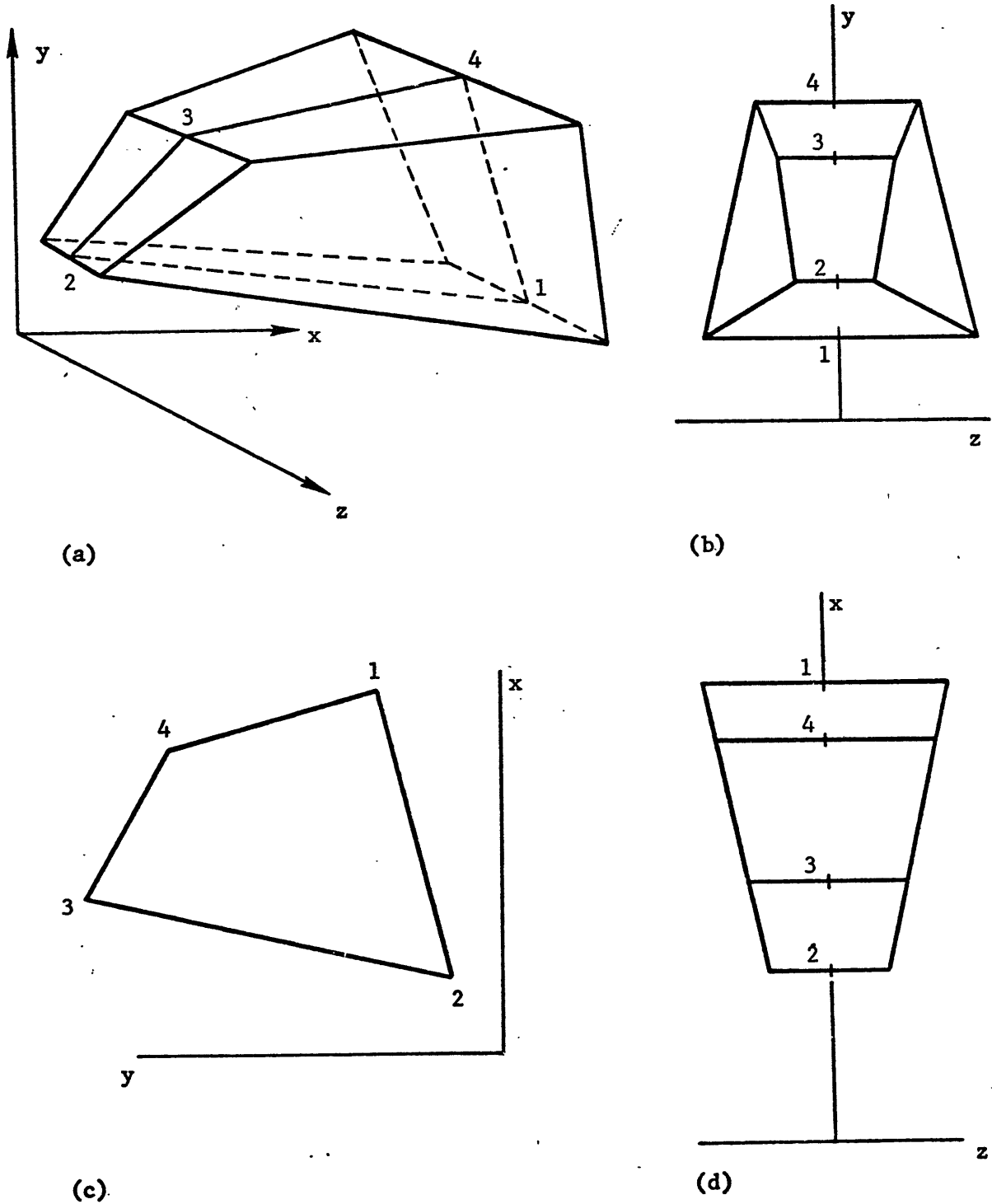


Figure II-3. Quadrilateral Wedge and Its Projections Into the x-y, y-z, and x-z Planes.

Equation (II-18) can be interpreted as a sum of internal energy changes produced by the extension of material in directions normal to the forces exerted on specific interior or wedge face surfaces of the quadrilateral wedge.

### Calculation of Momentum

In addition to updating the thermodynamic variables of a zone, new velocities and positions of the mesh points also need to be calculated. The procedure used to update velocities is based on the principle of momentum conservation, as applied to a spatial region known as a "momentum zone".

As in the case of velocities and positions, momentum zones are centered at mesh points. The momentum zone associated with a mesh point is comprised of a precisely defined portion of each of the four thermodynamic zones which share the mesh point as a common vertex. A thermodynamic zone is therefore divided into four pieces each of which is associated with one, and only one, vertex for the purpose of the momentum calculation. The division is made by joining an interior point of the zone, called its "mid-point", to certain points of its edges; for example, the point labeled *a* in Figure II-1 is connected to the points *a*, *d*, *2* and *3*. The trapezoidal surfaces bounded by pairs of points such as (*a*,*a*) or (*a*,*2*) (shaded in Figure II-4) represent a major portion of the interior areas upon which the stresses are imposed. The remaining portion of the area acted upon by stress is subtended by the wedge faces of the zone. The momentum zone contains a mass of material equal to the sum of a precise portion of each of the four thermodynamic zones which have as a

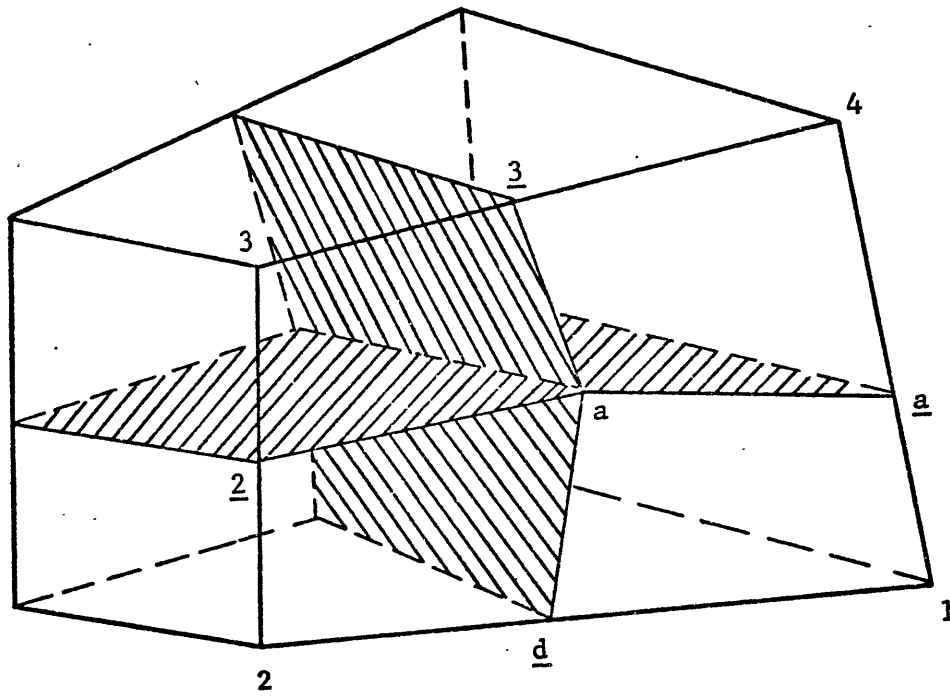


Figure II-4. Interior Areas of a Quadrilateral Wedge.

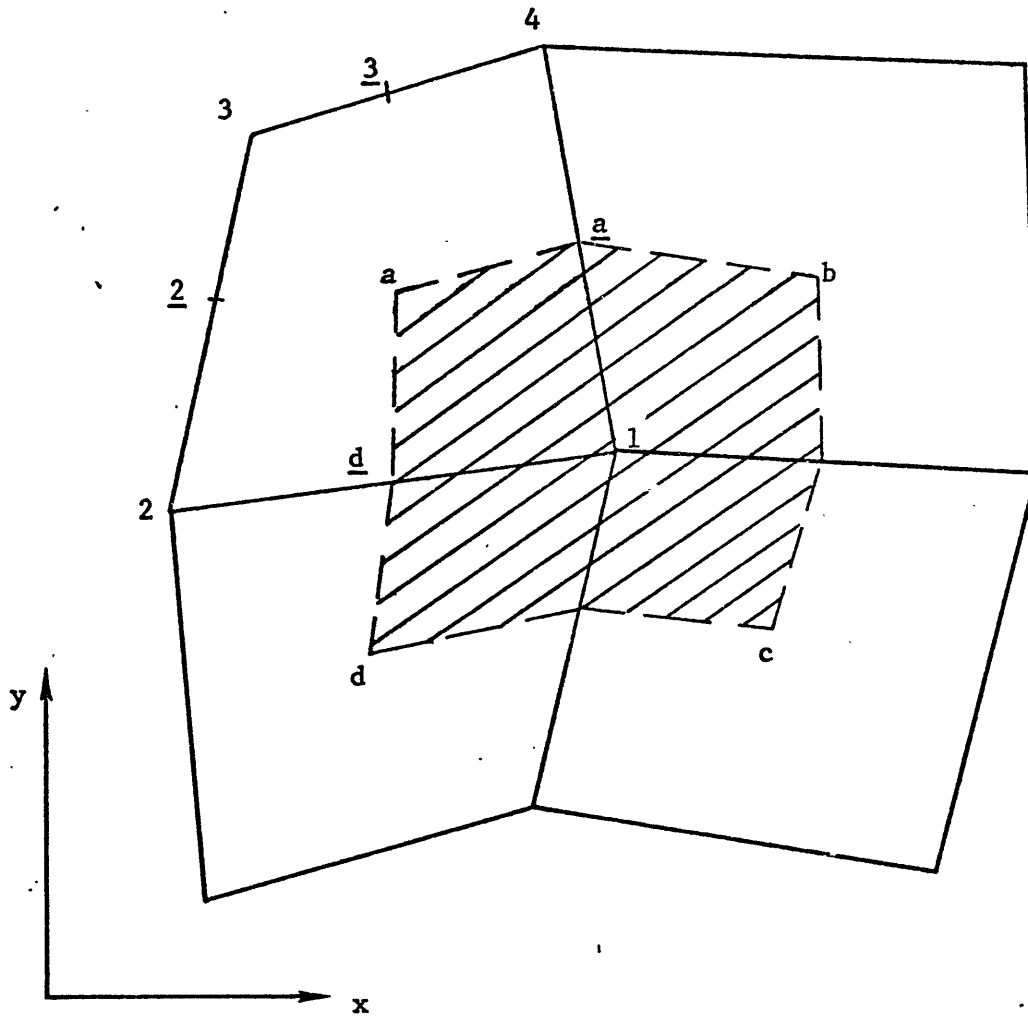


Figure II-5. Momentum Zone Centered at Point 1 Projected Into the x-y Plane; Point 1 is the Vertex Common to the Four Thermodynamic Zones Labeled a,b,c,d.

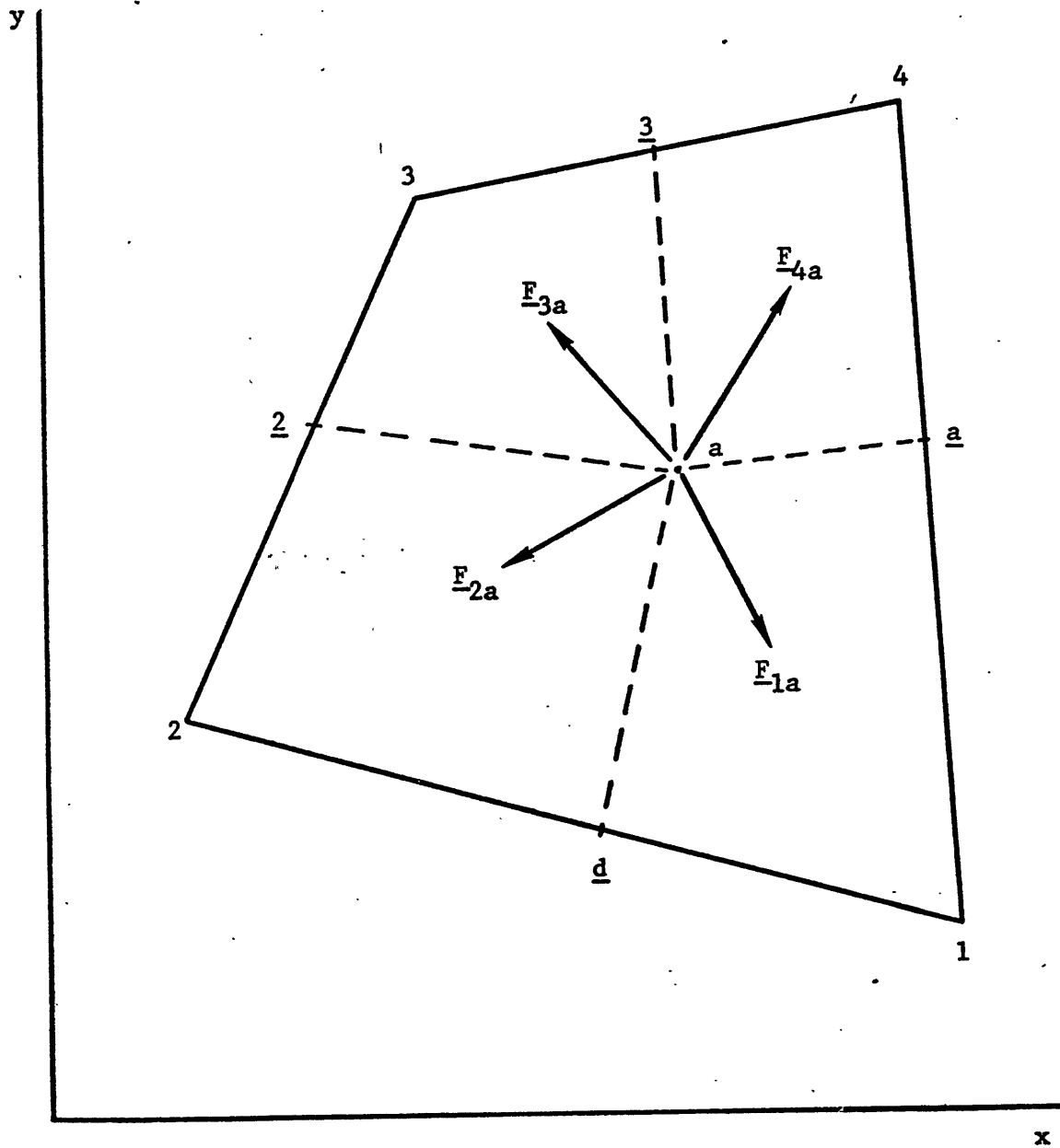


Figure II-6. Illustration of the Sense of the Forces  $\underline{F}_{1a}$ ,  $\underline{F}_{2a}$ ,  $\underline{F}_{3a}$ , and  $\underline{F}_{4a}$ .

common vertex the point about which the momentum zone is centered (i.e., the shaded area in Figure II-5). The momentum zone in AFTON-2A is then a polyhedron of ten faces. Forces exerted on the eight trapezoidal faces and two wedge faces of the momentum zone produce an acceleration of the momentum mass. If assumption (b) is true for both the forces acting on the momentum zone and the velocity of the zone during an entire timestep, then the change in momentum during a timestep may be calculated exactly. The momentum  $\underline{M}^n$ , at time,  $t^n$ , can now be updated from its value at time  $t^{n-1}$ . For the momentum zone, conservation of momentum is expressed by the equation

$$\underline{M}^n - \underline{M}^{n-1} = \Delta t \left[ \underline{F}_{1a} + \underline{F}_{2b} + \underline{F}_{3c} + \underline{F}_{4d} \right] \quad (\text{II-19})$$

In the above expression the force  $\underline{F}_{1a}$  is related to three of the forces which appear in Eq. (II-18), as follows

$$\underline{F}_{1a} = \underline{F}_{as} + \underline{F}_{da} + \underline{F}_{wa}$$

or

$$\underline{F}_{1a} = \begin{bmatrix} \sigma_{11} (A_{1x} - \underline{a}) + \sigma_{12} A_{1y} + \sigma_{33} \underline{a} \\ \sigma_{12} (A_{1x} - \underline{a}) + \sigma_{22} A_{1y} \\ 0 \end{bmatrix} \quad (\text{II-20})$$

and similarly for  $\underline{F}_{2b}$ ,  $\underline{F}_{3c}$  and  $\underline{F}_{4d}$ . The sense of the forces  $\underline{F}_{1a}$ , ...,  $\underline{F}_{4d}$  is illustrated in Figure II-6.  $\underline{a}$  is the scalar area of the wedge face whose vertices are  $l$ ,  $\underline{d}$ ,  $a$ ,  $\underline{a}$ . The velocity of the mesh point on which the momentum zone is centered is related to the momentum by the equation

$$\underline{U}^n = \frac{\underline{M}^n}{m} \quad (\text{II-21})$$

where  $m$  is the mass of the momentum zone. A forward extrapolation in time is used to advance the velocity from one timestep to the next.

$$\begin{aligned} \underline{U}^{n+1/2} &= 2 \underline{U}^n - \underline{U}^{n-1/2} \\ &= \frac{2 \underline{M}^n}{m} - \underline{U}^{n-1/2} \end{aligned} \quad (\text{II-22})$$

### Calculation Of Strain

The discussion of the calculation of strain will be initially restricted to considering an axially symmetric wedge (axis of symmetry is the  $y$ -axis) whose cross-section in the  $x$ - $y$  plane is a triangle. The calculation of strain for wedges with quadrilateral cross-sections will be treated later. Consider a triangular zone with vertices 1,2,3 in its unstrained configuration which, under the influence of external forces, is strained to a new configuration (Figure II-7). Then, in axial symmetry, the linear transformation which takes a point  $(x,y,z)$  in the unstrained state to the strained state  $(x',y',z')$  is given by

$$\begin{aligned} x' &= a_{11}x + a_{12}y \\ y' &= a_{21}x + a_{22}y \\ z' &= a_{33}z \end{aligned} \quad (\text{II-23})$$

In general for any point  $(x,y,z)$  we can define

$$\begin{aligned} \alpha_i &= (x - x_i) \quad ; \quad \alpha'_i = (x' - x'_i) \\ \beta_i &= (y - y_i) \quad ; \quad \beta'_i = (y' - y'_i) \end{aligned} \quad i = 1, 2, 3$$

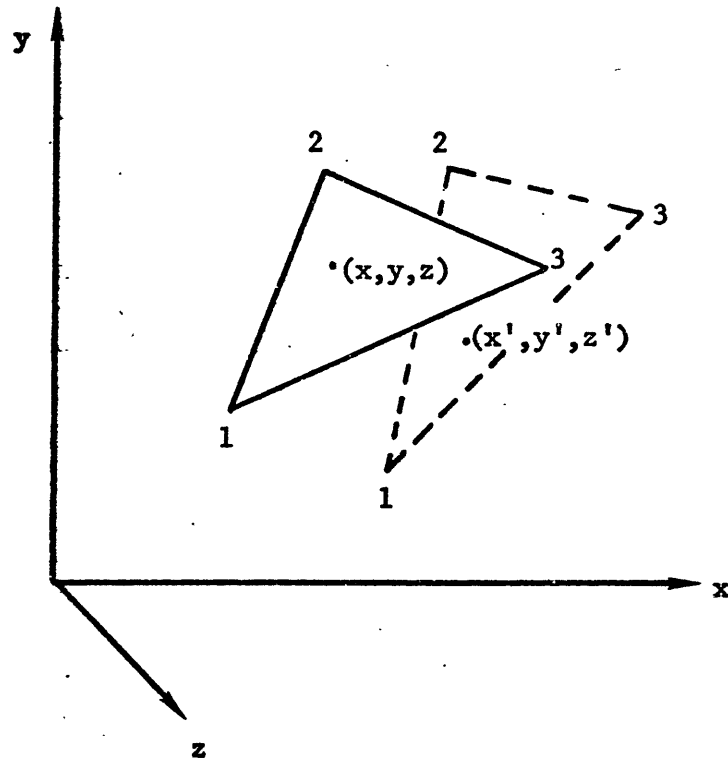


Figure II-7. Schematic of an Unstrained and Strained Triangular Zone.

Now form four equations in the four unknowns  $a_{11}$ ,  $a_{12}$ ,  $a_{21}$ ,  $a_{22}$ , which are elements of the point-transformation matrix A, namely

$$\begin{aligned} \alpha'_1 &= a_{11} \alpha_1 + a_{12} \beta_1 \\ \alpha'_2 &= a_{11} \alpha_2 + a_{12} \beta_2 \\ \beta'_1 &= a_{21} \alpha_1 + a_{22} \beta_1 \\ \beta'_2 &= a_{21} \alpha_2 + a_{22} \beta_2 \end{aligned} \quad (\text{II-24})$$

from which

$$\begin{aligned} a_{11} &= \frac{(\alpha'_1 \beta_2 - \alpha'_2 \beta_1)}{A_{\alpha\beta}} \quad ; \quad a_{12} = \frac{(\alpha'_1 \alpha_1 - \alpha'_2 \alpha_2)}{A_{\alpha\beta}} \\ a_{21} &= \frac{(\beta'_1 \beta_2 - \beta'_2 \beta_1)}{A_{\alpha\beta}} \quad ; \quad a_{22} = \frac{(\alpha_1 \beta'_2 - \alpha_2 \beta'_1)}{A_{\alpha\beta}} \end{aligned} \quad (\text{II-25})$$

where  $A_{\alpha\beta} = \alpha_1 \beta_2 - \alpha_2 \beta_1$ .

Using the elements of the transformation matrix A, a new matrix, T, can be formed

$$T = \begin{bmatrix} a_{11}^2 + a_{12}^2 & a_{11} a_{21} + a_{12} a_{22} \\ a_{11} a_{21} + a_{12} a_{22} & a_{21}^2 + a_{22}^2 \end{bmatrix} = \begin{bmatrix} t_{11} & t_{12} \\ t_{12} & t_{22} \end{bmatrix}. \quad (\text{II-26})$$

The eigenvalues  $\lambda_1$  and  $\lambda_2$  of T are now related to the principal extensions  $E_1$  and  $E_2$ , as follows:

$$E_1 = \lambda_1^{1/2} \quad ; \quad E_2 = \lambda_2^{1/2} \quad (\text{II-27})$$

where

$$\left. \begin{matrix} \lambda_1 \\ \lambda_2 \end{matrix} \right\} = \frac{1}{2} \left\{ (t_{11} + t_{22}) \pm \sqrt{(t_{11} - t_{22})^2 + 4t_{12}^2} \right\}. \quad (\text{II-28})$$

The third principal extension  $E_3$  is found from the ratio of the strained to unstrained volumes according to the equation

$$\frac{V}{V_0} = E_1 E_2 E_3 \quad . \quad (\text{II-29})$$

The three principal strains are related to the extensions by

$$\epsilon_x = E_1 - 1 \quad ; \quad \epsilon_y = E_2 - 1 \quad ; \quad \epsilon_z = E_3 - 1 \quad . \quad (\text{II-30})$$

The principal strain axes are found from the eigenvectors of  $T$ , namely,  $\underline{\Lambda}_1, \underline{\Lambda}_2$ , where

$$\underline{\Lambda}_1 = [(t_{11} - \lambda)^2 + t_{12}^2]^{-1/2} \begin{bmatrix} -t_{12} \\ t_{11} - \lambda \end{bmatrix}$$

$$\underline{\Lambda}_2 = [(t_{22} - \lambda)^2 + t_{12}^2]^{1/2} \begin{bmatrix} t_{22} - \lambda \\ -t_{12} \end{bmatrix} \quad . \quad (\text{II-31})$$

Of the four possible vectors which can be formed when  $\lambda_1$  and  $\lambda_2$  are substituted in the above equations, the two with the largest positive x- and y- components are chosen as the principal strain axes.

For a wedge whose cross-section is a quadrilateral, the strain cannot be defined uniquely. The convention used in AFTON to define the strain employs an averaging technique. Each diagonal of the quadrilateral divides it into two triangles. Elements of A-matrices are found for each of the four possible triangles formed by the two diagonals. Then the elements of  $T$

for the entire quadrilateral are formed by averaging the values of the elements of the A-matrix obtained for each of the four triangles.

### Calculation Of Stress

Knowing the principal strain axes, defined by the eigenvectors  $\underline{\Lambda}_x$  and  $\underline{\Lambda}_y$ , the principal strains can then be rotated into the laboratory coordinate system. The components of strain in the laboratory coordinate system are then given by the relations

$$\begin{aligned}\epsilon_{xx_L}^n &= (\Lambda_{x1}^n)^2 \epsilon_x^n + (\Lambda_{y1}^n)^2 \epsilon_y^n \\ \epsilon_{xy_L}^n &= \Lambda_{x1}^n \Lambda_{x2}^n \epsilon_x^n + \Lambda_{y1}^n \Lambda_{y2}^n \epsilon_y^n \\ \epsilon_{yy_L}^n &= (\Lambda_{x2}^n)^2 \epsilon_x^n + (\Lambda_{y2}^n)^2 \epsilon_y^n \\ \epsilon_{zz_L}^n &= \epsilon_z^n\end{aligned}\tag{II-32}$$

where the subscript L indicates that the strains are Lagrangian, i.e., they are computed at time n for the mass elements that occupied generalized coordinate cells at time n-1. Total strain increments are then formed as follows:

$$\Delta \epsilon_{ij} = \epsilon_{ij}^n - \epsilon_{ij}^{n-1} \tag{II-33}$$

The deviatoric strain increment is calculated from the equation

$$\Delta \epsilon'_{ij} = \Delta \epsilon_{ij} - \frac{1}{3} \delta_{ij} \Delta \epsilon_{ii} \tag{II-34}$$

Next, the Lagrangian compression  $\Lambda^n$  is calculated from the known mass and volume  $V_L^n$  of this material element, according to the

equation

$$\lambda_L^n = \frac{m^{n-1}}{\rho_0 v_L^n} \quad (II-35)$$

The compression increment  $\Delta\lambda_L = \lambda_L^n - \lambda_L^{n-1}$ , and the excess compression  $\mu_L^n = \lambda_L^n - 1$  are then formed. From the equation of state for the Lagrangian mass element the new mean stress,  $P^n$ , its derivative  $K = dP/d\mu$ , and the shear modulus,  $G$ , are computed. The deviatoric elastic stress tensor and its second invariant are then computed as follows:

$$(\sigma_{ij}^{e'})^n = (\sigma_{ij}^{e'})^{n-1} - 2G \Delta \epsilon_{ij}' \quad (II-36)$$

$$J_2^{e'} = \frac{1}{2} \sigma_{ij}^{e'} \sigma_{ij}^{e'} \quad (II-37)$$

and a function  $Y$  is evaluated according to the expression

$$Y = \min \left\{ \frac{\alpha_1 + \alpha_2 \bar{P} + \alpha_3 \bar{P}^2}{k} \right\} \quad (II-38)$$

where  $\alpha_i$  and  $k$  are constants and  $\bar{P}$  is the average mean stress  $(P^n + P^{n-1})/2$ ; the yield surface equation is  $J_2^{e'} = Y^2$ . If  $J_2^{e'} \leq Y^2$ , then

$$\sigma_{ij}^{\prime n} = \sigma_{ij}^{e'} \quad (II-39)$$

However, if  $J_2^{e'} > Y^2$ , then the incremental mean and deviatoric stresses are formed according to the incremental plastic stress-strain equations;

$$\Delta P = \frac{K \Delta \mu - K \left( \frac{dY}{dP} \right) \sigma'_{ij} - \frac{\Delta \epsilon_{ij}}{Y}}{1 + \left( \frac{dY}{dP} \right)^2 \frac{K}{G}} \quad (\text{II-40})$$

$$\Delta \sigma'_{ij} = G \left[ 2 \Delta \epsilon'_{ij} - \frac{\sigma'_{ij} (\sigma'_{ij} \Delta \epsilon'_{ij})}{2 J_2'} \right] - \sigma'_{ij} \frac{\left( \frac{dY}{dP} \right) \Delta P}{Y} \quad (\text{II-41})$$

The deviatoric stress is then computed as follows:

$$\sigma'_{ij}{}^n = \sigma'_{ij}{}^{n-1} + \Delta \sigma'_{ij} \quad (\text{II-42})$$

The calculation of the updated components of Lagrangian stress is completed using the equation

$$\sigma_{ijL}{}^n = s_{ij} P^n + \sigma'_{ij}{}^n \quad (\text{II-43})$$

## Appendix III.

Auxiliary Computation Routines

Three computer programs, in addition to the AFTON-2A code, were important to the results and displays contained in this document. The first was the ballistic extension model used to extend the calculated velocity conditions at 16.4 msec in the Mixed Company II simulation to the final grid position at 616.4 msec. The second was a flow-field parameter-display program that used the restart dump tapes to construct spatial displays at a particular simulated-time. The final program was the time-history display program which used the target-point data tapes to construct the time histories. This third program involved only data handling and simple manipulations and will not be described. However, the first two programs included calculational procedures that are important to their use.

Ballistic Extension Routine. The ballistic extension model had to describe what grid points were moving, how that motion changed position and velocity values during one time increment, and what grid points stopped moving during the time increment. The major assumptions of the routine were 1) that all motion occurred under the influence of gravity only, and 2) that only large displacements were of interest.

A parameter,  $S_t$ , was used at each grid point to differentiate between moving and stopped grid points. For moving grid points the value of this parameter was zero, and for stationary grid points  $S_t$  was set to one. At the beginning of the ballistic

extension to MC 2.12 the grid points above 20 ft depth and within a 35 ft range from the vertical axis were considered moving, while all other grid points were considered stopped. This region was defined because of the primary interest in the crater region and because the velocity conditions outside that region, except in the soil layer, would result in calculated displacements of less than one inch under ballistic conditions.

The motion of each grid point inside that region was calculated at time increments,  $\Delta t$ , of two milliseconds until three conditions were simultaneously satisfied. The first condition was that at least one of the grid points which were originally either immediately below or radially away from the grid point being considered had stopped. This condition was met if the value of  $S_t$  at either of those neighboring grid points was one. The second condition was that the vertical velocity component, calculated during the previous time increment, was not positive. The third condition was that the material density in the lower, outward quarter volume associated with the grid point was at least 1.5 gm/cc. This density was determined by dividing the mass in that quarter zone, which was constant because of Lagrangian motion, by the volume of the quarter zone calculated, using the volumetric subroutine of AFTON-2A, at the beginning of the time increment. If all three of these conditions were met, the value of  $S_t$  at the zone being considered was set to one.

The motion of each grid point was then calculated based on the value of  $S_t$ . If the value of  $S_t$  at the grid point was

one, both the horizontal and vertical velocity components were set to zero and the position coordinates of the grid point remained constant. If the value of  $S_t$  at the grid point was zero, then the horizontal velocity component,  $U_x$ , remained constant and the vertical velocity component,  $U_y^1$ , at the end of the time increment was determined by

$$U_y^1 = U_y^0 - g \Delta t \quad (\text{III-1})$$

where  $U_y^0$  is the vertical velocity component at the beginning of the time increment and  $g$  is the gravitational acceleration. The position coordinates of the grid point  $(X^1, Y^1)$  at the end of the time increment were then

$$\begin{aligned} X^1 &= X^0 + U_x \Delta t \\ Y^1 &= Y^0 + \Delta t \left[ U_y^0 - \frac{g}{2} \Delta t \right] \end{aligned} \quad (\text{III-2})$$

where  $(X^0, Y^0)$  are the position coordinates at the beginning of the time increment.

Flow Field Display Routines. The calculation space displays were used to display calculated motion and thermodynamic parameters at appropriate positions. These values, except for the maximum pressure contour plot, were for a particular moment of simulated time and were represented by vector arrows that began at the calculational position, indicated the vector direction, and had lengths scaled to the magnitude of the value. A vector would not be drawn, however, if 1) the calculational position was outside the display field, 2) the display length of the vector was less than a minimum value, or 3) the length of the vector would

cause it to extend beyond the display borders. Minimum length vectors were 0.01 inch on the velocity vector plots and 0.03 inch on the acceleration, principal stress, and calculation grid plots. The displays that required significant data manipulation were the plots of acceleration vectors, principal stress axes, and maximum pressure contours.

The acceleration vectors and principal stress vectors were represented by arrows with lengths proportional to the square root of magnitude but were constructed to maintain the exact vector direction. The second condition required that

$$\frac{l_x}{l_y} = \frac{A_x}{A_y} \quad (\text{III-3})$$

where  $l_x$  and  $l_y$  are the x and y components of the display vector and  $A_x$  and  $A_y$  are the linearly scaled components of the quantity to be represented. The first condition is satisfied if

$$l_x^2 + l_y^2 = (A_x^2 + A_y^2)^{1/2}. \quad (\text{III-4})$$

Solving these two relations for  $l_y$  implied

$$l_y = \pm \left[ (A_x^2 + A_y^2)^{1/2} / \left(1 + \frac{A_x^2}{A_y^2}\right) \right]^{1/2} \quad (\text{III-5})$$

where the sign for  $l_y$  was chosen to be the same as  $A_y$ . The value of  $l_x$  was then determined from relation (III-3). However, this scheme would not work on a computer if  $A_y$  was near zero. Since the Calcomp hardware will not plot distances less than 0.01 inches, an alternate scheme was used when  $A_y$  was less than 0.0001. The alternate scheme set  $l_y$  equal zero and set

$$l_x = \pm (|A_x|)^{1/2} \quad (\text{III-6})$$

where the sign of  $l_x$  was chosen to be the same as  $A_x$ .

The acceleration vector was determined from the velocity and timestep information in the restart dumps. The AFTON-2A code retains velocity components ( $U_x^n, U_y^n$ ) at a simulated time and velocity components ( $U_x^{n+\frac{1}{2}}, U_y^{n+\frac{1}{2}}$ ) extrapolated one-half timestep ahead. The acceleration components ( $a_x, a_y$ ) were determined by

$$\begin{aligned} a_x &= 2 ( U_x^{n+\frac{1}{2}} - U_x^n ) / \Delta t^n \\ a_y &= 2 ( U_y^{n+\frac{1}{2}} - U_y^n ) / \Delta t^n \end{aligned} \quad \text{(III-7)}$$

where  $\Delta t^n$  is the timestep.

The calculation of principal stresses and principal stress direction was based on the Mohr circle construction. The maximum and minimum principal stresses were found by

$$\begin{aligned} \sigma_1 &= 0.5 ( \sigma_{xx} + \sigma_{yy} ) + R \\ \sigma_2 &= 0.5 ( \sigma_{xx} + \sigma_{yy} ) - R \end{aligned} \quad \text{(III-8)}$$

$$\text{where } R = [ 0.25 ( \sigma_{xx} - \sigma_{yy} )^2 + \sigma_{xy}^2 ]^{1/2}$$

and  $\sigma_{xx}$ ,  $\sigma_{yy}$ , and  $\sigma_{xy}$  represent the radial, vertical, and shear stresses from the restart dump. The maximum principal stress was considered to be in the x principal axis direction unless  $\sigma_{yy}$  was greater than  $\sigma_{xx}$ . The angle of rotation,  $\theta$ , of the principal axes from the page coordinates was

$$\theta = 0.5 \tan^{-1} \left( \frac{2 \sigma_{xy}}{|\sigma_{xx} - \sigma_{yy}|} \right) \quad \text{(III-9)}$$

unless  $|\sigma_{xy}| > 100 \cdot |\sigma_{xx} - \sigma_{yy}|$

in which case  $\theta = \pm 45^\circ$  with the sign chosen the same as  $\sigma_{xy}$ .

A positive  $\theta$  would rotate the principal stress axes from the

page axes in a clockwise manner. This scheme was used unless the stress values indicated the material had separated at the thermodynamic point being considered, in which case an X was centered at the point.

A maximum pressure contour plot involved first locating the original position of the thermodynamic grid point and then determining the maximum pressure experienced by that point. The original position of the grid point was determined by first subtracting the displacements of the four surrounding mesh points from their positions at the time of the restart dump to determine the original grid positions. Then the excess compression value was equated to the maximum excess compression value of the thermodynamic point being considered and the AFTON-2A equation-of-state routine was used to determine the maximum pressure value. These values were then contoured with the use of a contour mapping subroutine which was provided by the computer support division of the Air Force Cambridge Research Laboratories.

Bibliography

1. Ahrens T. J. and J..T. Rosenberg, 1968, "Shock Metamorphism: Experiments on Quartz and Plagioclase," Shock Metamorphism of Natural Materials, ed French and Short, Mono Book Corporation, Baltimore, MD, pg 59 - 82.
2. Air Force Weapons Laboratory, 1973, REVROC Calculations, unpublished report, AFWL/DEV, Kirtland AFB, NM.
3. Amsden A. A., 1966, Particle-in-Cell Method for the Calculation of the Dynamics of Compressible Fluids, Los Alamos Scientific Laboratory, U. of California, New Mexico, LA-3466.
4. Baldwin R. B., 1963, The Measure of the Moon, The University of Chicago Press.
5. Beals C. S., 1965, "The Identification of Ancient Craters," Annals of the New York Academy of Sciences, Vol 123, Article 2, pg 904 - 914.
6. Boon J. D. and C. C. Albritton Jr., 1937, "Meteorite Scars in Ancient Rocks," Field and Lab., 5, No. 2, pg 53 - 64.
7. Bratton J. L., 1973, "Middle Gust - Mixed Company Comparisons," Proceedings of the Mixed Company/Middle Gust Results Meeting, Vol II, General Electric Company TEMPO (DASIAC), pg 268 - 295.
8. Carnes B. L., 1973a, "Mixed Company Event, LN301, Crater and Ejecta Studies - Preliminary Report," Proceedings of the Mixed Company/Middle Gust Results Meeting, Vol II, General Electric Company TEMPO (DASIAC), pg 63 - 78.
9. Carnes B. L., 1973b, Personal letter and data, Waterways Experiment Station, U. S. Army Corps of Engineers, Vicksburg, MISS, 18 October.
10. Choromokos J. and J. R. Kelso, 1973, "Operation Mixed Company," Proceedings of the Mixed Company/Middle Gust Results Meeting, Vol I, General Electric Company TEMPO (DASIAC), pg 74 - 96.
11. Christensen D. M., C. S. Godfrey, and D. E. Maxwell, 1968, Calculations and Model Experiments to Predict Crater Dimensions and Free Field Motion, PIFR-072, DASA-2360, Physics International Company, San Leandro, CA 94577.
12. Christensen D. M., 1970, ELK-40: Prediction Calculation of Ground Motion for Distant Plain, Event 6, DASA-2471, Physics International Company, San Leandro, CA.

13. Circeo L. J. and N. D. Nordyke, 1964, Nuclear Cratering Experience at the Pacific Proving Grounds, University of California, Lawrence Radiation Laboratory, Livermore, CA, UCRL-12172.
14. Cooper H. F., 1971, On the Application of Finite Difference Methods to Study Wave Propagation In Geologic Materials, AFWL-TR-70-171, Air Force Weapons Laboratory, Kirtland AFB, NM.
15. Davis S. E., 1973, "Experimental Data from Middle Gust and Mixed Company Company CIST Events," Proceedings of the Mixed Company/Middle Gust Results Meeting, Vol II, General Electric Company TEMPO (DASIAC), pg 439 -457.
16. Day J. D., 1973, "Ground Motion Measurements - Mixed Company Calibration Events," Proceedings of the Mixed Company/Middle Gust Results Meeting, Vol II, General Electric Company TEMPO (DASIAC), pg 148 - 165.
17. Dence M. R., 1968, "Shock Zoning at Canadian Craters: Petrography and Structural Implications," Shock Metamorphism of Natural Materials, ed French and Short, Mono Book Corporation, Baltimore, MD, pg 169 - 184.
18. Dence M. R., M. J. S. Innes, and P. B. Robertson, 1968, "Recent Geological and Geophysical Studies of Canadian Craters," Shock Metamorphism of Natural Materials, ed French and Short, Mono Book Corporation, Baltimore, MD, pg 339 - 362.
19. Dent B., 1974, "The Formation of Central Uplifts in Large Impact Craters," extract from Ph.D. dissertation, Dept. of Geophysics, Stanford University, Stanford, CA.
20. Dietz R. S., 1968, "Shatter Cones in Cryptoexplosion Structures," Shock Metamorphism of Natural Materials, ed French and Short, Mono Book Corporation, Baltimore, MD, pg 267 - 284.
21. Eggleton R. E., 1965, Geologic Map of the Rhipaeus Mountains Region of the Moon, USGS, Washington, D. C. I-458.
22. Ehr Gott J. Q., 1973, "Preshot Material Property Investigation for the Mixed Company Site: Summary of Subsurface Exploration and Laboratory Test Results," Proceedings of the Mixed Company/Middle Gust Results Meeting, Vol II, General Electric Company TEMPO (DASIAC), pg 491 - 539.
23. Gajewski R., 1973, Personal letter and data, Air Force Weapons Laboratory/DEV, Kirtland AFB, NM.

24. Gault D. E., W. L. Quaide, and V. R. Oberbeck, 1968, "Impact Cratering Mechanics and Structures," Shock Metamorphism of Natural Materials, ed French and Short, Mono Book Corporation, Baltimore, MD, pg 87 - 100.
25. Harlow F. H. and J. P. Shannon, 1967, "The Splash of a Liquid Drop," Journal of Applied Physics, 38, pg 3855 - 3866.
26. Hartmann W. K., 1972, "Interplanet Variations in Scale of Crater Morphology - Earth, Mars, Moon," Icarus, 17, pg 707 - 713.
27. Hartmann W. K., 1973, "Martian Cratering, 4, Mariner 9 Initial Analysis of Cratering Chronology," Journal of Geophysical Research, 78, pg 4096 - 4116.
28. Howard K. A., T. W. Offield, and H. G. Wilshire, 1972, "Structure of Sierra Madera Texas as a Guide to Central Peaks of Lunar Craters," Geological Society of America Bulletin, 83, pg 2795 - 2808.
29. Ialongo G., 1973, "Mixed Company III Prediction Calculation," Proceedings of the Mixed Company/Middle Gust Results Meeting, Vol II, General Electric Company TEMPO (DASIAC), pg 669 - 694.
30. Jones A. H., W. M. Isbell, F. H. Shipman, R. D. Perkins, S. J. Green, and C. J. Maiden, 1968, Material Properties Measurements for Selected Materials, NAS 2-3427 Interim Report, General Motors Materials and Structures Laboratory, Warren, MICH 48090.
31. McConnell R. K., Jr., and P. W. Gast, 1972, "Lunar Thermal History Revisited," Moon, 5, pg 41 - 51.
32. Manley W. D., P. H. Schultz, and E. Ingerson, 1973, "Central Peaks of Martian and Lunar Craters: A Comparison," Abstract-P 15, EOS, 54, No 11, pg 1127.
33. Maxwell D. and H. Moises, 1971a, Prediction Calculations of Mine Under and Mine Ore, DASA-2526, Physics International Company, San Leandro, CA, 94577.
34. Maxwell D. and H. Moises, 1971b, Hypervelocity Impact Cratering Calculations, PIFR-190, Physics International Company, San Leandro, CA, 94577.
35. Meyers J., 1973, "Middle Gust Crater and Ejecta Studies," Proceedings of the Mixed Company/Middle Gust Results Meeting, Vol II, General Electric Company TEMPO (DASIAC), pg 29 - 49.
36. Milton D. J. and D. J. Roddy, 1972, "Displacements within Impact Craters," Proceedings, International Geological Congress, Twenty - Fourth Session, Section 15, pg 119 - 124.

37. Milton D. J., B. C. Barlow, R. Brett, A. R. Brown, A. I. Glikson, E. A. Manwaring, F. J. Moss, E. C. E. Sedmik, J. Van Son, G. A. Young, 1972, "Gosses Bluff Impact Structure, Australia," Science, 175, No 4027, pg 1199 - 1207
38. Muskat M. and W. M. Meres, 1940, "Reflection and Transmission Coefficients for Plane Waves in Elastic Media," Geophysics, 5, pg 115 - 148.
39. Murray B. C., M. J. S. Belton, G. E. Danielson, M. E. Davies, D. Gault, B. Hapke, B. O'Leary, R. G. Strom, V. Suomi, and N. Trask, 1974, "Mariner 10 Pictures of Mercury: First Results," Science, 184, pg 459 - 461.
40. Niles W. J., J. J. Germroth, and S. H. Schuster, 1971, Numerical Studies of AFTON-2A Code Development and Applications, Vol II, AFWL-TR-70-22, Air Force Weapons Laboratory, Kirtland AFB, NM.
41. Pike R. J., 1971, "Genetic Implications of the Shapes of Martian and Lunar Craters," Icarus, 15, pg 384 - 395.
42. Port R. J. and R. Gajewski, 1973, "Sensitivity of Uniaxial Stress - Strain Relations on Calculations of Middle Gust Event III," Proceedings of the Mixed Company/Middle Gust Results Meeting, Vol II, General Electric Company TEMPO (DASIAC), pg 540 - 568.
43. Roddy D. J., 1968, "The Flynn Creek Crater, Tennessee," Shock Metamorphism of Natural Materials, ed French and Short, Mono Book Corporation, Baltimore, MD, pg 291 - 322.
44. Roddy D. J., 1968b, "Comet Impact and Formation of Flynn Creek and Other Craters With Central Peaks," American Geophysical Union Transactions, 49, No. 1, pg 272.
45. Roddy D. J., 1973, "Geologic Studies of the Middle Gust and Mixed Company Craters," Proceedings of the Mixed Company/Middle Gust Results Meeting, Vol II, General Electric Company TEMPO (DASIAC), pg 79 - 128.
46. Schmitt H. H., N. J. Trask, and E. M. Shoemaker, 1967, Geologic Map of the Copernicus Quadrangle of the Moon, USGS, Washington, D. C., I-515.
47. Shoemaker E. M., 1961, "Interpretation of Lunar Craters," Physics and Astronomy of the Moon, ed Kopal, Academic Press, pg 283 - 359.
48. Shoemaker E. M., 1963, "Impact Mechanics at Meteor Crater, Arizona," The Solar System, Vol 4, The Moon, Meteorites, and Comets, ed Middlehurst and Kuiper, University of Chicago Press, Chicago, ILL, pg 301 - 336.

49. Short N. M., 1965, "A Comparison of Features Characteristic of Nuclear Explosion Craters and Astroblemes," Annals of the New York Academy of Sciences, 123, pg 573 - 616.
50. Simmons G., T. Todd, and H. Wang, 1973, "The 25-km Discontinuity: Implications for Lunar History," Science, 182, pg 158 - 161.
51. Stearns R. G., C. W. Wilson Jr., H. A. Tiedemann, J. T. Wilcox, and P. S. Marsh, 1968, "The Wells Creek Structure, Tennessee," Shock Metamorphism of Natural Materials, ed French and Short, Mono Book Corporation, Baltimore, MD, pg 323 - 338.
52. Toksöz M. N., S. C. Solomon, J. W. Minear, and D. H. Johnston, 1972, "Thermal Evolution of the Moon," Moon, 4, pg 190 - 213.
53. Trulio J. G., 1964, Methods in Computational Physics, Vol III, Chapter 3, Academic Press, New York.
54. Trulio J. G., 1966, Theory and Structure of the AFTON Codes, AFWL-TR-66-19, Air Force Special Weapons Center, Kirtland AFB, NM.
55. Trulio J. G., J. J. Germroth, W. J. Niles, and W. E. Carr, 1967, Study of Numerical Solution Errors in One- and Two-Dimensional Finite Difference Calculations of Ground Motion, AFWL-TR-67-27, Vol I, Air Force Weapons Laboratory, Kirtland AFB, NM.
56. Trulio J. G., W. E. Carr, J. J. Germroth, and M. W. McKay, 1969, "Ground Motion Studies and AFTON Code Development," Numerical Ground Motion Studies, Vol III, AFWL-TR-67-27, Air Force Weapons Laboratory, Kirtland AFB, NM.
57. Trulio J. G. and N. K. Perl, 1973, "Limitations of Present Computational Models of Explosive Induced Ground Motion: Middle Gust Event 3," Proceedings of the Mixed Company/Middle Gust Results Meeting, Vol II, General Electric Company TEMPO (DASIAC), pg 568 - 619.
58. Von Neumann J. and R. D. Richtmeyer, 1950, "A Method for the Numerical Calculation of Hydrodynamic Shocks," Journal of Applied Physics, 21, pg 232 - 237.
59. White J. W., 1973, "An Invariant Description of Failure for an Isotropic Medium," Journal of Geophysical Research, 78, pg 2438 - 2441.

60. Windham J. E., R. A. Knott, and J. S. Zelasko, 1973, "Geologic and Material Comparisons for the Middle Gust Test Sites," Proceedings of the Mixed Company/Middle Gust Results Meeting, Vol II, General Electric Company TEMPO (DASIAC), pg 458 - 491.
61. Wright J. P., I. S. Sandler, and M. L. Baron, 1973, "Ground Motion Calculations for Events II and III of the Middle Gust Series," Proceedings of the Mixed Company/Middle Gust Results Meeting, Vol II, General Electric Company TEMPO (DASIAC), pg 620 - 645.
62. Zelasko J. S. and G. Y. Baladi, 1971, Free Field Code Predictions Versus Field Measurements: A Comparative Analysis for the Prairie Flat Event, Misc Paper S-71-6, U. S. Army Corps of Engineers Waterways Experiment Station, Vicksburg, MISS.

Biographical Note

Gilbert Wayne Ullrich was born in Vicksburg, Mississippi on October 17, 1946. He completed his high school education in 1963 at Savannah High School, Savannah, Georgia. He then entered The Citadel, in Charleston, South Carolina where, in 1967, he received his Bachelor of Science degree in Mathematics and a commission in the United States Air Force. His first active duty assignment was to the Air Force Institute of Technology at Wright-Patterson Air Force Base, Ohio where he obtained a Master of Science degree in Space Facilities Engineering in 1969. He was then assigned to the Minuteman Systems Program Office of the Space and Missiles Systems Organization where he was a project officer for programs concerning ground shock simulation including the Minuteman Free Field Ground Motion Program. In 1971 he was assigned to Kwangju AFB, South Korea where he was the Chief of Programs for the Base Civil Engineer. In 1972 he returned to the United States to begin work toward the Ph.D. degree in Geophysics at the Massachusetts Institute of Technology in the special assistantship program of the Air Force Institute of Technology.